

# INVESTIGATION OF DC MICROGRID STABILITY FOR SOURCE DISTURBANCES

Ph.D. THESIS

by

GINBAR ENSERMU



DEPARTMENT OF ELECTRICAL ENGINEERING  
INDIAN INSTITUTE OF TECHNOLOGY ROORKEE  
ROORKEE-247667 (INDIA)

June, 2020



# INVESTIGATION OF DC MICROGRID STABILITY FOR SOURCE DISTURBANCES

A Thesis

*Submitted in partial fulfillment of the  
requirements for the award of the degree  
of*

DOCTOR OF PHILOSOPHY

*in*

ELECTRICAL ENGINEERING

*by*

GINBAR ENSERMU



DEPARTMENT OF ELECTRICAL ENGINEERING  
INDIAN INSTITUTE OF TECHNOLOGY ROORKEE  
ROORKEE-247667 (INDIA)

June, 2020



**©INDIAN INSTITUTE OF TECHNOLOGY ROORKEE, ROORKEE-2020**  
**ALL RIGHTS RESERVED**



# INDIAN INSTITUTE OF TECHNOLOGY ROORKEE

## Student's DECLARATION

I hereby certify that the work which is being presented in thesis entitled “**Investigation of DC Microgrid Stability for Source Disturbances**” is my own work carried out during a period from July/2015 to June/2020 under the supervision of Dr. Avik Bhattacharya, Assistant Professor, Department of Electrical Engineering of Indian Institute of Technology Roorkee.

The matter presented in the thesis has not been submitted by me for the award of any other degree of this or any other Institute.

**GINBAR ENSERMU**

## Supervisor's DECLARATION

This is to certify that the above statement made by the candidate is correct to the best of my knowledge.

**Dated:** 12/06/2020

(Dr. Avik Bhattacharya)  
Supervisor



## ABSTRACT

The DC power distribution systems have been drawing significant attention and have shown the potential to compete with conventional AC systems. DC microgrids (DC $\mu$ Gs) are based on direct current technologies and consist of distributed energy resources (DER) and loads operating in a controllable and synchronized way either in a grid-connected or islanded manner. Most energy sources such as solar photovoltaic (PV), fuel cell, and battery energy system are generating DC in nature. Nowadays, DC operated electronic loads are developing that eliminates further power conversion stages, reducing costs and losses.

Furthermore, DC $\mu$ G is more preferred than its AC counterpart because of its benefit, like; the direct connection of DC loads with renewables generating DC natively, more comfortable control system compared to AC counterparts, higher reliability, and efficiency. Power electronic converter plays a vital role in the efficient energy conversion system and integration of the DER units for excellent performance and efficiency of the power network. It can also be used to regulate the power flow between the source and the load subsystem.

However, the generation output disturbance of DGs, sudden load changes, and impedance mismatch among the source and load converters subsystem cause the stability problem of the DC microgrid. The hybrid DC $\mu$ G with multiple DG sources and ESSes have varying characteristics and fluctuating voltage levels due to the changing of the wind speed and solar irradiation. The micro sources are linked in parallel to the central DC grid system through power converters. The DC $\mu$ G has typical interconnected distributed power topologies in which the power converter interconnect between the portions of the policy with various voltages levels. In such structures, instability in the system occurs due to the tight control of load side converters that act as constant power loads (CPLs) in which its small-signal model contains negative input resistance. This negative incremental impedance causes the system poorly damped and can cause unstable poles in the frequency domain and worsen the system stability. The intermittent character of the input renewable energy sources and the continually changing power consumption are the variables that challenge the DC $\mu$ G power management and hence, DC bus stability.

The decentralized control scheme is proposed to manage the integrated system for proper and stable operation with the multiple sources interfaced in parallel to the primary DC grid using a single topology of the DC microgrid. Each source converters are controlled autonomously and

interconnected in a harmonized way to the point of a typical DC bus grid for reliable and flexible operations. The decentralized control method realizes the different operating modes using the DC bus voltage signal (DBS) control. This control method is a combination of voltage droop control and voltage level signaling. Voltage level signaling is a method that allows multiple source operations programmed in a prioritized manner. The dominant source is used to regulate the intermediate DC voltage. The control methodology offers an autonomously controlled service of each terminal without communication. MPPT and CVC (Constant Voltage Control) schemes are used in the DG's interface converter control to regulate power and voltage fluctuations due to changing input conditions.

Furthermore, the control strategy used the DC bus voltage as a control parameter. Each power source converters are prompted by monitoring the change of DC bus voltage to keep the DC $\mu$ G power balance. Accordingly, system reliability and flexibility operation is maintained. A DC $\mu$ G composed of wind, solar, BESS with and without grid-connection that enable flexible and reliable performance proposed in this thesis.

The control method uses the DC bus voltage level as a communication signal, and the self-controlled scheme implemented at each terminal without communication. The developed DC $\mu$ G decentralized control method is simulated in real-time simulations with software control-in-the-loop (CIL) to verify the controller accuracy and performance through OPAL-RT real-time simulator.

On the other hand, the input filter employed to mitigate disturbances due to switching devices and avoid electromagnetic interferences—the optimum damping resistance designed to eliminate instability problems in the feedback control loop of the POL converter. The stability problem is due to the dynamic filter interactions with sources. The stability condition verified using the Nyquist stability criterion.



## **ACKNOWLEDGMENT**

Firstly, I would like to praise the Almighty God, Lord Jesus Christ, who gave me peace, strength, and health in all my journey of accomplishment of this work.

I want to express my deepest gratitude to my respected supervisor Dr. Avik Bhattacharya for his support, encouragement, and guidance throughout my study at the Indian Institute of Technology Roorkee. His extensive knowledge, passionate research attitude and constructive suggestions have been a source of motivation for me throughout the study. I am also grateful to my research committee members: Dr. N.P.Padhy, Dr. M.K. Pathak, and Dr. Sudeb Dasgupta for their kind supports and suggestions for my research work.

I want to express my appreciation to my colleagues in project lab II, Mr. Haris Ahmed, Ms. Toshi Sharma, Mr. Muneer V., Mr. Rubell Sen Goopta, Ms. Priyanka Priyadarsini, and Mr. Diress Tilahun for their great supports, precious friendship, and valuable discussions.

I would also like to express my deepest gratitude to the Head of the Department of Electrical Engineering, and all faculty members of the department for their help, moral support, and providing the infrastructure, laboratory, and computing facility for the research work.

I acknowledge my sincere gratitude to the Ministry of Education of the Ethiopian Government and my institution (Wollega University) for providing me a chance to do my doctoral research work in India at the Indian Institute of Technology Roorkee with full financial support.

I am indebted to all the technical and administrative staff of the Electrical Engineering Department for their support and necessary facility provided to me to carry out this research work.

Most importantly, I would like to express the most profound appreciation to my wife Hawine Debela and my children (my son Kenna Ginbar and my daughter Fedi Ginbar) for their unconditional love, encouragement, support, care, trust, and patience. May all the praise be to the Almighty God, Lord Jesus Christ, for His grace and merciful.



# CONTENT

<b>ABSTRACT .....</b>	<b>i</b>
<b>ACKNOWLEDGMENT .....</b>	<b>iii</b>
<b>CONTENT .....</b>	<b>v</b>
<b>LIST OF FIGURES .....</b>	<b>ix</b>
<b>LIST OF TABLES .....</b>	<b>xiii</b>
<b>LIST OF ACRONYMS .....</b>	<b>xv</b>
<b>LIST OF SYMBOLS .....</b>	<b>xvii</b>
<b>CHAPTER 1: INTRODUCTION .....</b>	<b>1</b>
1.1.DC Microgrid Background and Motivation of the Research .....	1
1.2.Literature Review .....	4
1.2.1. Historical Development of DC Microgrids .....	4
1.2.2. Control Strategies in DC Microgrids .....	5
1.2.3. Stability Issues in DC Microgrid .....	10
1.2.4. Application of DC Microgrid .....	11
1.3.Challenges of the Research and Proposed Solution .....	12
1.3.1. Research Challenges .....	12
1.3.2. Proposed Solutions .....	13
1.4.The Research Objectives .....	13
1.5.Thesis Organization .....	14
<b>CHAPTER 2: DC DISTRIBUTED ENERGY RESOURCE MODELLING AND CONTROL .....</b>	<b>17</b>
2.1.Grid-Connected Voltage Source Converter System (VSC) .....	18
2.1.1. Voltage Source Converter (VSC) Modeling .....	18
2.1.2. Active and Reactive Power Control .....	23
2.2.The Distribution Generation (DG) System .....	35
2.2.2. The PV Power Generation System .....	44
2.3.Battery Energy Storage Modelling .....	49
2.3.1. The BESS Converter Modeling and Control .....	50

2.4.Summary .....	54
<b>CHAPTER 3: DECENTRALIZED CONTROL SCHEME OF DC MICROGRID UNDER SOURCE DISTURBANCES .....</b>	<b>57</b>
3.1.Development of DC Microgrid Architectures .....	57
3.2.The DC Microgrid Power Management and Operation Strategy .....	60
3.2.1. DC Microgrid Power Management Techniques .....	60
3.2.2. DC Microgrid Operation .....	63
3.3.DC Microgrid Power Flow Analysis.....	65
3.4.DC Microgrid Control Strategies .....	66
3.5.Basic Concept and Analysis of Droop Control .....	68
3.5.1. Droop Control in AC Microgrid.....	68
3.5.2. Droop Control in DC Microgrid.....	70
3.5.3. Analysis of Droop Control in DC Power System.....	71
3.6.Constant Power Load Modelling.....	73
3.7.Concept of the Real-Time Simulator .....	76
3.8.Simulation Result Discussion .....	77
3.9.Summary .....	84
<b>CHAPTER 4: STABILITY ANALYSIS OF DC MICROGRIDS WITH CONSTANT POWER LOADS .....</b>	<b>85</b>
4.1.Characteristics of CPL Connected to DC Bus.....	86
4.2.Causes of DC Microgrid Instability .....	87
4.3.Dynamics of POL Converter .....	88
4.4.Input Filter for Stability Improvement.....	90
4.5.Damping of Input Filter .....	91
4.6.Stability Analysis Using Nyquist Stability Criteria .....	93
4.7.Result Discussion .....	94
4.8.Summary .....	97
<b>CHAPTER 5: CONCLUSION AND FUTURE RESEARCH WORK .....</b>	<b>99</b>
5.1.Conclusion .....	99
5.2.The Future Work .....	101
<b>BIBLIOGRAPHY .....</b>	<b>103</b>
<b>APPENDIX A.....</b>	<b>117</b>

A.1. Matlab/Simulink.....	117
A.2. Real-Time Simulation of DC Microgrid Matlab/Simulink Models Using OPAL-RT117	
<b>Appendix B .....</b>	<b>119</b>
B.1. List of Publication .....	119





## LIST OF FIGURES

Fig. 1. 1: The Development of Renewable Energy Installed Capacity in the World [11].....	2
Fig. 1. 2: Central Control System Structure .....	6
Fig. 1. 3: Decentralized Control System Structure .....	9
Fig. 2. 1: Grid-Connected Voltage Converter (G-VSC).....	18
Fig. 2. 2: Single-Phase LCL Equivalent Circuit.....	21
Fig. 2. 3: Frequency Bode Plot of LCL Filter .....	22
Fig. 2. 4: d-q axis Alignment Diagram .....	24
Fig. 2. 5: PLL Control Block.....	26
Fig. 2. 6: qd-axis voltage, (a) q-axis voltage, (b) d-axis voltage.....	26
Fig. 2. 7: PLL Compensator Result.....	28
Fig. 2. 8: VSC PQ Control System .....	29
Fig. 2. 9: Grid Input Parameters, (a) 3-phase grid-side voltage, (b) 3-phase AC line current, (c) phase to neutral voltage and line current (10 times increased) .....	31
Fig. 2. 10: Current THD (%) .....	31
Fig. 2. 11: Grid Rectified Output Parameters. (a) DC-link Voltage (V) (b) Power (watt).....	34
Fig. 2. 12: Turbine speed vs Wind Power System .....	37
Fig. 2. 13: Schematic Diagram of WECS Proposed in this Work .....	38
Fig. 2. 14: Boost Converter Operating Topologies .....	39
Fig. 2. 15: Wind Converter Control System.....	40
Fig. 2. 16: Input Voltage of Wind Boost DC/DC Converter, (a) Boost Converter Input Voltage (V <sub>w</sub> ) (b) MPPT Output Reference Voltage (V <sub>wref</sub> ).....	41
Fig. 2. 17: Wind and Solar Boost Converter Controller Block Diagram.....	42
Fig. 2. 18: Wind Converter Bode Plot of Current Control Loop .....	43
Fig. 2. 19: Wind Converter Bode Plot of Voltage Control Loop.....	44
Fig. 2. 20: PV Circuit Model and $I \times v$ Curve .....	45
Fig. 2. 21: Linearized PV Array Equivalent Circuit .....	46
Fig. 2. 22: Control Schematics for PV Boost DC/DC Converter.....	46
Fig. 2. 23: PV Boost Converter Input Voltage. (a) PV Array Voltage, (b) PV MPPT Output Voltage Reference .....	47
Fig. 2. 24: PV Interconnecting Converter in DC Microgrid.....	47
Fig. 2. 25: Solar Converter Bode Plot of Current Control Loop .....	49

Fig. 2. 26: Simplified Battery Nonlinear Circuit Model .....	49
Fig. 2. 27: Bidirectional DC/DC Converter Circuit Topology .....	50
Fig. 2. 28: Battery BDC Control Block.....	51
Fig. 2. 29: Battery Bidirectional Converter Inductor Current .....	52
Fig. 2. 30: Battery Current Control Loop Block Diagram .....	53
Fig. 2. 31: Battery Converter Current Control Loop Bode Plot .....	54
Fig. 2. 32: Battery Converter Boost Bode Plot for Voltage Control Loop .....	54
Fig. 3. 1: DC Microgrid Ring Bus Topology.....	58
Fig. 3. 2: DC Microgrid Single Bus Topology with ESS Directly Connected .....	58
Fig. 3. 3: DC Microgrid Topology with ESS Connected via Bidirectional DC/DC Converter .59	
Fig. 3. 4: DC Microgrid Bipolar Topology Type .....	60
Fig. 3. 5: The Proposed DC Microgrid Configuration .....	61
Fig. 3. 6: The System Switching Mode Logic Flow Chart .....	62
Fig. 3. 7: Operating Mode Definitions [18] .....	64
Fig. 3. 8: Power Management Schemes .....	64
Fig. 3. 9: DC Grid Simplified Power System .....	66
Fig. 3. 10: AC Microgrid Droop Control Scheme.....	68
Fig. 3. 11: Simplified AC Equivalent Circuit .....	69
Fig. 3. 12: Droop Control Characteristic.....	70
Fig. 3. 13: DC Voltage Droop Control and I-V Characteristics Schematics .....	71
Fig. 3. 14: A Simplified Equivalent Circuit for Two Sources Connected in Parallel Supplying a Load and Its Thevenin Equivalent [144].....	72
Fig. 3. 15: Point of Load Converter (buck) Schematics with Input Filter .....	73
Fig. 3. 16: Proposed DC Microgrid Equivalent Circuit Model .....	75
Fig. 3. 17: The set up of real-time simulation with OPAL-RT Simulator; (a) Simulink Model Using RT LAB, (b) Simulator Set-up Picture .....	76
Fig. 3. 18: DC Bus Reference Voltage.....	77
Fig. 3. 19: Simulation Result of Solar Power Components; (a) Irradiation, (b) Converter Output Current, (c) Converter Output Power, (d) Input Boost Converter Voltage, (e) Solar MPPT Reference Voltage .....	78
Fig. 3. 20: Simulation Result of Wind Generation Components; (a) Wind Speed, (b) Converter Output Current, (c) Converter Output Power, (d) Input to Boost Converter Voltage, (e) Wind MPPT Reference Voltage .....	80



Fig. 3. 21: G-VSC Output Parameters; (a) Current, (b) Power (watt), (c) DC Voltage .....	80
Fig. 3. 22: Battery Real-Time Simulation Results; (a) Current, (b) Power, (c) Voltage, (d) SoC .....	82
Fig. 3. 23: CPL Real-Time Simulation Results; (a) Output Current, (b) Output Power, (c) Input Power, (d) Input Current, (e) Output Voltage .....	83
Fig. 4. 1: Simplified DC Microgrid Source Circuit .....	87
Fig. 4. 2: CPL I – V Characteristic Curve .....	87
Fig. 4. 3: Load and Source Thevenin Equivalent Circuit Model .....	89
Fig. 4. 4: Load Buck Converter with Damped Input-Filter Circuit Diagram.....	91
Fig. 4. 5: Input Passive Damping Equivalent Circuit .....	92
Fig. 4. 6: Magnitude of Input Filter Output Impedance.....	92
Fig. 4. 7: Equivalent Circuit of Proposed DC $\mu$ G .....	94
Fig. 4. 8: Bode Plot of Control to Output (Gvd(s)) Without and With Undamped Input Filter.	95
Fig. 4. 9: Nyquist Plot of Control to Output (Gvd(s)) without Input Filter .....	96
Fig. 4. 10: Nyquist Plot of Control to Output (Gvd(s)) with Undamped Input Filter .....	96
Fig. 4. 11: Bode Plot of Gvds Buck DC / DC Load Converters with and without a Damped input filter .....	96
Fig. 4. 12: Nyquist Plot of Gvds Buck DC/DC POL Converter with Damped Input Filter .....	96
Fig. 4. 13: Converter Input and Source Output Impedance .....	97
Fig. A. 1: Proposed DC Microgrid Matlab/Simulink.....	117
Fig. A. 2: Real-Time Simulation Set up Using OPAL-RT Simulator .....	118




## LIST OF TABLES

Table 2. 1: G-VSC Parameter.....	32
Table 2. 2: Wind Turbine PMSG Parameters.....	36
Table 2. 3: Rated Wind Boost Converter Parameters .....	43
Table 2. 4: Rated Solar PV Boost Converter Parameters .....	48
Table 2. 5: Battery Bidirectional Converter Parameters.....	53
Table 3. 1: Power Flow Operation at Various Operating Modes.....	63
Table 3. 2: DC $\mu$ G Components Design Parameter .....	72
Table 3. 3: Bus Voltages at Different Operating Modes .....	77
Table 3. 4: System Parameter .....	81





## LIST OF ACRONYMS



AC	Alternating Current
BESS	Battery Energy Storage System
CIL	Control in the Loop
CPL	Constant Power load
CPS	Constant Power Source
CVC	Constant Voltage Control
DBS	DC Bus Signal
DC	Direct Current
DC $\mu$ G	DC Microgrid
DER	Distributed Energy Resource
DFIG	Doubly-Fed Induction Generator
DG	Distributed Generation
EMI	Electromagnetic Interference
ESS	Energy Storage System
FC	Fuel Cell
G-VSC	Grid-Connected Voltage Source Converter
HIL	Hardware in the Loop
HVAC	Heating, Ventilation, Air Conditioning
HVDC	High Voltage Direct Current
LCL	Inductor, Capacitor, Inductor
LRC	Line Regulating Converter
LVDC	Low Voltage Direct Current
MPPT	Maximum Power Point Tracking
P&O	Perturb and Observe
PCC	Point of Common Coupling
PFC	Power Factor Corrector
PLL	Phase-locked Loop
PMSG	Permanent Magnet Synchronous Generator
POL	Point of Load Converter
PV	Photovoltaic
PWM	Pulse Width Modulation
RES	Renewable Energy System

RMS	Root Mean Square
SCIG	Squirrel-Cage Induction Generator
SoC	State of Charge
SPWM	Sinusoidal Pulse Width Modulation
SRF	Synchronous Rotating Frame
SVPWM	Space Vector Pulse Width Modulation
THD	Total Harmonic Distortion
VCO	Voltage Controlled Oscillator
VSC	Voltage Source Converter
VSD	Variable Speed Drive
WECS	Wind Energy Conversion System
WRIG	Wound Rotor Induction Generator
WRSG	Wind Rotor Synchronous Generator
WT	Wind Turbine



## LIST OF SYMBOLS

C	Capacitance
$i_d$	d-axis Current
$I_{DC}$	DC Current
$I_{PV}$	PV Array Output Current
$i_q$	q-axis Current
$i_w$	Rectified Wind DC Current
$P_{ac}$	AC Power
$P_{Bat}$	Battery Power
$P_{DG}$	Distributed Generation Power
$P_{Load}$	Load Power
$R_d$	Droop Resistance
$V_{bus}$	Bus Voltage
$V_d$	d-axis Voltage
$V_{dc}$	DC Voltage
$V_{pv}$	PV Array Output Voltage
$V_q$	q-axis Voltage
$V_{sa}$	Phase A Line to Neutral Voltage
$V_{sb}$	Phase B Line to Neutral Voltage
$V_{sc}$	Phase C Line to Neutral Voltage
$V_w$	Wind Rectified DC Voltage
$V_\alpha$	$\alpha$ -axis Voltage
$V_\beta$	$\beta$ -axis Voltage
$\mu F$	Microfarad
kHz	Kilo Hertz
kW	Kilowatt
L	Inductance
mH	Mili Henery
P	Real Power
Q	Reactive Power
V	Voltage
$\beta$	Pitch Angle
$\theta$	Grid phase Angle
$\lambda$	Pitch Speed Ratio
$\omega$	Angular Frequency
$\Omega$	Ohm





# CHAPTER 1: INTRODUCTION

## 1.1. DC Microgrid Background and Motivation of the Research

A conventional fossil-fuelled based power generation system is facing challenges in a continuing reduction of fossil fuel resources. The traditional generation systems with fossil fuels require the transmission of electrical energy from generation place to distribution system or customer side. Consequently, this wastes more electricity in the transmission and distribution system since it is far from the user. Also, the fossil fuel-based generation system is not environmentally friendly [1], [2]. These challenges have led to the innovative development of the power generating system closer to the customer end within the distribution system using renewable and non-renewable energy resources. The power generation at a distribution voltage level referred to as distribution generation (DG). For increasing high-power quality demand and reliable power supply, energy storage systems (ESS) and DG utilization commonly more popular in recent times. The DG and ESS encompass small power network and ESS that can be interconnected with medium or low voltage distribution system locally through power electronic converters [3], [4].

Nowadays, the penetration of DG using RES becomes increasing in the distribution network because of the advancement of semiconductor device technologies [5]–[7], [8]. Accordingly, the utilization of renewable energy source distributed generation has been developed to provide power sources within the local distribution network. This increased reliability, efficiency, and flexibility for the local end-users. These generation systems can utilize both small-scale conventional energy generation technologies like gas and micro-turbines and non-conventional renewable energy generation technologies like photovoltaic (PV) panels, wind turbines (WTs), fuel cells (FCs), etc. [9], [10].

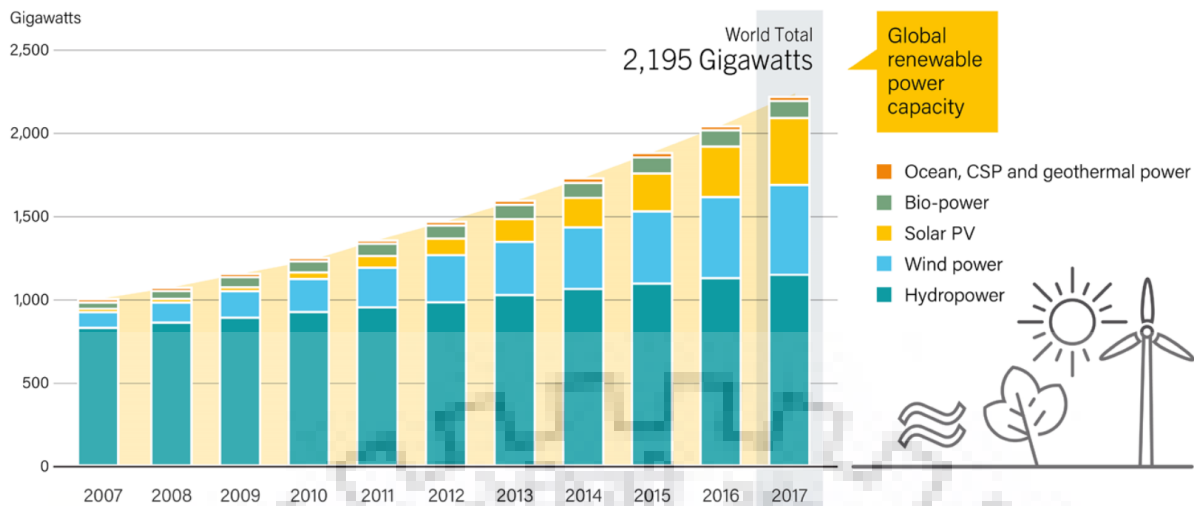


Fig. 1. 1: The Development of Renewable Energy Installed Capacity in the World [11]

The capacity of installed renewables in the world is increasing, as reported in renewable energy policy for the 21<sup>st</sup> century (REN21) (see Fig. 1.1) [11]. Hydropower constitutes the most significant amount among the total capacity of installed renewables in the past year. But nowadays, the ability of renewable energy resources like wind and solar has also been growing at a rapid rate.

However, the operation of the renewable energy sources presents several challenges due to their fluctuating output. It hence requires energy storage and grid-connection to support the power balance between energy production and consumption [12]. Thus, considerable developments can be achieved when heterogeneous distributed energy sources with easier grid integration and smart power managing features are used. To harmonize the inconsistency between the large grid and distributed power, and maximize the significance and welfares of the distributed energy, the concept of microgrid has been introduced [3], [13].

The microgrid is a cluster of micro sources, loads, and energy storage systems that work as a single controllable entity that can be operated independently or connected with the utility grid [13], [14]. Initially, the concept of microgrid introduced to satisfy local energy requirements by interfacing the DG sources to distribution lines at the substation or close to the customer side without the need for costly extension of the conventional central power grid.

Microgrids can be classified as AC, DC, or AC/DC hybrid based on the voltage and current types. Depending on the operation system, it can also be divided into two; grid-connected and islanded microgrids [15]–[17], [18]. Most energy sources, such as the battery energy system, fuel cell, and solar PV, are generating DC in nature. Nowadays, also DC-operated electronic

loads are developing that eliminate further power conversion stages, reducing costs and losses. Besides, in the DC system, reactive power control, synchronization concerns, and frequency control do not exist [19], [20]. The load side converters determine the quality of the DC microgrid power supply to the customer. Thus the appropriate use of the power electronic converter is to provide a tasty variety of electrical power for the end-users. The DC bus voltage is the only variable that uniquely determines the power balance and DC $\mu$ G quality. As a result, the DC microgrid is more comfortable to control, easier for multi-distributed power sources integration as compared to its AC counterparts [21].

In recent years, wind and solar distributed generations are becoming the most popular distributed renewable energy sources for microgrid applications. A hybrid wind and PV with a grid-connected system provides more reliability and higher quality power to the load than a system with a single source in the microgrid system [22]. In such an order, the power electronic converters are used for integrating the different distributed energy resources (DERs). The increasing number of renewable energy sources (RES) penetrations in the distribution network and the increased consumer energy demands from a nearby site, encouraged the deployment of DC $\mu$ G with multiple sources and energy storage opportunities to deal with the control, reliability, and stability problem in the integrated systems [23]–[25]. A DC $\mu$ G can be interfaced with different sources in parallel, each unit in the network participates in supporting each other via an integrated and power management control strategies. Consequently, this can provide various benefits such as the optimal operation of DC $\mu$ G subsystem through coordinated control scheme that maximize utilization of DGs and BESS [23], [26] and maintain the reliability and power balance of the DC $\mu$ G in case of generation and load disturbances [24], [25].

In 2004 Ito *et al.* [27] developed the first DC $\mu$ G experimental prototype claiming that simple control, higher reliability, and availability as well as more efficient than its AC microgrid counterpart. Afterward, several DC $\mu$ G projects were demonstrated in different applications like flexible DC distribution for telecom power supply [28], data centers [29], residential households [30], [31], and distributed energy resource plants [32]. Nowadays, DC $\mu$ G systems are acknowledged as a fundamental technology part of smart grid development. For example, an automotive industry uses 12V DC distribution systems to supply all the electronic/electrical devices of the vehicle [33], 48V DC supply is widely used in telecom distribution systems [28], and HVDC is used for undersea or long-distance electrical transmission. The DC $\mu$ G enables to increases of the power quality of the distribution network [34], [35], and it is suitable for RES generating DC output in nature since these sources eliminate unnecessary energy conversion

stages [36]. Power electronic converters are used to interface the generations to the DC bus. Besides, these converters employed to regulate and manage the source and load subsystem terminal parameters to interact with each other predictably and stably [37].

With the development of micro-grid control methods along with cost-effective and efficient power electronic converters, a DC $\mu$ G can become a promising solution for integrating DG sources, storages, and loads. However, to achieve stable and secure operation, proper control and stability strategies should be determined before DC $\mu$ Gs can become commonplace. Thus, in this study, suitable control strategies and stability improvement both in islanded and grid-connected modes are proposed. Different kinds of literature reported on DC $\mu$ Gs control schemes and stability analysis is described in the following section.

## **1.2. Literature Review**

In a hybrid source DC microgrid system, the RES supplies the average load demand. Whereas ESS and the AC grid supply are employed to regulate and support the power balance in the case of fluctuating output of distributed generation units within the distribution network. The DC $\mu$ G enables the system for proper integrated operation of the different micro sources such as DGs, ESS, grid-connected VSC, and loads with appropriate control and stability. Also, microgrid offers a suitable technical, operational, and economic benefit of enhanced optimized energy economics and reliability [38], [39]. Thus in the following section, the development of DC microgrid, the different kinds of the control system, stability, and application reviews are reported. The next section describes the detail of the literature reviews of the DC microgrid.

### **1.2.1. Historical Development of DC Microgrids**

In 2001 T. Ackermann *et al.* [10] presented the general definition of distributed generation as the generation of electric power at the distribution level. Additionally, the author described the meanings of distributed capacity, distributed utility, distributed resources, and network and connection issues of distributed generation. The intended purpose of the study was that the anticipation of distributed generation would have become more significant for the next power generation system. Later the idea of microgrid introduced in 2002 by R.H. Lasseter [13] as a future low voltage distribution systems paradigm that was practicing radical changes due to the beginning of the distributed generation. The design is based on a group of micro sources and loads into one typical unit could be deduced as a single dispatchable consumer from the overhead power system point of view.

A better way of microgrid system that enables the separate microgrid operation of generation and the associated loads has been proposed in [40]. Whenever disturbances occur, the corresponding loads and production will be disconnected from the distribution system to protect the microgrids load from the interference without affecting the grid transmission integrity. In 2004 A. Arulampalam *et al.* [41] have been proposed the concept of electronic power control in integrating generating sources, loads, and energy storage devices. The control scheme is intended for voltage regulation, frequency regulation, unbalanced current compensator, islanding, and grid-connecting operation. Similarly, the application of interfacing power converters of distributed generations, particularly PV generators, fuel cells, and wind power, was introduced for improving the power systems performance and efficiency [42].

Dushan Boroyevich *et al.* [43] reported that power electronic converters could support to improve system reliability, controllability, efficiency, and size in the AC and DC distribution system. For example, from the start of a computer power system, the study anticipates the possible forthcoming of AC and DC power electronic distribution system configurations, particularly in the existence of RES. The author also suggested that the control scheme achieves a hierarchical dynamic decoupling of distribution, consumption, and generation through the use of bidirectional converters as energy control centers. Patterson [44] has proposed DC micro-grids and the origin of the Enernet. The source of the earliest form of DC electrical voltage and its potential to change the world again discussed. The vision of the DC Micro-Grid-enabled "Enernet" represents an inevitable decentralization of the national network and should facilitate the current overhaul of the Smart Grid. Nowadays, the DC power system is becoming more popular solutions in different application areas such as electric vehicle charging, residential, automotive industry, and charging energy storage systems.

### **1.2.2. Control Strategies in DC Microgrids**

The increasing power demand for reliable and high power quality encouraged the small-scale power generation from DERs and ESSes that are connected to the low voltage DC power system. The control of the microgrid system ensures the seamless operation of the energy storage system and distributed generation with stable and equal current sharing among the parallel-connected power converters. As reported in the literature, many researchers investigated the AC microgrid since the conventional power system based on the AC system [45]–[49]. Currently, the DC $\mu$ G have received more popularity than AC counterpart because of



the benefits such as higher reliability, higher efficiency, low cost, absence of frequency or reactive power control and more straightforward analysis and design of control loops [50]–[52].

Moreover, in DC $\mu$ G different DER and ESSes are joined to the universal DC bus through power electronic converters. The integrated operations of ESSes and multiple DGs have fluctuating voltage levels with varying characteristics when coupled with the central DC microgrid system [53]. Accordingly, to ensure stable and effective integrated operation of a DC $\mu$ G, there are three control schemes usually employed. These are decentralized, centralized, and distributed control schemes. These control techniques are described in the following section.

### a) Centralized Control System

In the centralized control scheme, the central controller receives the detected signal from all the units. After that, the controller performs functions like sending instructions to each interfaced converters, deciding how much amount of power each group can contribute, and so on.

The central controller monitors the control decision as per the received measurement signals from each converter in the system and set up acceptable limit values. The control system employs a fast communication network to link it with the load and source subsystems, as depicted in Fig. 1.2. In the case of small-scale DC $\mu$ Gs, each unit in the system can be controlled directly by the central controller, which uses high-speed communication using a master/slave approach[54], [55].

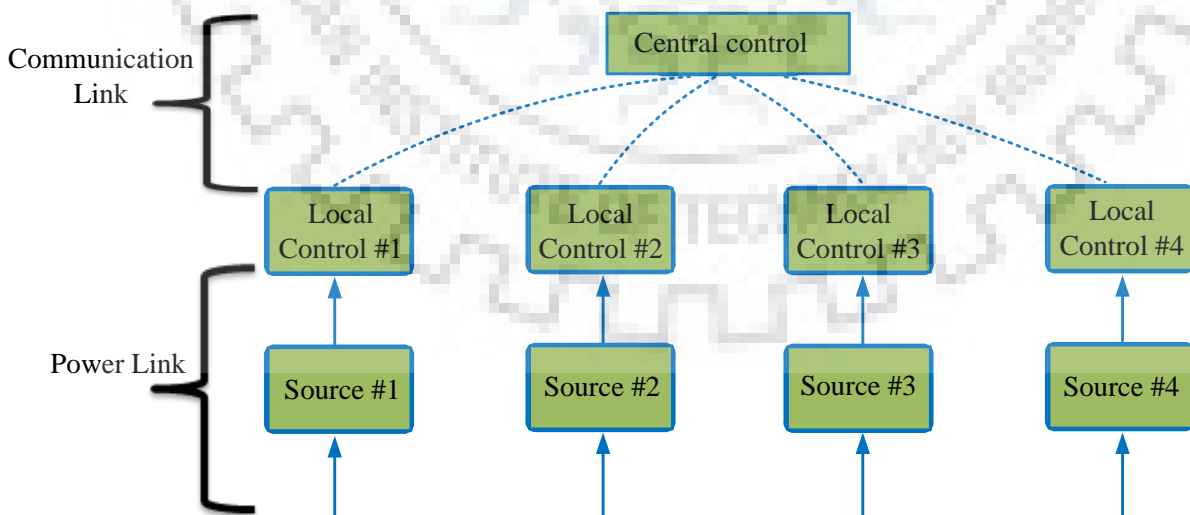


Fig. 1. 2: Central Control System Structure

However, for large DC $\mu$ Gs, hierarchical control is often a preferred choice because it introduces a degree of absolute independence between diverse levels. The hierarchical control

that achieved by the simultaneous use of a local converter control and a coordinated control based on a digital communication link and separated by at least an order of magnitude in the control bandwidth [56].

In [57], a hierarchical control system with a three-level control scheme proposed. The first control level includes primary control functions as it maintains the reliability of system operation in case of communication failure. In the secondary control level, it employs a consensus-based voltage controller to avoid the average voltage variations in the microgrids. This averaging method permits control of power flow between the microgrids [56]. The tertiary control regulates the power flow among the DC $\mu$ Gs and the external electrical distribution systems [58]. The hierarchical control method is used in [34] to optimize efficiency and the resilient operation of DC $\mu$ G. Supervisory control used to manage and balance the power of the system within a microgrid in [34], [59]. The practical application of a hierarchical controller and its interaction among different levels are detailed in [58], [60].

One of the best benefits of the centralized control scheme is that the central control system can able to realize global optimization based on information obtained from all units. But, the control technique is highly susceptible to single point failure, subsequently degrades reliability; moreover, the control strategy also suffers from a high computational burden. In [61], a centralized control technique is presented to interface the operation of different converters in DC $\mu$ G that connected in parallel. This control strategy implemented the model predictive control scheme for power-sharing and voltage control. However, this control mechanism degrades the system reliability, flexibility, and it is more susceptible to failure with a single point fault in the system. In [62], a master-slave control method for load sharing proposed. Similarly, this control solution also has a related problem with the central control, since the voltage control fails with the failure of the master-slave.

#### **b) Distributed Control System**

The distributed control scheme has no central control that requires communication links with all individual units. However, the different groups in the system communicate among themselves via dedicated digital communication links. In this control scheme, each local converter controllers work independently but interchange information with each other via a communication link to enhance global performance. One of the critical advantages of the distributed control scheme is that it maintains full system functions. Even though one communication link failure happens in the system, the other communication linkages remain

connected. The control principle employs a consensus algorithm within each local controllers in which it is unceasingly sum up all the errors of some variables targeting get the desired value in given local control units. The computational burden of global optimization also reduced by distributing the algorithm to local controllers.

In the distributed control algorithm, the communication system is flat and spans over the local controllers, unlike the multi-level control scheme and communication in case of hierarchical control approaches. Such type of communication network design is intricate, needing knowledge of graph theory. Specifically, the exchange of information only can happen between the two interconnected nodes and only comprise local information. The most uncomplicated distributed communication technique is using the standard bus voltage as a means of communication to combine all the local controllers. Thus, via this communication link, all local controllers could get access to other whole nodes without the need for a central controller. Hence, improvement in reliability can be achieved.

In the distributed control strategies, the voltage restoration and current sharing are the key issues. In [63], the voltage variation and current unbalance are distinguished in the DC<sub>u</sub>G system with increased virtual resistance. The control method uses a low bandwidth communication interface to calculate the overall average power flow delivered by each unit. Then after the value is used to evaluate the remuneration value required for the desired voltage reference. All the modifications supplied to the local controllers via the control loop.

Consequently, the bus voltage renovated to its desired value. In [64], the influence of time delay in a distributed control scheme discussed. It demonstrated that the control algorithm has a low time delay, but the system control stability is still guaranteed. The voltage shifting equalization technique is implemented in [65] to maintain the same amount of voltage shift within the converters during DC bus voltage restoration.

Nowadays, in many numbers of microgrid applications, consensus algorithms have been employed [66], [67]. A consensus algorithm based on low bandwidth communication was applied in [64] to control the average DC voltage and current by using two more extra PI controllers in the secondary control loop. As a result, the aim of enhanced current sharing accuracy and voltage restoration achieved at the same time. In [66], a dynamic consensus system is applied where a robust DC observer using the data from the neighboring DG developed to correct the desired local voltage references. A current regulator also included comparing the adjacent local currents to eliminate the load sharing errors.



To optimize the economic performance of a global droop controlled DC $\mu$ G dynamic consensus algorithm suggested in [67].

In [20] distributed control scheme operating with droop control that can facilitate maximum load transfer to load using the fuzzy logic controller is proposed. However, this control system has the drawback of complex computational analysis, slow communication, and vulnerability to measurement error. Many studies reported in [22], [68] proposed control of energy management methods primarily on islanded DC $\mu$ G by optimized usage of RES and ESS. However, such control approaches may lead to reduced reliability and create more burdens on ESS due to the intermittent behaviour of solar insolation and wind speed [22].

In conclusion, note that in the distributed control scheme, information awareness is comparable with the centralized control system. The distributed control offers improved reliability since it eliminates the single point of failure. However, the control method has limitations such as complex analysis, communication delay, and measurement errors.

### c) Decentralized Control System

The decentralized control scheme is implemented based on local control information. Each unit in the system controlled independently. The control structure can be achieved exclusively without employing a digital communication link, as shown in Fig. 1.3. Several decentralized control methods used to coordinate the performance of multiple hybrid sources that connected in parallel in DC $\mu$ G. The most commonly used are adaptive droop coefficient control, DC bus signaling, and power line communication.

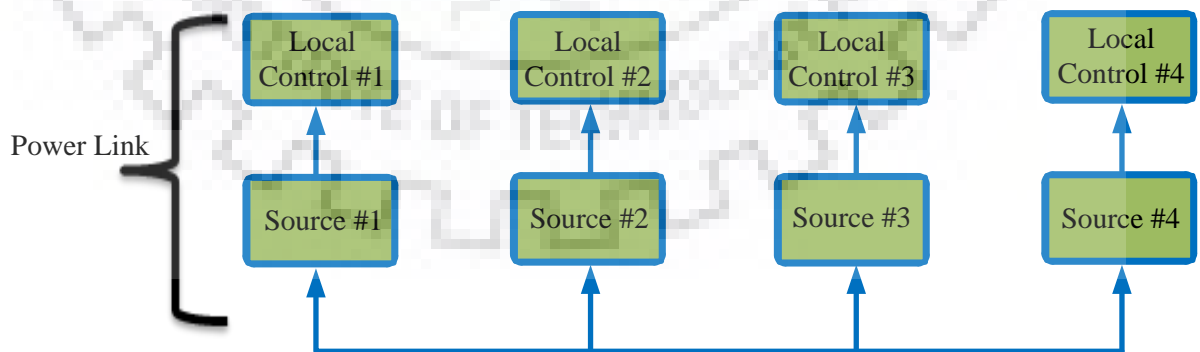


Fig. 1. 3: Decentralized Control System Structure

Initially, the concept of DC bus signaling was introduced in 2004 [69]. The DBS used as a means of scheduling power generation and load power-sharing to regulate the power balance in a decentralized approach in DC $\mu$ Gs comprising multiple hybrid generating sources. DBS relies

only on local information and does not require any components other than the interface converter. Therefore, it is a decentralized control method that is easy to implement. The main concern is the selection of suitable voltage levels that are required to identify different operating modes.

In [70], a decentralized control scheme based on an adaptive droop controller proposed for primary and secondary power-sharing in low voltage DC $\mu$ G. The local control functions such as voltage, current, and superimposed AC frequency parameters are utilized in the primary and secondary loop for the target power-sharing without the need for additional communication links. As a result, the reliability of the system is higher as compared to the system utilizing the communication network. An output constrained robust decentralized control method with parallel converters for a single bus DC $\mu$ G system presented in [71]. The control method guarantees a proportional load sharing and consistent performance of voltage regulation with a bounded transient response. In [72], a DC $\mu$ G with multiple renewable DGs and ESSs implemented using a mode adaptive decentralized control algorithm to maintain the power balance. The DC bus voltage utilized to allow load sharing among the various sources. Besides, it also used to determine the operation of the DC $\mu$ G modes as well as to enable seamless mode transitions. This control system allows performing local control variables in every interfacing converter to realize the power and voltage regulation. Also, every power converters in the method employed independent control without any communication link between different units.

### **1.2.3. Stability Issues in DC Microgrid**

The stability concern in DC $\mu$ G is the consequence of the energy conversion via interconnecting power converters between source and load subsystems to obtain different voltage ranges that required in case of integrating multiple sources, ESS and load components. Thus, the DC $\mu$ G architecture cascaded of a power distribution system where the interfacing power converters link the subsystems with different voltage levels [73]. The causes of stability problems in DC $\mu$ G are POL converters that immediate instability effect, DGs power output fluctuation due to input disturbances in nature, sudden load changing, and fault occurrences [74]. In DC $\mu$ G, loads classified as resistive and CPL. CPL typically maintained via a POL converter with sufficiently large bandwidth.

Note that load output power is equal to the POL converter input power regardless of the source voltage deviations [75], [76]. The influence of CPL on the stable system operation is conveyed

by its negative converter input impedance in the system dynamics. This negative resistance causes the system poorly damped and can cause stability problems and worsen the system operation [77]. To overcome the instability problems caused by non-linear CPL admittance or impedance-based design is proposed in [78]. In [79], stability analyzed for converters dynamic equation, and damping enhancement using frequency-dependent virtual impedance for DC $\mu$ G with the presence of CPL is discussed. Similarly, in [77], stability improvement using virtual impedance was proposed. Most of the DC $\mu$ G stability analyses reported in the literature are linear and based on small-signal review [77], [80].

The proposed DC $\mu$ G employed a decentralized control configuration using DBS. This methodology features a self-controlled operation of each interfacing converter without communication links. The stability problems mitigated by passive damping of the input filter applied at the input of point of load (POL) converters.

#### **1.2.4. Application of DC Microgrid**

Due to the recent development toward smart grid technology, together with the potential advantages of the DC power system, DC $\mu$ Gs have received more attention as a viable distribution alternative in various areas.

Advantageously, most of the loads in residential and office applications are DC supplied. Electronic appliances such as computers, laptops, tablets, phones [81], and DC supply used for lighting [82]–[85]. Modern DC supplied lighting technologies are more efficient. For example, solid-state lighting and compact fluorescent fixtures involve a DC stage. As a result, a DC distribution system is more valuable than their AC counterparts [86], [87]. DC supply used in variable speed drives (VSD) for heating, ventilation, pumps, and air conditioning (HVAC) systems, elevators, fans, and traction with front end inverter.

Additionally, industrial applications, the DC electric arc furnaces employed in the steel industry due it needs less energy than the equivalent AC and cause fewer flickers [88]. If the AC distribution system supplies the load, it adds conversion stages and, subsequently, the delivery chain results with reduced efficiency. According to [89], about 30% of the AC power generated passes via interfacing converters before consumed. The lost energy amount varies, but usually, it approximated in the range of 10-25% [44]. Consequently, the authors in [90] proposed that the efficiency of the power conversion approximately raised with 8% if a DC power supply utilized.

Furthermore, around 25% of saving attained by eliminating one rectifier and one power factor corrector (PFC) stage. Thus, DC $\mu$ Gs can be an alternative solution to supply individual buildings like data centers and banks. DC power systems are making a comeback to the AC system not as a competitor but as a partner where the DC supply system offers more advantages than the AC supply counterparts. The DC systems have advantages where distances are small, and DC loads are dominating. In data centers, loads such as computers, LED lighting, and adjustable speed drives for air conditioning powered by DC power. Also, DC $\mu$ Gs provide power for loads during transients and outages on the utility grid [91], [92]. Thus, nowadays, DC $\mu$ Gs has got numerous applications in industrial, residential, and commercial areas.

### **1.3. Challenges of the Research and Proposed Solution**

#### **1.3.1. Research Challenges**

The DC $\mu$ Gs are becoming more popular and drawing more attention with the integration of various DGs with a centralized battery energy storage system. Integrating multiple DGs in parallel via power electronic converters enables improved reliability and energy utilization in the microgrids. However, the generation output disturbance of DGs, sudden load change, and impedance mismatch among the source and load converters cause stability problems in the DC distribution system. The integrated operations of DC $\mu$ G with ESSes and multiple DGs have changing input characteristics and varying voltage levels. The various sources are interconnected in parallel through the power converters to the central DC grid system. Changing aspects of wind speed and solar irradiation, as well as the charging and discharging of the battery, affect the stability of the DC bus voltage. Consequently, due to the disturbances mentioned above, power unbalance and voltage instability results in the DC bus. The fluctuating output characteristics of DGs, the dynamic interaction between the source and load interfacing converters, and a sudden load changing cause a significant problem on DC bus voltage stability.

Typically, DC $\mu$ G is an interconnected distributed power topology, and the power converter interconnects between the portions of the system with various voltages levels. In such structures, instability in the system occurs due to the tightly controlled load side converters that act as CPLs (Constant Power Load), in which the small-signal model contains a negative input resistance. This negative incremental impedance causes the system poorly damped and can cause unstable poles in the frequency domain and worsen the system stability [1]. The intermittent character of the renewable energy sources and the continually changing power

consumption are also among the parameters that challenge the DC $\mu$ G power management system and hence, DC bus stability.

### **1.3.2. Proposed Solutions**

A hybrid wind and PV generation with a grid-connected system provides more reliable and higher power quality to the load than a system with a single source in a microgrid system. The increasing number of RES penetrations in the new distribution network and the increased consumer energy demands from a nearby site, encouraged the deployment of DC $\mu$ G with multiple sources and energy storage opportunities that deal with the control, reliability as well as stability problem in the integrated systems. Thus, in this study, a coordinated decentralized droop controlled strategy among the various sources has been implemented using the DC bus voltage signal (explained in detail in chapter 3). A DC $\mu$ G composed of wind-solar hybrid RES and BESS with grid-connected or islanded operations that allow flexible and reliable performance with seamless mode transition proposed. The control method employed the DC bus voltage level as a communication signal and let the autonomous control operation of each the interfacing converters without communication. The control methods for maximum power and constant voltage are used in the DGs interface converter to control the power and voltage fluctuations due to changing input conditions. The developed DC $\mu$ G control is implemented in real-time simulations with software control-in-the-loop (CIL) to verify the controller accuracy and performance through the OPAL-RT simulator.

In addition to improving the problem of DC bus oscillation due to electromagnetic interferences, the input filter applied between power sources and a load converter. Furthermore, to overcome the instability of the POL converter feedback control, the stability conditions using Nyquist stability, criterion analysis implemented.

### **1.4. The Research Objectives**

DC microgrid is an integration platform that encompasses storage units, micro sources, interconnecting units, and loads. The synergetic operation of these units can enhance the reliability and flexibility of the system. Thus, based on the gap identified from the literature survey, the objectives of the researches are described as follows:

- Modeling and autonomous control of each source units such as distributed generation (wind and solar), and grid-connected VSC under input disturbances.



- Investigation of appropriate control strategies for the stability of DC microgrid with source and load disturbances.
- Investigation of stability of a DC microgrid due to source disturbance with constant power loads.

All the objectives are validated using MATLAB/SIMULINK and real-time simulation.

## 1.5. Thesis Organization

Apart from this chapter, this thesis consists of four chapters. Each chapter's work descriptions summarized in the following.

In chapter two, the modeling and control of renewable energy sources (such as wind and solar), battery energy storage, and grid-connected VSC is described independently. An autonomous control scheme based on local functions like the current, voltage, and droop controls is employed through the power electronic converters that connect the source units to the typical DC grid.

Chapter three presented the existing DC microgrid topologies and also described the benefits and limitations of each topology. Based on the single bus DC microgrid topology, the integrated operation of DC $\mu$ G with different sources like wind, solar, BESS, and G-VSC through a decentralized control structure with input source disturbance explanation is given. The DC bus signaling control technique that employs the DC bus voltage as the communication link to determine the various operating modes depending on the status of generating source input also discussed. Three different ways of operations are explained based on the changing generation output power and sudden load switching. The proposed DC $\mu$ G model is developed in Matlab/Simulink SimPowerSystems and verified with real-time simulation using OPAL-RT is presented.

Chapter four describes the different causes of the stability problem in DC microgrids. It elaborates stability problems due to the source and load converter impedance mismatches, as well as due to the uncertainties of DGs operation and method of improvement was described. In the chapter, the input filter design and analysis for stability problem mitigation with optimum damping of input filter design are implemented. Besides, several decentralized control methods used the control technique to overcome the instability of the POL converter feedback control explained in the chapter. The load converter, control loop instability problem examined using

the Nyquist stability criterion. The source output and load input impedance investigated to quantify the system stability.

Chapter five summarizes the significant contribution of works performed in this thesis and states the further future research area to investigate.







## **CHAPTER 2: DC DISTRIBUTED ENERGY RESOURCE MODELLING AND CONTROL**

The DC power distribution systems have been drawing significant attention and have shown the potential to compete with conventional AC systems [50], [4]. DC $\mu$ Gs are based on direct current technologies and consist of DER and loads operating in a controllable and synchronized way either in a grid-connected or islanded manner [93]. Most energy sources such as solar PV, fuel cell, and battery energy system are generating DC in nature. Nowadays, also DC operated electronic loads are developing that eliminates further power conversion stages reducing costs and losses. To date, DC $\mu$ G is getting more preference than its AC counterparts. Because of numerous benefits such as the direct connection of native DC loads with renewables natively generate low voltage DC power, more straightforward control system compared to AC counterparts, higher reliability, and efficiency [52], [53], [64], [75]. Furthermore, the DC power system is gaining attraction in low voltage applications; for example: in modern electronic DC loads at home (LED lights, phones, TVs, laptops, and so on), in academia, and so on.

In the DC power system, power electronics are a crucial element for the energy conversion and for allowing control of the bus voltage and power flow of the system. Due to the advancements in the semiconductor technology and power converters, the microgrid's topology has received more popularity with the integration of ESSes and DERs [94]. Thus, the power converter plays an essential role in the combination of renewable energy sources into the electrical grid. Also, it is widely used and rapidly expanding as these applications become more integrated with the grid-based systems. The distributed generation is a small power scale located close to the customer side. It can operate with a connection to the utility grid or independently. The commonly used DG sources are solar PV, wind generation, fuel cell, microturbine, and small hydropower. In this chapter, DC distributed energy sources along with the interfacing converter to the DC grid, and their control methods described independently. Finally, these distributed sources integrated or connected in parallel in a decentralized fashion by using a single DC bus topology and hence can get supply from the universal DC bus. In this chapter, grid-connected VSC, wind generation, solar PV, and BESS are described.

## 2.1. Grid-Connected Voltage Source Converter System (VSC)

A VSC is one of the main elements in microgrids and DGs for interconnecting the AC grid and DGs, such as the wind power system with the DC grid [4], [94]. In low voltage DC $\mu$ G applications, a three-phase two-level VSC is commonly used.

Different control schemes reported in the literature for VSC to address the control of power and voltage balance of the power converters. Feedback control systems employed, and these controllers have an advantage, such as robustness and adaptability of disturbance rejection in the grid as compared to the open-loop control system [4], [95]. In this thesis, a current mode vector control approach using a typical direct PI controller employed. Averaging and linearization used in linear controller design that allows the control action to change continuously despite the discrete number of the possible switching state of the converter. The control system allows using necessary pulse width modulation (PWM) techniques such as space vector PWM (SVPWM) [96] to transform the output voltage reference from the current controller into the switching signals sent to the actual converter switching devices. For the computation of the controller output, usually, a variable transformation matrix is applied to the measured magnitudes.

### 2.1.1. Voltage Source Converter (VSC) Modeling

The three-phase VSC is employed to convert a three-phase grid AC power supply to DC voltage with input power factor control. The schematic diagram of the three-phase two-level VSC illustrated in Fig. 2.1.

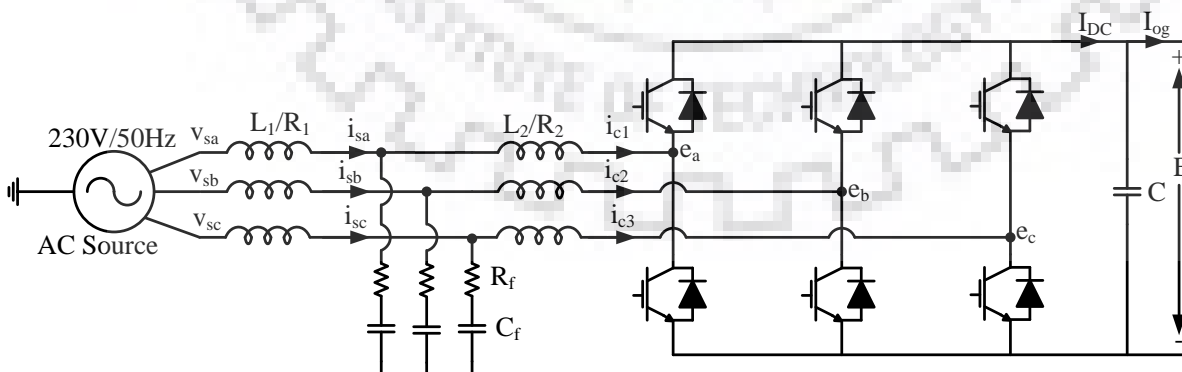


Fig. 2. 1: Grid-Connected Voltage Converter (G-VSC)

The VSC interfaced to the AC grid system through an  $L_1C_fL_2$  filter. The  $L_1C_fL_2$  filter constructed from three-phase coupled inductors ( $L_1$ ) with resistances  $R_1$  on the grid side, three-

phase coupled inductors ( $L_2$ ) with resistances  $R_2$  on the converter side, and three-phase star-connected filter capacitors ( $C_f$ ) each of them damped with resistances  $R_f$ . The voltage represents the AC grid sources  $V_{sa}$ ,  $V_{sb}$ ,  $V_{sc}$  on phase A, phase B, and phase C respectively, in series with the coupled inductors ( $L_1$ ) whereas  $e_a$ ,  $e_b$ ,  $e_c$  represent the VSC AC terminal voltages on phases A, B, and C, respectively.  $I_{sa}$ ,  $I_{sb}$ ,  $I_{sc}$  are the grid side line currents and  $i_{c1}$ ,  $i_{c2}$  and  $i_{c3}$  are the converter line currents. The converter can be modeled as a current source and a capacitor from the DC side of the system, whereas on the AC side, it is shaped by AC voltage sources [4].

The DC side current source reveals that the real power exchange between the DC and AC sides and guarantees the power balance of the system. Neglecting the losses in the converter, the DC load ( $I_{DC}$ ) in Fig. 2.1 can be calculated by:

$$I_{DC} = \frac{P_{ac}}{E}$$

The grid side source voltages can be expressed by [97]:

$$\left. \begin{aligned} V_{sa}(t) &= \hat{V}_s \cos(\omega_0 t + \theta_0) \\ V_{sb}(t) &= \hat{V}_s \cos(\omega_0 t + \theta_0 - \frac{2\pi}{3}) \\ V_{sc}(t) &= \hat{V}_s \cos(\omega_0 t + \theta_0 - \frac{4\pi}{3}) \end{aligned} \right\} \quad (2.1)$$

Where  $\hat{V}_s$  is the line to neutral amplitude voltage,  $\omega_0$  is the fundamental grid frequency, and  $\theta_0$  represent the initial phase angle of the AC grid supply. The equivalent space phasor of three-phase voltage is stated, as shown in (2.2).

$$\vec{V}_s(t) = \hat{V}_s e^{j(\omega_0 t + \theta_0)} \quad (2.2)$$

The dynamics of the VSC from the AC side can be designated by:

$$L \frac{d\vec{i}_s}{dt} = -R\vec{i}_s + \vec{V}_t - \vec{V}_s \quad (2.3)$$

Where  $R$  is the equivalent cable resistances of the line and  $i_s$  the grid side line current.

Replacing  $\vec{V}_s$  from (2.2) in (2.3), it deduced as:

$$L \frac{d\vec{i}_s}{dt} = -R\vec{i}_s + \vec{V}_t - \hat{V}_s e^{j(\omega_0 t + \theta_0)} \quad (2.4)$$

Equation (2.4) expressed in dq-frame form by replacing  $\vec{i}_s = i_{dq}e^{j\rho}$  and  $\vec{V}_t = V_{tdq}e^{j\rho}$  in (2.4), and realized:

$$L \frac{d}{dt} (i_{dq}e^{j\rho}) = -R(i_{dq}e^{j\rho}) + (V_{tdq}e^{j\rho}) - \widehat{V}_s e^{j(\omega_0 t + \theta_0 - \rho)} \quad (2.5)$$

The equation (2.5) is realized separately in real and imaginary components;

$$L \frac{di_d}{dt} = \left( L \frac{d\rho}{dt} \right) i_q - Ri_d + V_{td} - \widehat{V}_s \cos(\omega_0 t + \theta_0 - \rho) \quad (2.6)$$

$$L \frac{di_q}{dt} = - \left( L \frac{d\rho}{dt} \right) i_d - Ri_q + V_{tq} - \widehat{V}_s \sin(\omega_0 t + \theta_0 - \rho) \quad (2.7)$$

Equation (2.6) and (2.7) expressed in a standard state-space form with the introduction of a new control variable  $\omega$ , where  $\omega = d\rho/dt$  and yields;

$$L \frac{di_d}{dt} = L\omega(t)i_q - Ri_d + V_{td} - \widehat{V}_s \cos(\omega_0 t + \theta_0 - \rho) \quad (2.8)$$

$$L \frac{di_q}{dt} = -L\omega(t)i_d - Ri_q + V_{tq} - \widehat{V}_s \sin(\omega_0 t + \theta_0 - \rho) \quad (2.9)$$

$$\frac{d\rho}{dt} = \omega(t) \quad (2.10)$$

It realized from (2.8) – (2.10) is that,  $V_{td}$ ,  $V_{tq}$ , and  $\omega$  are the control inputs and  $i_d$ ,  $i_q$ , &  $\rho$  are the state variables. The dynamic equations expressed in (2.8) – (2.10) are non-linear due to the terms  $\omega i_d$ ,  $\omega i_q$ ,  $\cos(\omega_0 t + \theta_0 - \rho)$ . Suppose that  $\rho$  has zero initial condition and  $\omega(t) \equiv 0$ . As a result, if  $\rho$  continues to zero all the time, then (2.8) and (2.9) are modified to the following.

$$L \frac{di_d}{dt} = -Ri_d + V_{td} - \widehat{V}_s \cos(\omega_0 t + \theta_0) \quad (2.11)$$

$$L \frac{di_q}{dt} = -Ri_q + V_{tq} - \widehat{V}_s \sin(\omega_0 t + \theta_0) \quad (2.12)$$

Suppose that, if  $\omega_0 = \omega$  and  $\rho(t) = \omega_0 t + \theta_0$ , then (2.8) and (2.9) is simplified to (2.13) and (2.14);

$$L \frac{di_d}{dt} = L\omega_0 i_q - Ri_d + V_{td} \quad (2.13)$$

$$L \frac{di_q}{dt} = -L\omega_0 i_d - Ri_q + V_{tq} - \widehat{V}_s \quad (2.14)$$

From (2.13) and (2.14) it can be realized that the system is a linear second-order excited by constant input  $\widehat{V}_s$ . Therefore, if  $V_{tq}$  and  $V_{td}$  constant DC variables, then  $i_d$  and  $i_q$  are also

continuous DC variables. The technique to ensure  $\rho(t) = \omega_0 t + \theta_0$  is denoted as the PLL system.

### a) Design of LCL Filter

As shown in Fig. 2.1, a filter is used at the point where VSC coupled to the grid side to reduce the high harmonic content due to the switching frequency ripple. The LCL filter is used in grid-connected VSC [98], [99] due to their capability to minimize harmonic current distortions that can be injected into the grid [100].

### b) LCL Filter Modelling

An equivalent circuit diagram of the LCL filter model for the single-phase circuit shown in Fig. 2.2, where  $L_1, L_2$  represent the filter inductance of the grid and the converter side;  $i_c, i_g$  &  $i_f$  are the current on the converter side, the power flow on the grid side, and the current through the filter capacitor [100]. Assuming the star connected capacitor LCL filter modeling is carried out. Accordingly, the state space equation of the single-phase LCL circuit shown in Fig. 2.2 derived by neglecting the cable resistances and it is described by:

$$\begin{aligned} \frac{dv_c}{dt} &= \frac{1}{C_f} (i_s - i_c) \\ \frac{di_s}{dt} &= \frac{1}{L_2} (V_s - R_f(i_s - i_c) - V_c) \\ \frac{di_c}{dt} &= \frac{1}{L_1} (V_c + R_f(i_s - i_c) - V_{conv}) \end{aligned} \quad (2.15)$$

Representing (2.15) in matrix form:

$$\begin{bmatrix} \frac{di_c}{dt} \\ \frac{di_s}{dt} \\ \frac{dV_c}{dt} \end{bmatrix} = \begin{bmatrix} -\frac{R_f}{L_2} & \frac{R_f}{L_2} & \frac{V_c}{L_2} \\ \frac{R_f}{L_1} & -\frac{R_f}{L_1} & -\frac{V_c}{L_1} \\ -\frac{1}{C_f} & \frac{1}{C_f} & 0 \end{bmatrix} \begin{bmatrix} i_c \\ i_s \\ V_c \end{bmatrix} + \begin{bmatrix} -\frac{1}{L_1} & 0 \\ 0 & \frac{1}{L_2} \\ 0 & 0 \end{bmatrix} \begin{bmatrix} V_{conv} \\ V_s \end{bmatrix} \quad (2.16)$$

$$\dot{x} = Ax + Bu \quad (2.17)$$

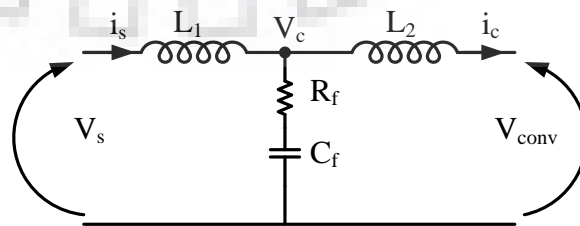


Fig. 2. 2: Single-Phase LCL Equivalent Circuit

Assuming  $v_g = 0$ , the filter transfer function is expressed by:

$$G_{LCL}(s) = \frac{sC_f R_f + 1}{s^3 L_1 C_f L_2 + s^2 C_f (L_1 + L_2) + s(L_1 + L_2)} \quad (2.18)$$

The frequency response of the filter transfer function using the Bode plot shown in Fig. 2.3 with and without damping resistance. As observed in the figure the addition of damping resistance together with filter capacitor avoids the resonant peak, attenuating the system response and moves the phase margin to  $-180^\circ$  at high frequencies.

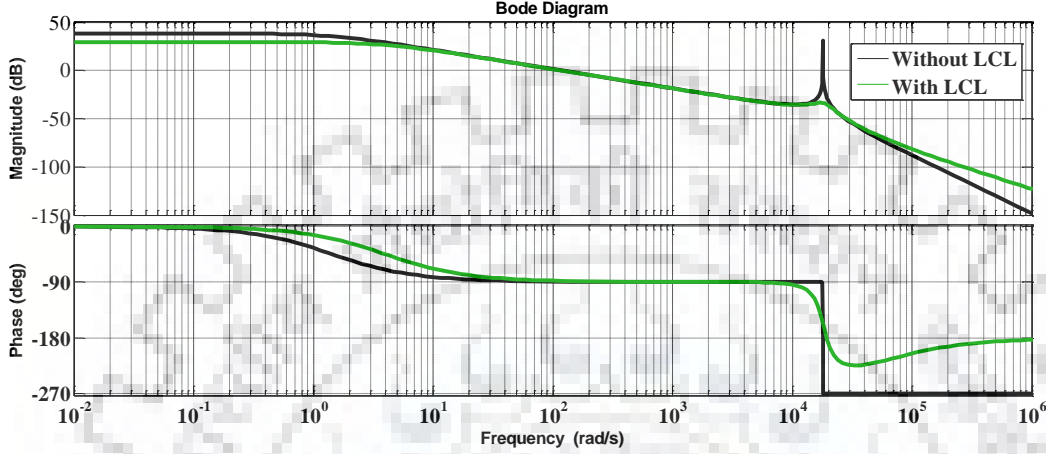


Fig. 2. 3: Frequency Bode Plot of LCL Filter

Parameters required for the calculation of filter components are; line-line RMS voltage ( $V_{L-L}$ ), grid frequency ( $f_g$ ), DC-link voltage, rated active power ( $P_n$ ), resonance, and switching frequencies. The parameters used for the design are  $V_{L-L} = 400$  V,  $P_n = 5$  kW,  $f_g = 50$  Hz and  $f_{SW} = 5$  kHz then the system base capacitance and impedance can be calculated by:

$$z_b = \frac{V_{L-L}^2}{P_n} = 32\Omega \quad (2.19)$$

$$C_b = \frac{1}{\omega_g z_b} \approx 100\mu\text{F} \quad (2.20)$$

Suppose that the maximum power factor deviation realized by the AC grid supply is 5 % to determine the filter capacitor. Accordingly, the filter capacitor found to be  $C_f = 0.05 * C_b = 5\mu\text{F}$ .

Similarly, the base current calculated as:

$$I_b = \frac{P_n * \sqrt{2}}{3 * V_{p-rms}} = 10.25\text{A} \quad (2.21)$$

The filter inductor ( $L_2$ ) from the converter side is calculated by adopting 2.7% of the base impedance and assuming that at this impedance value, a 10% current ripple obtained. Thus, from (2.19), 2.7% of the base impedance value is given by [101].

$$X_{L2} = 0.027 * 32 = 0.864\Omega \quad (2.22)$$

The inductance value obtained from the equation  $X_{L2} = 2\pi f_n L_2$  and calculated as follow:

$$L_2 = \frac{X_{L2}}{2 * \pi * f_n} = 2.75\text{mH} \quad (2.23)$$

Similarly, the grid side inductance is also approximated by adopting 1.8% of the base impedance and assuming a ripple attenuation factor of less than 20%. With these assumptions, the new impedance obtained.

$$X_{L1} = 0.018 * 32 = 0.576\Omega \quad (2.24)$$

and from (2.24) the inductance is calculated as:

$$L_1 = \frac{X_{L1}}{2 * \pi * f_n} = 1.8\text{mH} \quad (2.25)$$

Typically, the resonant frequency of the system is taken as one-half of the switching frequency and in this system;  $f_{\text{res}} = 2.5\text{kHz}$ . Accordingly, the impedance of filter capacitance at the resonant frequency is given by:

$$X_c = \frac{1}{2 * \pi * f_{\text{res}} C_f} = 12.73\Omega \quad (2.26)$$

The damping resistance selected to be one-third of the impedance at the resonant frequency that is  $R_f = 4.24\Omega$ .

## 2.1.2. Active and Reactive Power Control

### a) The Synchronous Rotating Frame (SRF) transformation

The stationary reference frame is useful in various applications; however, it is oscillating similar to the abc quantities. As a result, for VSC employing vector control technique, constant DC quantities are required for the controller design. Thus synchronously rotating dq reference frame is needed to obtain the continuous variables [102]. The grid side voltage  $V_{sa}$ ,  $V_{sb}$  and  $V_{sc}$  is sensed and converted to a stationary reference frame  $V_\alpha$  &  $V_\beta$  as shown in (2.28) and this stationary frame further switched to synchronously rotating reference frame (SRF)  $V_{sq}$  and  $V_{sd}$  (2.30). When VSC operates in rectifier operating mode, the voltage vector  $\bar{V}_s$  is aligned with the q – axis and the d – axis lags the q – axis by  $90^\circ$  as illustrated in Fig. 2.2 [102].

The grid voltage represented as:

$$V_{sabc} = V_m * \begin{pmatrix} \cos\theta \\ \cos(\theta - \frac{2\pi}{3}) \\ \cos(\theta + \frac{2\pi}{3}) \end{pmatrix} \quad (2.27)$$

Where  $V_{abcs} = [V_{as} \quad V_{bs} \quad V_{cs}]^T$  and  $V_m$  is the peak of phase voltage. If the system is balanced, (2.1) can be expressed in a stationary reference frame as:



$$V_{\alpha\beta} = T * V_{abcs} \quad (2.28)$$

Where  $V_{\alpha\beta} = [V_\alpha \ V_\beta]^T$  and T denotes a vector matrix defined by:

$$T = \frac{2}{3} \begin{bmatrix} 1 & -\frac{1}{2} & -\frac{1}{2} \\ 0 & \frac{\sqrt{3}}{2} & -\frac{\sqrt{3}}{2} \end{bmatrix} \quad (2.29)$$

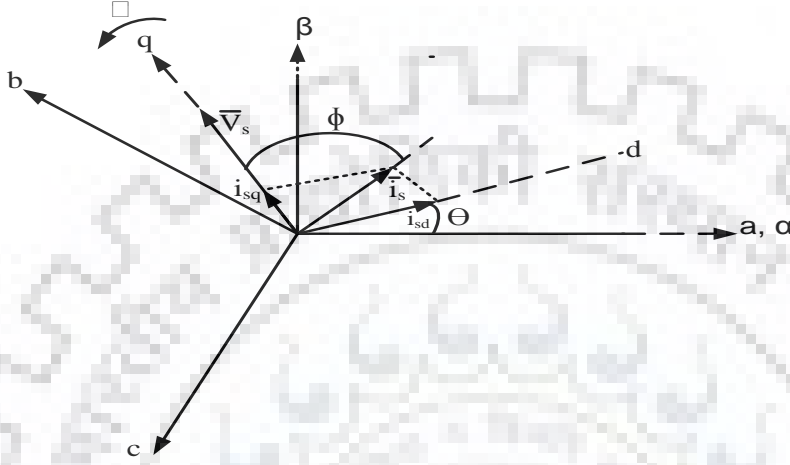


Fig. 2. 4: d-q axis Alignment Diagram

The rotating synchronous reference frame [103] using (2.28) determined as:

$$V_{qd} = B * v_{\alpha\beta} \quad (2.30)$$

Where  $V_{qd} = [V_q \ V_d]^T$  and B denotes the rotating matrix given by:

$$B = \begin{pmatrix} -\sin\theta^* & \cos\theta^* \\ \cos\theta^* & \sin\theta^* \end{pmatrix} \quad (2.31)$$

Substituting (2.27) and (2.28), into (2.30), the voltage  $V_q$  and  $V_d$  is obtained as [103],[104]:

$$\begin{bmatrix} V_q \\ V_d \end{bmatrix} = \begin{bmatrix} \cos(\theta^* - \theta) \\ \sin(\theta^* - \theta) \end{bmatrix} = \begin{bmatrix} \cos(\Delta\theta) \\ \sin(\Delta\theta) \end{bmatrix} \quad (2.32)$$

The required voltage magnitude the q-axis component and can be obtained as:

$$V_q = E_m \sin\rho \equiv e \quad (2.33)$$

Where  $E_m = -V_m$  and  $\rho = \theta - \hat{\theta}$ . The grid system frequency derived as:

$$\omega = \frac{d\hat{\theta}}{dt} = G_f * e \quad (2.34)$$



Where  $G_f$  denotes the loop filter gain. Assuming the phase difference  $\rho$  is very small, (2.21) can be linearized as:

$$e \cong E_m \delta \quad (2.35)$$

The electrical voltage angle  $\theta$  is employed in the SRF to obtain constant DC quantities.

Converting abc currents and voltages to the SRF, the following voltage and current phasors achieved.

$$\underline{V}^{qd} = \frac{V_q - jV_d}{\sqrt{2}} \quad (2.36)$$

$$\underline{I}^{qd} = \frac{i_q - ji_d}{\sqrt{2}} \quad (2.37)$$

A three-phase power formulated as:

$$\underline{S} = P + jQ = 3\underline{V}^{qd}\underline{I}^{qd*} = 3\left(\frac{V_q - jV_d}{\sqrt{2}}\right)\left(\frac{i_q + ji_d}{\sqrt{2}}\right) \quad (2.38)$$

Simplifying and rearranging (2.38), active and reactive power can be found by [105]:

$$P = \frac{3}{2}(v_q i_q + v_d i_d) \quad (2.39a)$$

$$Q = \frac{3}{2}(v_q i_d - v_d i_q) \quad (2.39b)$$

### b) Advanced PLL Control Using Lead Compensator

In a microgrid, grid connection is necessary for supporting the local distributed renewable generations like wind and solar in which the power generation is intermittent due to the changing environmental conditions. In this case, the grid system should maintain the power factor control to provide the generated power without energy losses [102]. Thus, accurate phase information must be sensed and delivered to the VSC control system for proper active and reactive power regulation. On other hands, the dq quantities that obtained from abc to dq transformations contain sinusoidal components such as the double frequency ( $2\omega_0$ ) signal with the DC quantities [97]. These sinusoidal components exhibit oscillations that are modulated with controller and feedback variables via these transformations.

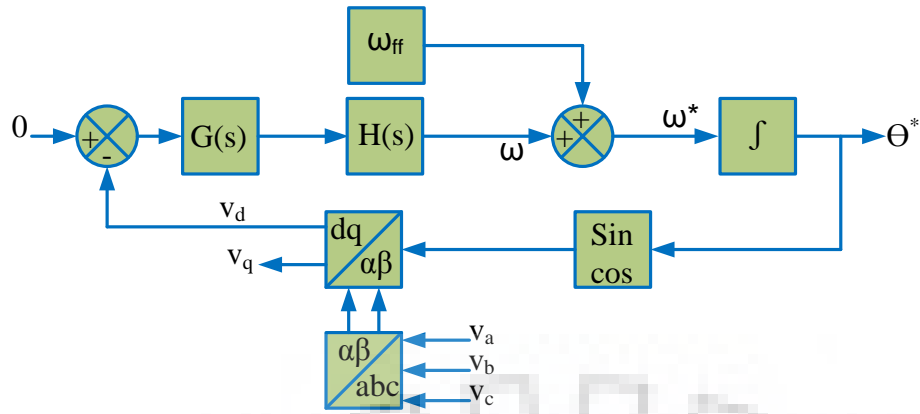


Fig. 2. 5: PLL Control Block

Consequently, the PLL is required to regulate the double harmonic frequency and oscillations to control the phase angle and frequency of the grid supply constant. The control scheme illustrated in Fig. 2.5, and as shown in the figure PI controller represented by  $G(s)$  is applied to decrease the phase error of AC components. Thus, it should note that if the difference in angle ( $\Delta\theta$ ) between the PLL output  $\theta^*$  and grid angle  $\theta$  is kept zero, then  $V_q = V_m$  and  $V_d = 0$ , as shown in Fig. 2.6. The voltage-controlled oscillator (VCO) employed to generate the phase angle and frequency from the low pass filter (PI controller). Using only the PI controller has a limitation that the phase detector generates oscillations or harmonic distortion at the double frequency of the input signal [106].

Accordingly, to solve the problem of double frequency content in the input signal, the lead compensator  $H(s)$  is implemented to attenuate a notch peak frequency at  $2\omega_0$  due to fundamental negative-sequence coupling. Also, it enhances stability by increasing the phase margin [97].

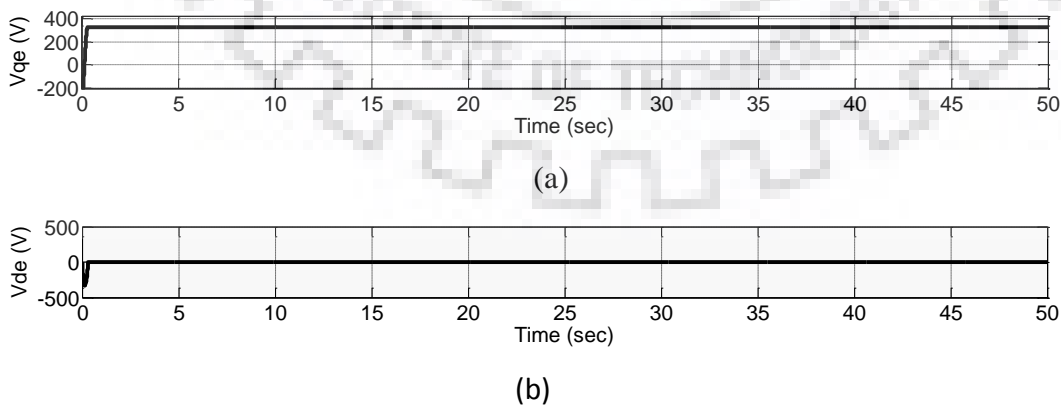


Fig. 2. 6: qd-axis voltage, (a) q-axis voltage, (b) d-axis voltage

Fig. 2.5 shows the PLL control diagram in which  $V_{sabc}$  is the input described in (2.27), where  $\hat{V}_s = 325V$  and  $\omega_0 = 2\pi * 50$  rad/sec. The compensator  $H(s)$  designed by considering one pole at the origin and complex conjugate zeros  $s = \pm j2\omega_0$  to eliminate the double frequency oscillation. Then the compensator transfer function is given by:

$$H(s) = \left( \frac{h}{\hat{V}_{sn}} \right) \frac{s^2 + (2\omega_0)^2}{s(s + 2\omega_0)^2} N(s) \quad (2.40)$$

Where  $N(s)$  is the lead controller transfer function and  $\hat{V}_{sn}$  is the nominal value of  $\hat{V}_s$ . The lead compensator designed by assuming the required phase margin of  $60^\circ$  and gain cross over frequency  $\omega_c = 167$  rad/sec. The compensator provides an optimum phase boosting to the loop gain. Accordingly,  $N(s)$  consists of two cascaded lead compensators, each to provide  $45^\circ$  at  $\angle l(j167)$ . As a result, the transfer function for  $N(s)$  derived as:

$$N(s) = \left( \frac{s+69}{s+403} \right)^2 \quad (2.41)$$

Substituting (2.41) in (2.40), the compensator transfer function becomes:

$$H(s) = \frac{1.8 \cdot 10^2 (s^2 + 394784)(s^2 + 138s + 4761)}{s^2 (s^2 + 1257s + 394786)(s^2 + 806s + 162409)} \quad (2.42)$$

Fig. 2.7 shows the frequency response of  $H(j\omega)$ . As observed in the figure that the magnitude drops with a slope of  $-40$  dB/dec, for  $\omega_c = 167$  rad/sec. But, around the  $\omega_c$  the slope of the magnitude reduces to about  $-20$  dB/dec, and the magnitude of the loop gain rises to  $-120^\circ$  at  $\omega = \omega_c$ . Thus, this is a desired characteristic because of the AC components of  $V_d$  due to harmonic distortion of  $V_{sabc}$ , attenuated.

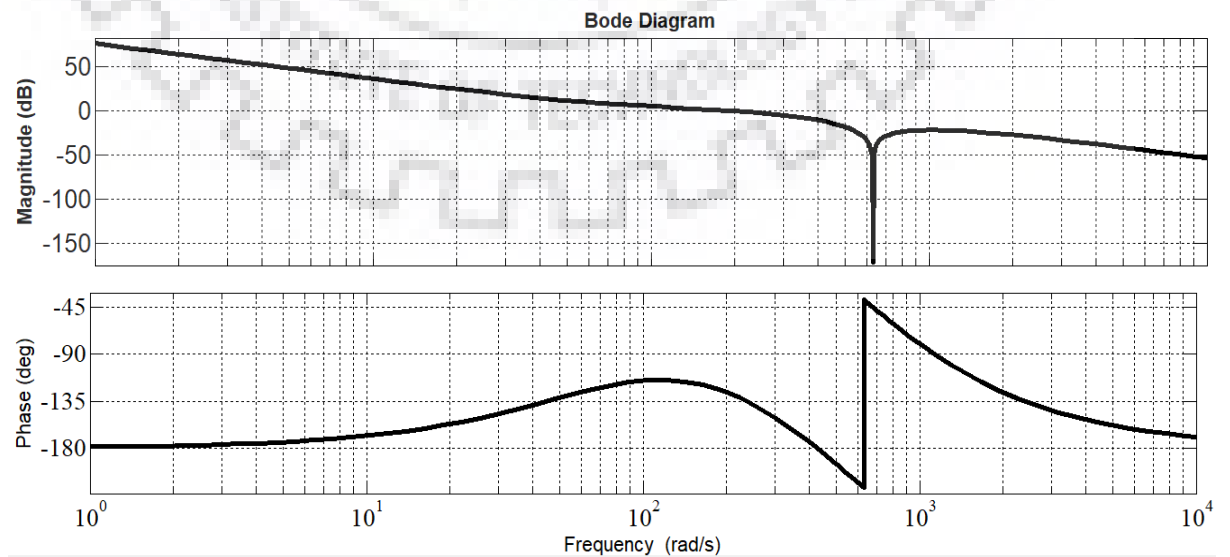


Fig. 2. 7: PLL Compensator Result

### c) Current Control Scheme

In the analysis of VSC employing vector control strategies, three-phase currents and voltages transformed into two-phase reference frames. The transformed grid side voltage and line currents are used as feedback parameters for the inner current control loop, as shown in Fig. 2.8. The active power is regulated through the inner q-axis current control loop while reactive power controlled via the d-axis current control loop due to  $i_{sq}$  is a measure of P and similarly  $i_{sd}$  signify a measure of Q, as described in (2.27) [102]. The feed-forward terms  $\omega L i_{sq}$  and  $-\omega L i_{sd}$  are combined with the inner current control system to allow effective decoupled control of the  $i_{sq}$  and  $i_{sd}$ .

The reference currents  $i_{qref}$  and  $i_{dref}$  are calculated from the real and reactive power references  $P_{ref}$  and  $Q_{ref}$  that formulated using the instantaneous power theory described in (2.27). The  $V_d = 0$  maintained by the PLL control system and substituting this in (2.27) the reference currents can be formulated as

$$i_{qref} = \frac{2 P_{ref}}{3 V_q} \quad (2.43a)$$

$$i_{dref} = \frac{2 Q_{ref}}{3 V_q} \quad (2.43b)$$

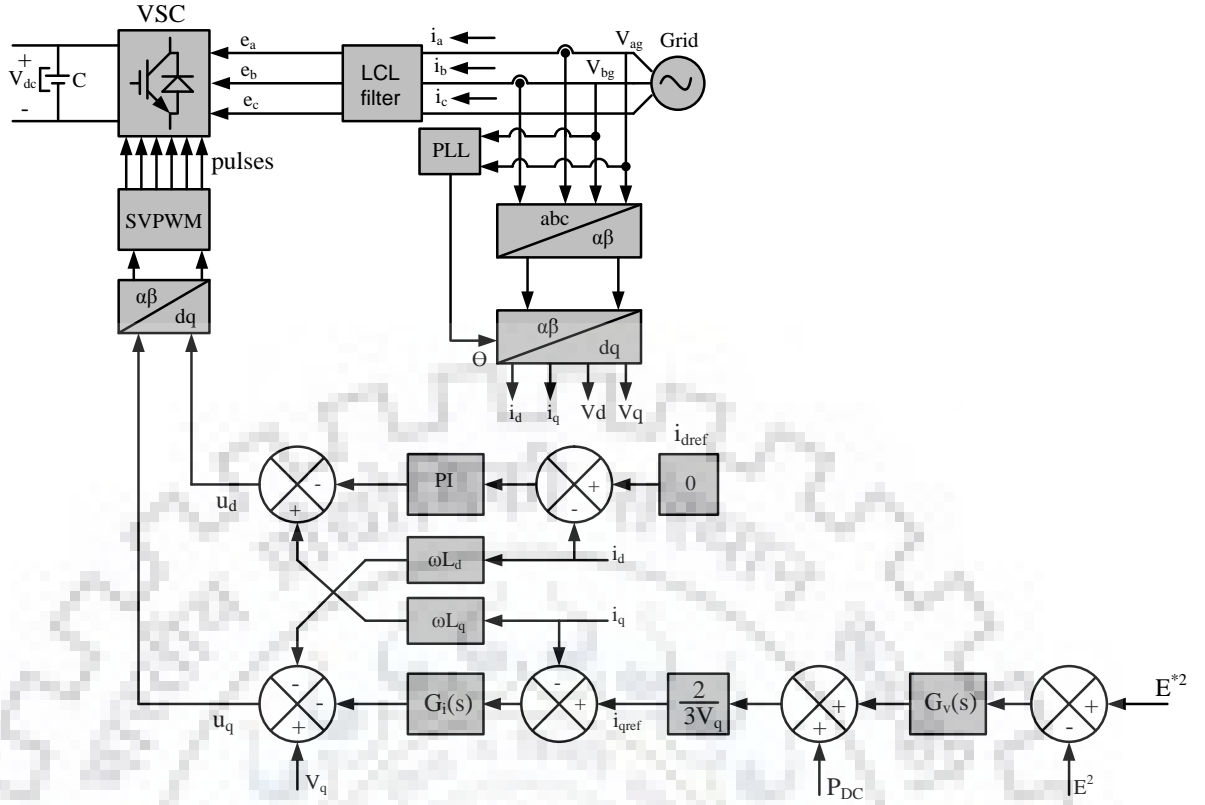


Fig. 2. 8: VSC PQ Control System

Consider the VSC connected to the AC grid shown in Fig.2.1. In the figure the  $v_{sabc}$  represent the grid voltages,  $i_{sabc}$  is grid-side line current,  $L/R$  are line inductance and resistance respectively,  $v_{tabc}$  is the converter side voltage and  $i_{c-abc}$  is the AC line current from the converter side [107].

Then the converter model in the dq synchronous frame can be expressed by:

$$\begin{aligned}
 v_{td} &= L_2 \frac{di_{cd}}{dt} + R_2 i_{cd} + [v_{cd} + (i_{sd} - i_{cd})R_f] + \omega L_2 i_{cq} \\
 v_{tq} &= L_2 \frac{di_{cq}}{dt} + R_2 i_{cq} + [v_{cq} + (i_{sq} - i_{cq})R_f] - \omega L_2 i_{cd} \\
 i_{sd} &= C_f \frac{dv_{cd}}{dt} + i_{cd} + \omega C_f v_{cq} \\
 i_{sq} &= C_f \frac{dv_{cq}}{dt} + i_{cq} - \omega C_f v_{cd} \\
 v_{cd} + (i_{sd} - i_{cd})R_f &= L_1 \frac{di_{sd}}{dt} + R_1 i_{sd} + \omega L_1 i_{sq} \\
 v_{cq} + (i_{sq} - i_{cq})R_f &= L_1 \frac{di_{cq}}{dt} + R_1 i_{cq} + v_{sq} - \omega L_1 i_{qd}
 \end{aligned} \tag{2.44}$$

Where  $v_{td}$  and  $v_{tq}$  the d- and q-axis components of converter side voltage;  $u_q$  is the q-axis component grid voltage;  $\omega$  is the fundamental grid frequency;  $L_1$  and  $L_2$  filter inductances from

grid and converter side, respectively;  $R_1$  and  $R_2$  are the cable resistances and  $C_f$  and  $R_f$  represent the filter capacitor and damping resistance, respectively.

The conventional PI controller based vector control employed in an inner current loop for tracking the reference current. If the grid side current is used as feedback variables for the inner-current control, the control equation formulated as:

$$\begin{aligned}
 v_{tdref} &= \omega(L_1 + L_2)i_q + (i_{dref} - i_d)k_{pi} + k_{ii}u_{dr} \\
 v_{tqref} &= v_{sq} - \omega(L_1 + L_2)i_d + (i_{qref} - i_q)k_{pi} + k_{ii}u_{qr} \\
 u_{dr} &= \frac{i_{dref} - i_d}{s} \\
 u_{qr} &= \frac{i_{qref} - i_q}{s}
 \end{aligned} \tag{2.45}$$

Where  $k_{pi}$  and  $k_{ii}$  are the proportional and integral gain of the current controller.  $v_{tdref}$  and  $v_{tqref}$  represent the reference modulation voltages.

The LCL filter used to dampen the high harmonics due to the switching frequency of the converter. For this reason, the current control bandwidth always designed to be smaller than the resonance frequency of the LCL frequency [107], [108], and the lower order harmonics attenuated with the current control loop. Since the DC-link voltage control design is mainly based on the low-frequency range, the filter capacitor has no effect on it. Accordingly, the dynamics of the converter side voltage in q – d axis reference frame can be described by:

$$v_{td} = L \left( \frac{di_d}{dt} \right) + \omega L i_q + R i_d \tag{2.46a}$$

$$v_{tq} = R i_q + L \left( \frac{di_q}{dt} \right) - \omega L i_d + v_{sq} \tag{2.46b}$$

According to (2.45) and (2.46), the closed-loop transfer function  $G_c(s)$  for the current control results from the following equation:

$$G_c(s) = \frac{\frac{k_{pi}s + k_{ii}}{L}s + \frac{k_{ii}}{L}}{s^2 + \left( \frac{R}{L} + \frac{k_{pi}}{L} \right)s + \frac{k_{ii}}{L}} \tag{2.47}$$

The modeled grid-connected VSC simulated using the parameters described in Table 2.1 in MATLAB/SIMULINK, and the AC-side parameter results depicted in Fig. 2.9.

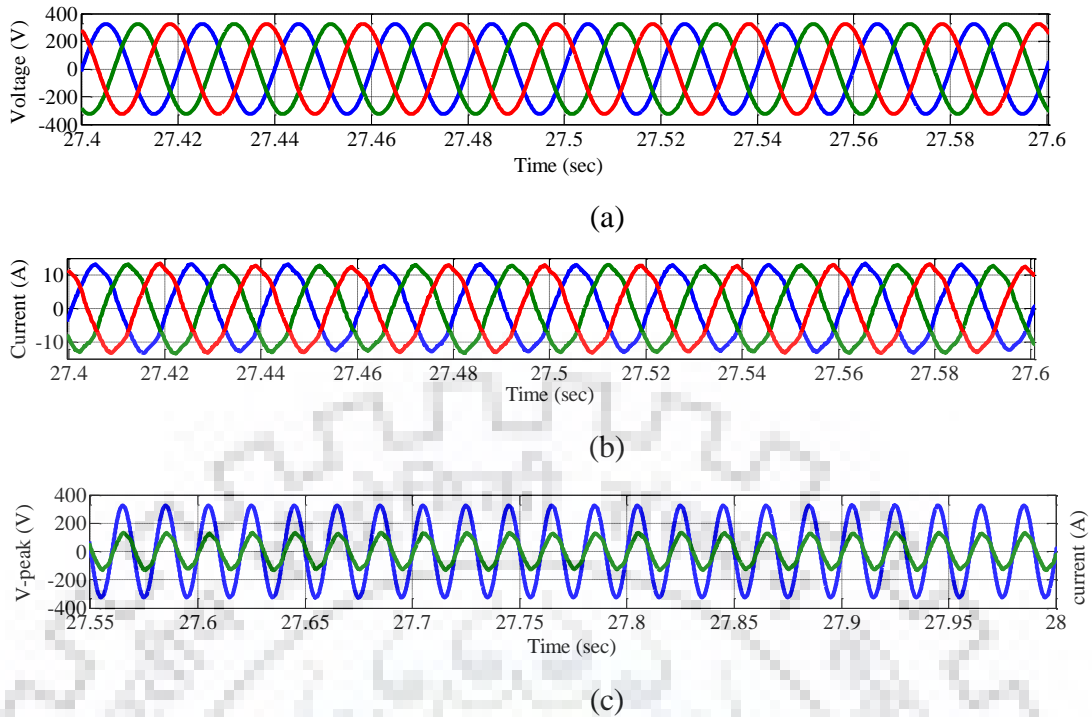


Fig. 2. 9: Grid Input Parameters, (a) 3-phase grid-side voltage, (b) 3-phase AC line current, (c) phase to neutral voltage and line current (10 times increased)

Fig. 2.9 shows grid voltage and current are in phase, and hence, the unity power control achieved. That indicates the grid phase angle and frequency controlled at the desired value. The high order harmonic frequencies that are created by a non-linear switching operation of VSC attenuated by employing an LCL filter on the input side of the converter. The inner current loop control regulates the low order harmonics, and as a result, a sinusoidal input current with THD less than 5% achieved, as shown in Fig. 2.10. The inner current control loop realizes real power control.

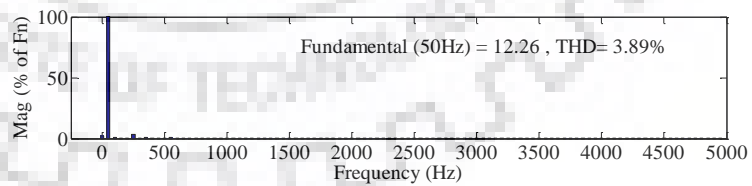


Fig. 2. 10: Current THD (%)

Table 2. 1: G-VSC Parameter

S.No	Description	Value	Units
1	Rated Capacity	5	kW
2	Grid nominal frequency	50	Hz
3	line voltage	400	V
4	Switching frequency	5	kHz
5	Filter inductances L1, L2	1.8, 2.75	mH
6	DC-Link voltage	650	V
7	Filter capacitance	1	$\mu$ F
8	Damping resistance	4.24	$\Omega$

#### d) Design of DC-Link Capacitor

The active rectifier, as shown in Fig. 2.1 has an intermediate circuit capacitor. This capacitor makes it easier to control the DC link voltage. Also, the intermediate circuit capacitor offers an energy store in the middle and also serves to decouple the three-phase VSC from the load subsystem. The difference in instantaneous active power stored in the DC-link capacitor, and this causes the DC voltage to fluctuate [109]. Thus, the DC-link capacitor value is determined based on the maximum tolerable limit of DC voltage change,  $\Delta V_{dc}$ .

This DC link capacitor designed for the currently active power flow to the DC network. The instantaneous active power that flows into the direct current system described using the synchronously rotating frame, which is based on the level of the mains voltage and is given by [97]:

$$P = V_d i_d + V_q i_q = V_q i_q, \text{ with } V_d = 0 \quad (2.48)$$

$i_q$  and  $V_q$  are the q-axis component of grid current and voltage magnitude respectively and they can be expressed by:

$$V_q = E_n$$

$$i_q = \text{Im}(\sqrt{3}I_n \sin(-2\omega_1 t)) \quad (2.49)$$



Where  $E_n$  represent the nominal value of peak amplitude-phase voltage and  $\omega_1$  denotes the nominal grid angular frequency. Neglecting the grid-connected VSC losses, the corresponding instantaneous active power flowing into the DC-link capacitor calculated as:

$$P = i_{cdc} V_{dc} = P_{ac} \quad (2.50)$$

Substituting equation (2.48) into (2.50) and simplifying the equation, the average DC capacitor current can be estimated:

$$i_{cdc} = \frac{e_q}{V_{dc}} i_q \quad (2.51)$$

The change in DC voltage can also be achieved by:

$$\frac{d}{dt} V_{dc} = \frac{1}{C_{dc}} \frac{e_q}{V_{dc}} i_q \quad (2.52)$$

The average DC voltage derived by linearizing the (2.52), and it is given by:

$$\frac{d}{dt} \Delta V_{dc} = \frac{1}{C_{dc}} \frac{e_q}{\bar{V}_{dc}} i_q \quad (2.53)$$

Finally, the DC-link capacitor is derived by substituting (2.49) into (2.53) and simplifying the expression; the DC capacitor defined as:

$$C_{dc} = \frac{P_n}{\bar{V}_{dc} \Delta V_{dc} 2\omega_1} \quad (2.54)$$

Where  $P_n$  represents the converter nominal power rating. Accordingly, substituting the converter parameter values listed in Table 2.1 in (2.54), DC capacitor calculated as;  $C_{dc} = 300\mu\text{F}$ .

#### e) The DC Voltage Control

The DC voltage controller regulates the DC link voltage and sets the reference input for the q-axis current controller. The control block diagram proposed in this study shown in Fig. 2.8. The measured DC voltage and feed-forward (capacitor power) used to improve system performance. The  $E^2$  is proportional to the energy stored in the capacitor. The controller output is the active power supplied to the capacitor  $P_C^*$ . Accordingly, the desired real power for the converter evaluated at  $P_{ref} = P_C + P_{DC}$ , where  $P_{DC}$  represents the power detected in front of the intermediate circuit capacitor [110]. In this study, the mains supply voltage used as the nominal bus voltage of the DC micro-network. The control method implemented with a PI controller.

Suppose  $W = E^2$  is the control variable used in the design of the DC voltage control. Then the intermediate circuit capacitor power  $P_C$  in the frequency domain can be described as

$$P_C(s) = \frac{1}{2} s C W(s) \quad (2.55)$$

The control system represented with a transfer function  $G_{vDC}$

$$G_{vDC}(s) = K_{pv} + \frac{K_{iv}}{s} \quad (2.56)$$

The closed-loop control system transfer function could be formulated by

$$\frac{W(s)}{W_s^*} = \frac{sK_{pv} + K_{iv}}{\frac{1}{2}s^2C + sK_{pv} + K_{iv}} \quad (2.57)$$

It can also be expressed in the standard form as:

$$\frac{W(s)}{W_s^*} = \frac{2s\zeta_E\omega_E + \omega_E^2}{s^2 + 2s\zeta_E\omega_E + \omega_E^2} \quad (2.58)$$

The controller parameters can be found by:

$$K_{pv} = C\zeta_E\omega_E, \quad K_{iv} = \frac{C\omega_E^2}{2} \quad (2.59)$$

Where  $\zeta_E$  is the value of damping ratio desired for the voltage loop, and  $\omega_E$  signifies the desired gain crossover frequency of the DC voltage control loop. It should note that the DC voltage loop must be much slower than the internal current regulator to ensure stable system behavior [107], [110]. The rectified DC voltage and power simulation result, as shown in Fig. 2.11.

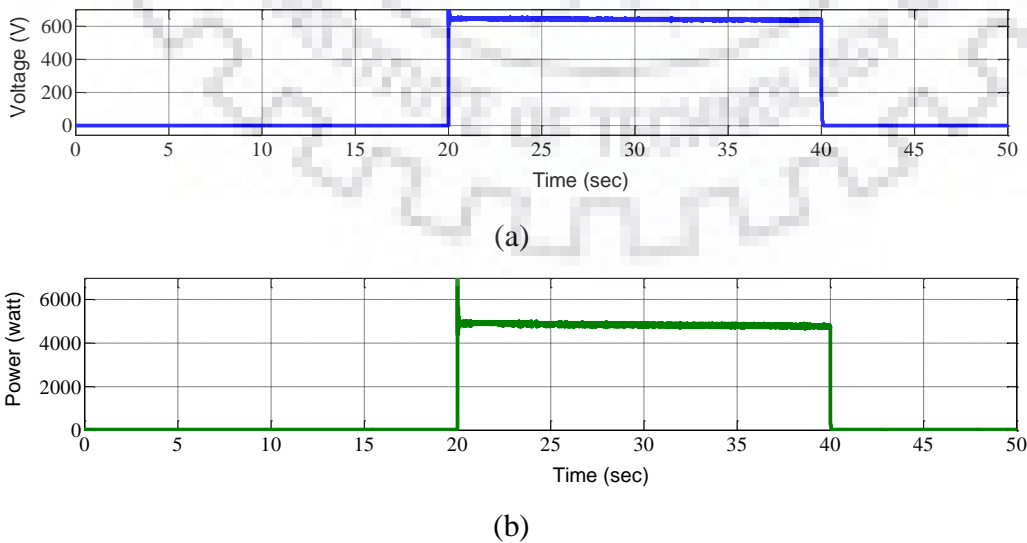


Fig. 2. 11: Grid Rectified Output Parameters. (a) DC-link Voltage (V) (b) Power (watt)

The voltage source rectifier voltage and power output simulation results, as shown in Fig. 2.11. As mentioned above, this voltage considered as a nominal DC bus voltage for the proposed DC $\mu$ G. It maintained at rated values of 650 V and 5 kW for the duration  $t = 20$  to  $t = 40$ s, voltage, and power, respectively. In this study, the grid-VSC and BESS employed for smoothing the DC bus power balance at different times. Thus, during  $t = 0$  to  $t = 20$ s and  $t = 40$  to  $t = 50$ s, the grid-VSC is in disconnected mode, and the system is operating in islanded mode. During this period, the BESS regulating the DC bus voltage by charging and discharging. The detailed result described in chapter three in section 3.8.

## **2.2. The Distribution Generation (DG) System**

Distributed energy resources developed as an alternative source of generating clean energy supply and revolutionized the conventional power generation approach. Nowadays, advancement in smart microgrid has made the DGs operate in reliable and efficiently enabling maximize operation of the system with appropriate decentralized control scheme with the intermittent generation output of solar and wind power sources [111].

Small-scale power generation developed from DERs such as solar, wind, and ESS can be utilized in islanded or with grid-connected mode. Most of these energy sources generate DC or variable AC frequency/voltage outputs [94], [112]. The DERs such as wind, solar power generation systems as well as ESSes control and operations are described in the following sections.

### **2.2.1. The Wind Power System**

Wind energy is a type of renewable energy source that found abundantly in nature, and it is one of the clean energy sources. The wind power systems mainly classified as variable speed, semi-variable speed, and fixed-speed wind energy system [113]. The variable-speed wind turbines have more advantages over the fixed-speed wind energy system due to it allows maximum power point capturing, improved efficiency, and power quality. Usually, the variable WECS consists of two main electrical components, such as generator and power converters. The main types of generators used in WECS are squirrel-cage induction generator (SCIG), wound rotor induction generator (WRIG), doubly-fed induction generator (DFIG), permanent magnet synchronous generator (PMSG) and wound rotor synchronous generator (WRSG) [113], [114].

In a variable speed WECS, the most commonly used electrical generators are a doubly-fed induction generator (DFIG) and synchronous generator (SG) [113]. In this study, the permanent

magnet synchronous generator (PMSG) used due to its self-excitation capability, higher efficiency, and simple structure. In low-speed, PMSG gearbox is not required to match the turbine and rotor speed [114]. As a result, issues such as increased cost, regular maintenance, power losses, weight, and noise generation do not exist [113]. The AC/DC converter is employed to convert the generator AC voltage to constant DC voltage [115].

Table 2. 2: Wind Turbine PMSG Parameters

S.No	Parameters description	Value
1	Wind speed	12 m/sec
2	Nominal speed	300rpm
3	Nominal torque	270 Nm
4	Generator nominal electrical power	7400 watt
5	Nominal line current	15A
6	Line voltage at no load (L-L RMS)	326 V
7	No of pole pairs	6
8	Nominal frequency	30Hz
9	Stator resistance	1.5Ω
10	d- and q-axis inductances	12.5mH

Wind power generation varies continuously with the changing wind speed throughout the day. Accordingly, the wind turbine has to deliver maximum power with the rotor speed varying according to the change in wind speed to achieve the optimum power coefficient  $C_p$  and consequently, extract maximum power from the wind turbine. As the turbine speed increases, generator output power increases (see Fig. 2.12), and at the optimum value of the rotor speed, the output power of the variable speed wind power becomes maximum [113]. The proposed wind turbine and generator parameters, as shown in Table 2.

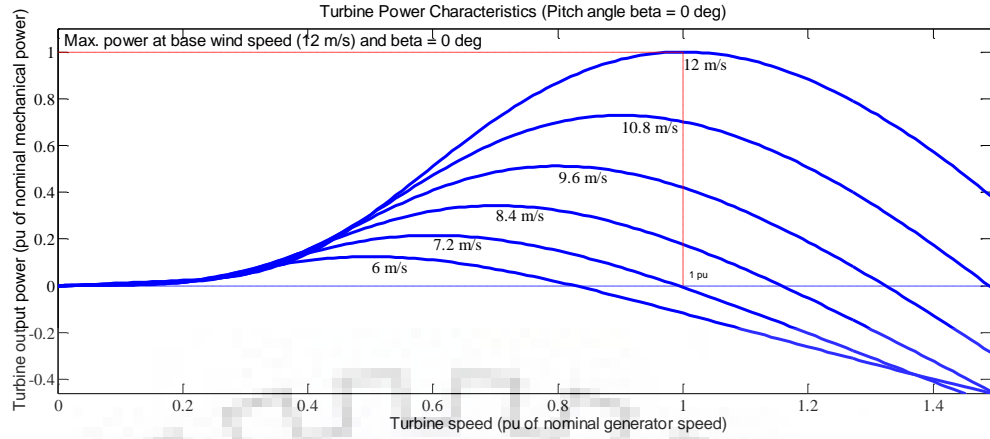


Fig. 2. 12: Turbine speed vs Wind Power System

### a) Modeling of Wind Turbine System

The power output by the wind turbine is a function of its radius, its wind speed, its pitch angle ( $\beta$ ), and the shape of the turbine. The wind power absorbed by the rotor blade and converted into mechanical force can also be calculated [113]–[115]:

$$P_m = 0.5\rho A v_w^3 C_p \quad (2.60)$$

$$T_w = 0.5 C_p(\lambda, \beta) \rho \pi R^3 A v_w^2 / \lambda \quad (2.61)$$

Where  $V_w$  is the wind speed,  $\rho$  is the air density,  $R$  is the radius of the wind turbine,  $C_p$  is the wind turbine power coefficient,  $\lambda$  is the tip speed ratio. The power coefficient  $C_p$  is dependent on the turbine pitch angle  $\beta$  and the tip speed ratio ( $\lambda$ ). The ratio between the generator speed multiplied blade radius ( $\omega_m R$ ) and speed of the wind ( $V_w$ ) referred to as TSR or  $\lambda$ . This ratio, known as the tip-speed ratio, is defined as

$$\lambda = \frac{\omega_m R}{V_w} \quad (2.62)$$

Where  $\omega_m$  is the angular rotor speed,  $\beta$  is the pitch angle. The power coefficient can be calculated by the following equation [114]:

$$C_p = 0.5 \left( \frac{116}{\lambda_i} - 0.4\beta - 5 \right) \exp\left(\frac{21}{\lambda_i}\right) \quad (2.63)$$

where

$$\lambda_i = 1 / \left( \frac{1}{\lambda + 0.08\beta} - \frac{0.035}{\beta^3 + 1} \right) \quad (2.64)$$

### a) The WECS using PSMG and Its Operation with Power Converter

Power electronic converters widely employed in WECS. With the development of these power converters, different converter topologies such as AC voltage controllers, DC/DC boost

converters, VSCs, and PWM current source converters introduced for WECS [116]. The wind subsystem proposed in this study uses PMSG to generate a variable three-phase AC supply. The variable produced voltage is supplied to the three-phase uncontrolled rectifier to convert it to DC voltage and fed to the boost converter [116]. The boost DC/DC converter performs two functions. Namely; 1) track maximum power from the wind turbine generator and boost the generated voltage to the level desired by DC bus, 2) it facilitates capturing of maximum power from the wind turbine generator with changing wind speed.

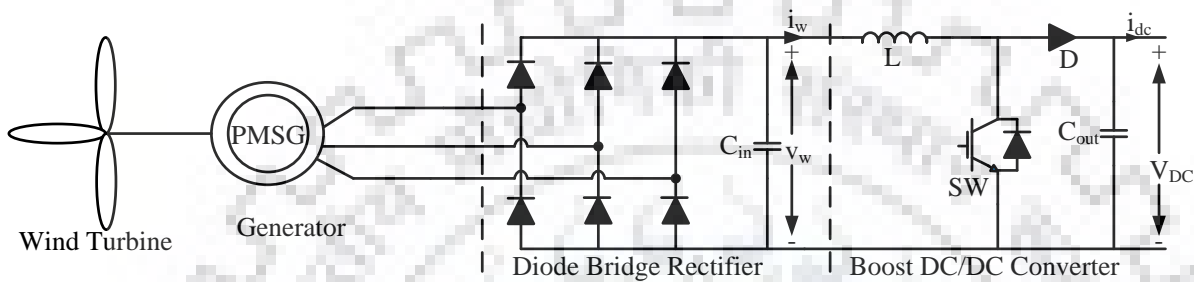


Fig. 2. 13: Schematic Diagram of WECS Proposed in this Work

Fig. 2.13 shows a typical block diagram of WECS, which is connected to the direct current network via a diode bridge rectifier and DC/DC step-up converter proposed in this work. Two variables are carefully controlled, namely: the rectified DC voltage and the active generator power. The rectified DC voltage (the output of the diode rectifier) changes when the speed of the generator changes. Therefore, the DC link voltage is controlled to be within a specified range of acceptable values by controlling the primary voltage of the boost DC/DC converter. Due to the gain of the converter, the intermediate circuit voltage is usually higher than the output voltage of the rectifier. The active power of the generator is regulated by setting the duty cycle  $D$  of the step-up converter via the control system.

## b) The Boost DC/DC Converter Modelling and Control for Wind Subsystems

### 1) Modeling of Unidirectional Boost Converter

The unidirectional boost converter is used to interface the wind and solar power source to the DC grid. The converter circuit topology, as shown in Fig. 2.14. The state-space averaging is applied in converter modeling. The boost converter equivalent circuit with the switch turned on and off separately [80], [117] is depicted in Fig. 2.14 (b) and (c), respectively.

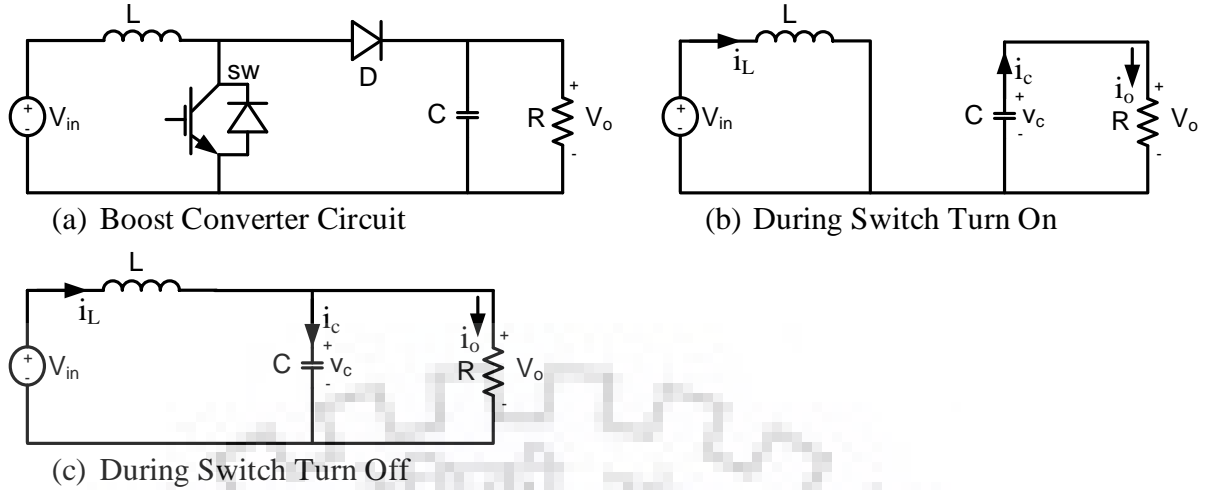


Fig. 2. 14: Boost Converter Operating Topologies

During the switch is ON (Fig. 2.14b), then the state space equation can be derived as:

$$L \frac{di_L}{dt} = v_{in} \quad (2.65a)$$

$$C \frac{dv_c}{dt} = \frac{v_c}{R} \quad (2.65b)$$

Where  $v_o$ ,  $v_{in}$ ,  $i_L$  the output voltage of the converter, the input voltage, and the current through the inductance (input current), respectively. Similarly,  $L$  and  $C$  are the converter inductor and the capacitor, respectively.

During the switch is OFF (Fig. 2.14c), the equation described as:

$$L \frac{di_L}{dt} = v_{in} - v_o \quad (2.66a)$$

$$C \frac{dv_c}{dt} = i_L - \frac{v_c}{R} \quad (2.66b)$$

The averaged state-space equation is expressed as:

$$L \frac{d\Delta i_L(t)}{dt} = \Delta v_{in}(t) - (1 - D)\Delta v_c(t) + V_c \Delta d(t) \quad (2.67a)$$

$$C \frac{d\Delta v_c(t)}{dt} = (1 - D)\Delta i_L(t) - I_L \Delta d(t) + V_c \Delta d(t) \quad (2.67b)$$

Transforming (2.67) into the frequency domain and simplifying the equation, the converter control to output, control to input current and input current to output transfer functions are obtained:

$$G_{vd}(s) = \frac{\Delta v_o(s)}{\Delta d(s)} = \frac{(1-D)V_o - (LI_L)s}{(LC)s^2 + \frac{L}{R}s + (1-D)^2} \quad (2.68)$$



$$G_{id}(s) = \frac{\Delta i_L(s)}{\Delta d(s)} = \frac{sCV_o + 2(1-D)I_L}{(LC)s^2 + \frac{L}{R}s + (1-D)^2} \quad (2.69)$$

$$G_{iv}(s) = \frac{\Delta v_o(s)}{\Delta i_L(s)} = \frac{(1-D)V_o - (LI_L)s}{(CV_o)s + 2(1-D)I_L} \quad (2.70)$$

In the case of MPPT control mode, the converter loop gain achieved by multiplying controller and power plant transfer functions in the frequency domain, and it is given by [31]:

$$G_{ioL}(s) = G_c(s) * G_{id}(s) \quad (2.71)$$

Where  $G_c(s)$  represent PI controller transfer function. Similarly, the voltage and current open-loop transfer functions can be given by:

$$G_{ioL}(s) = G_{ii}(s)G_{id}(s) \quad (2.72)$$

$$G_{voL}(s) = G_v(s)G_{cl}(s)G_{vi}(s) \quad (2.73)$$

Where  $G_{cl}(s) = \frac{G_{ii}(s)G_{id}(s)}{1+G_{ii}(s)G_{id}(s)}$

## 2) The Control Scheme of the Boost DC/DC Converter

The RES input parameters such as irradiation in PV, wind speed in WECS, load demand, and the status of BESS in the microgrid determine the operating modes of DG systems. Accordingly, the control system for DG sources, such as PV and wind turbines, can be broadly classified into two. These are constant voltage control and MPPT Control, as illustrated in Fig. 2.15.

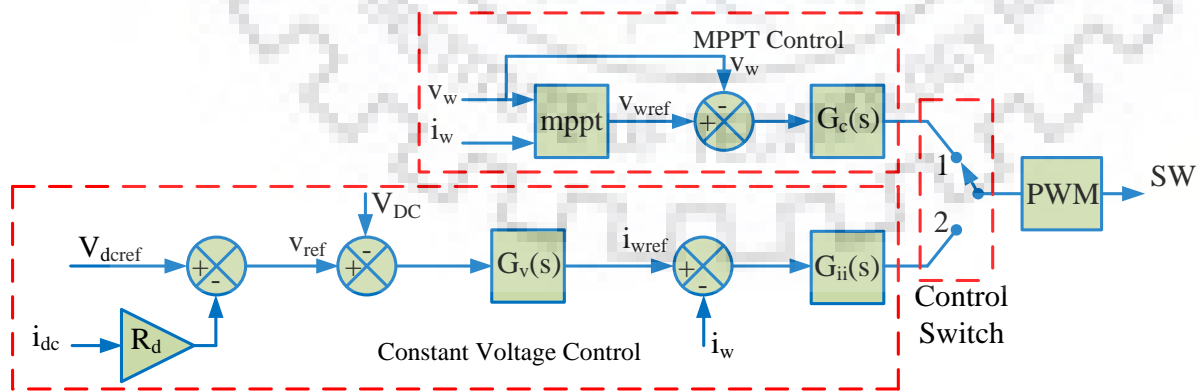


Fig. 2. 15: Wind Converter Control System

In Fig. 2.15  $V_w$  represent rectified DC voltage input for boost converter,  $i_w$  is represent boost converter input current.  $V_{dc}$  and  $i_{dc}$  boost converter output voltage and current, respectively. In



MPPT control mode the converter input voltage  $V_w$  and current  $i_w$  is sensed and provided to the MPPT module to track the MPPT reference voltage  $V_{wref}$  as similar to the rectified DC voltage, as illustrated in Fig. 2.16. This reference voltage  $V_{wref}$  is applied to the voltage controller to regulate the converter's input voltage through the closed-loop and hence, control the active power wind generator. In this work, the Perturb and Observe (P&O) MPPT scheme described in [118] is implemented for maximum power point tracking control. In the case of the MPPT control system, the wind generation unit used as a current source that injects the generated power into the DC grid.

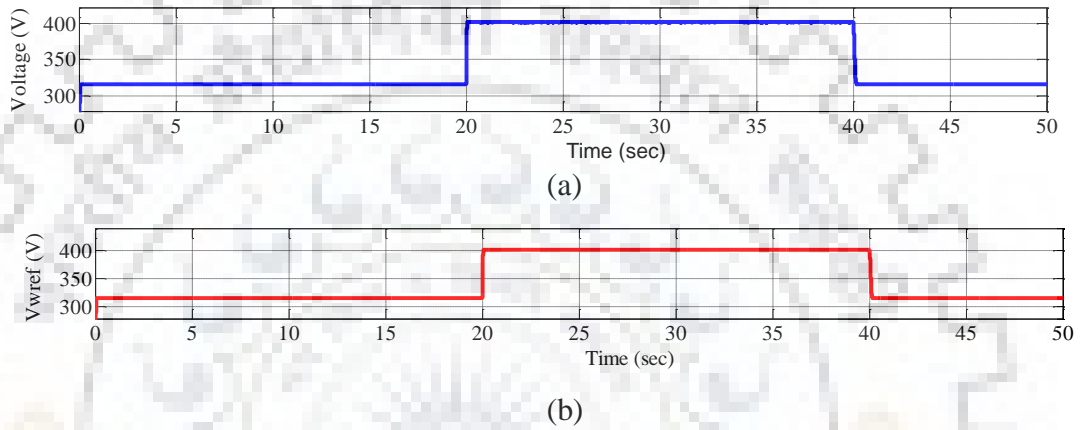


Fig. 2. 16: Input Voltage of Wind Boost DC/DC Converter, (a) Boost Converter Input Voltage ( $V_w$ ) (b) MPPT Output Reference Voltage ( $V_{wref}$ )

On the other hand, during the light load condition, the wind power generation shifts to constant voltage control (CVC). In this case, the system considered a voltage source unit. However, in the case of two or more voltage source units interconnected in parallel, a circulating current exist between the sources.

Therefore, to overcome this problem, a droop control scheme is employed to avoid the circulating current. In droop controlled voltage source units, the power-sharing technique realized by decreasing the reference voltage linearly with increases in output current [119] and the converter modeled as a voltage source in series with virtual impedance ( $R_d$ ) [63], [79]. The circulating current among the sources is reduced by designing the virtual resistances and employing it in series with the Thevenin source voltage. From Fig. 2.15, the voltage droop equation can be formulated as [120]:

$$V_{ref} = V_{dcref} - R_d i_{dc} \quad (2.74)$$

Where  $R_d$ , is the virtual output impedance  $V_{dcref}$  is the converter output voltage reference and  $i_{dc}$  is the converter output current and  $V_{ref}$  represent the reference voltage used as input for the

voltage control loop. The virtual impedance calculated by using parameters such as converter rated power and DC bus voltage [119] and given as:

$$R_d = \frac{\Delta v_{dc}(v_{dc} - \Delta v_{dc})}{P_n} \quad (2.75)$$

Where  $P_n$ , is the nominal power of the converter,  $\Delta v_{dc}$  the change in voltage on the DC bus.

### c) Boost Converter Controller Design

#### 1) Current Loop Control Design

The proposed controller block diagram illustrated in Fig. 2.17.

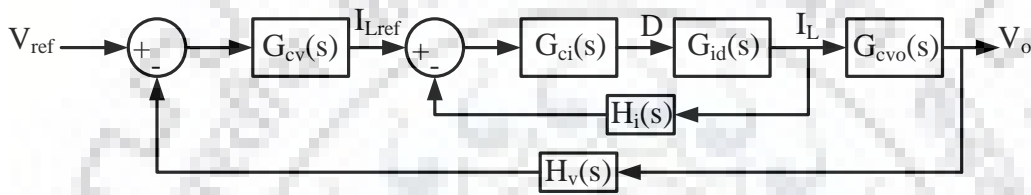


Fig. 2. 17: Wind and Solar Boost Converter Controller Block Diagram

The current reference of the step-up converter inductance ( $I_{Lref}$ ) generated from the outer voltage control loop. This current reference compared with the measured boost inductance current ( $i_L$ ) and applied to the PI controller block. The function for current transfer from the control to the inductance expressed in (2.71). In the equation,  $\Delta i_L$  and  $\Delta d$  represents the small signal interference of the step-up converter inductance and the duty cycle. The current transfer function of the PI controller formulated as follows:

$$G_{ci}(s) = k_{pi} + \frac{k_{ii}}{s} \quad (2.76)$$

Where  $k_{pi}$  and  $k_{ii}$  are the proportional and integral gain. Similarly, the loop-gain (open-loop) transfer function of the current control derived as:

$$G_{oi}(s) = G_{ci}(s) * G_{id}(s) * H_i(s) \quad (2.77)$$

Table 2. 3: Rated Wind Boost Converter Parameters

1	Input Voltage ( $V_w$ )	400V
2	Input Current ( $I_{Lw}$ )	18A
3	Duty Cycle (D)	0.3548
4	Inductance ( $L_w$ )	7.4mH
5	Capacitance (C)	140 $\mu$ F
6	Output Voltage ( $V_o$ )	680V
7	Rated Power ( $P_w$ )	7kW

The rating of the boost converter parameters used in the simulations listed in Table 2.3. The control system is designed based on the frequency responses. As a result the proportional and integral gains of the controller are designed to obtain phase margin (PM) of  $60^\circ$  and cut-off frequency of 3.14krad/sec.

The controller parameter tuning is done through the SISO tool using Matlab/Simulink software package. The controller gains calculated to be  $k_{pi} = 0.0241$  and  $k_{ii} = 68.8$ . The bode plot of the current control loop depicted in Fig.2.18.

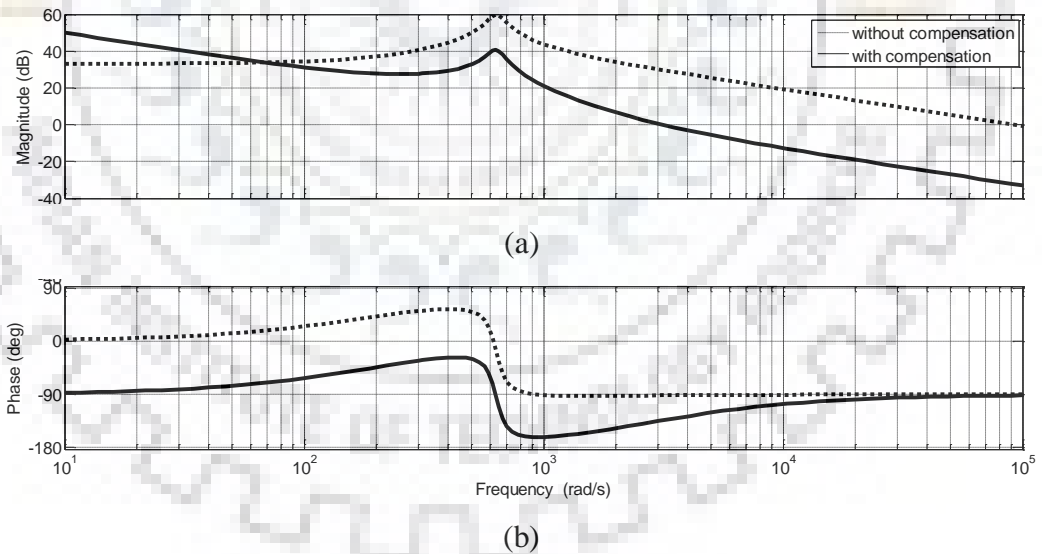


Fig. 2. 18: Wind Converter Bode Plot of Current Control Loop

## 2) Voltage Loop Control Design

The voltage control loop designed by using the inductor current to output voltage transfer function of the boost converter. The transfer function described by the equation given in (2.72). Where  $\Delta d$  and  $\Delta v_o$  represent the small-signal perturbation of the boost converter inductor

current and output voltage, respectively. The voltage compensator transfer function is described by:

$$G_{cv}(s) = k_{pv} + \frac{k_{iv}}{s} \quad (2.78)$$

Moreover, using the plant and controller transfer function, the loop-gain of the system is obtained as:

$$G_{cvo}(s) = G_{cv}(s) * G_{vi}(s) * G_{cl}(s) * H_v(s) \quad (2.79)$$

$G_{cl}(s)$  is represents:

$$G_{cl}(s) = \frac{G_{ci}(s)*G_{id}(s)}{1+G_{ci}(s)*G_{id}(s)*H_i(s)} \quad (2.80)$$

The controller parameters designed to obtain a phase margin and cut-off frequency of 60 and 1.34krad/sec, respectively, using (2.79) based on frequency response analysis. The controller gains calculated are  $k_{pv} = 0.278$  and  $k_{iv} = 33$ . Using (2.79) bode plot of the voltage control loop is simulated with Matlab/Simulink and shown in Fig. 2.19.

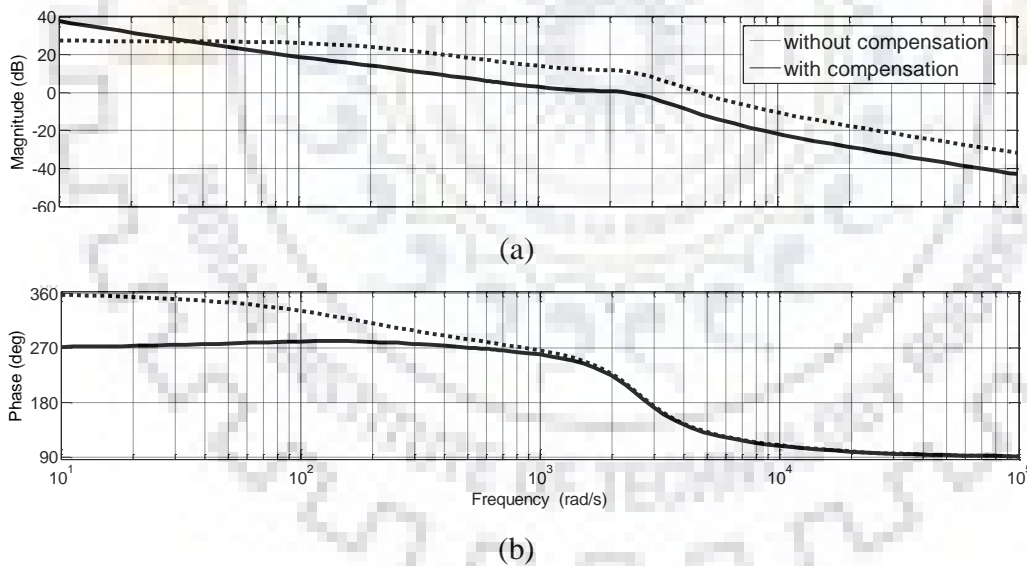


Fig. 2. 19: Wind Converter Bode Plot of Voltage Control Loop

## 2.2.2. The PV Power Generation System

### a) The PV Array Modelling

As reported in many kinds of literature [121], [122] the PV array equivalent circuit consists of a diode in parallel with a current source, series ( $R_s$ ) and parallel ( $R_p$ ) resistance, respectively, as depicted in Fig. 2.20 (a). The current source provides current in proportional to the solar

irradiation level. Fig. 2.20 (b) illustrates the voltage versus current curves of the PV array circuit. The PV array behaves as a current source for voltage lower than  $V_{mp}$  (region 1) and it acts as a voltage source for a voltage higher than  $V_{mp}$  (region 2).

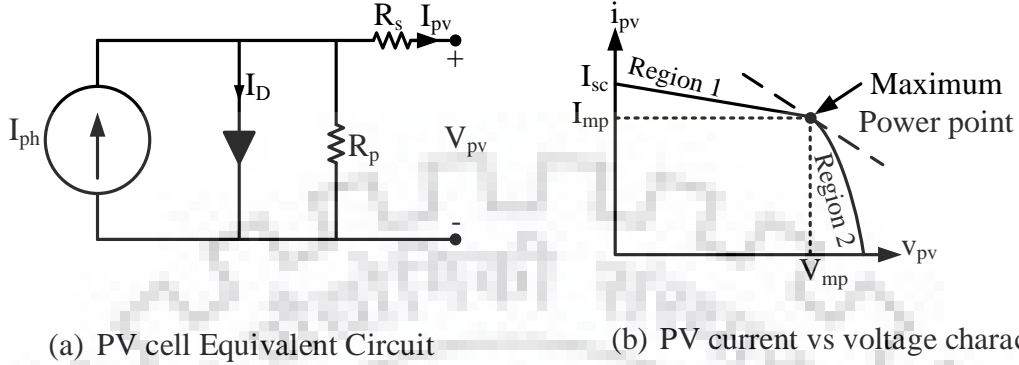


Fig. 2. 20: PV Circuit Model and  $I \times v$  Curve

The PV array mathematical modeling expressed as [123]:

$$i_{pv} = I_{PV} - I_0 \left[ \exp \left( \frac{V_{pv} + R_s i_{pv}}{V_t a} \right) - 1 \right] - \frac{V_{pv} + R_s i_{pv}}{R_p} \quad (2.81)$$

Where  $I_{PV}$  is the PV short-circuit current,  $I_0$  is diode saturation current of PV array,  $V_t = \frac{N_s k T}{q}$  represent the thermal voltage of  $N_s$  cells connected in series,  $q$  is a charge of the electron,  $T$  is the PV cell temperature,  $a$  is diode ideality factor, and  $k$  is Boltzmann constant. The PV array  $i \times v$  curve is linearized at the operating point, as indicated in Fig. 2.20 (b). The derivative of the modeled equation is given by

$$g(V, I) = -\frac{I_0}{V_t * N_s * a} \exp \left( \frac{V + I R_s}{V_t N_s} \right) - \frac{1}{R_p} \quad (2.82)$$

The tangent line obtains the linearized PV array model to the voltage vs current curve at the MPP, and it is described by

$$i_{pv} = (-gV + I) + gV_{pv} \quad (2.83)$$

The simplified circuit for the linearized model, as shown in Fig. 2.21. The equivalent PV array resistance and voltage calculated as:  $V_{eq} = V - I/g$  and  $R_{eq} = -1/g$  [32].

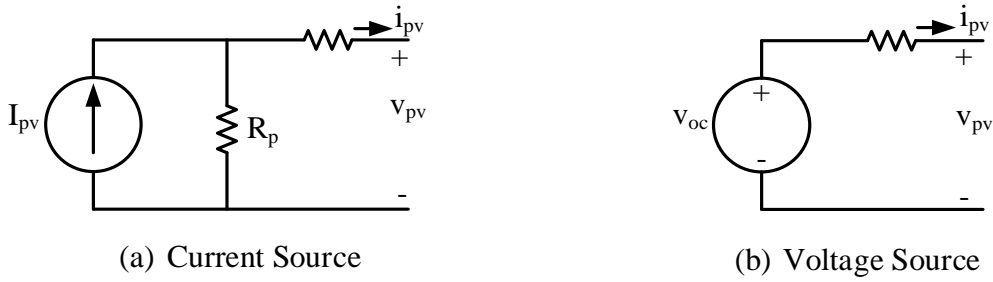


Fig. 2. 21: Linearized PV Array Equivalent Circuit

### b) The PV Interfacing Converter Control and Operation

The operation of the PV arrays depends on factors such as solar insolation, load demand, and the conditions of another energy source in the DC microgrid. Due to the changing character of the irradiation, the power generation in the PV system is also changing. Accordingly, similar to the wind power system, two control modes, namely MPPT and voltage control, are employed, as depicted in Fig. 2.22 [52]. The constant voltage control (CVC) used during sufficient power generation from the PV or wind power. Two or more RESs are connected in parallel and operating as a voltage source unit; there will be a problem of the circulating current. Thus, droop control is included in the outer voltage loop, as illustrated in Fig. 2.22, to reduce the circulating current. Fig. 2.22 demonstrates the two control mode schemes. In the case of MPPT control mode, the PV array voltage and current is measured and provided to the MPPT module to calculate the PV power ( $P_{pv}$ ). The MPPT module output the reference PV voltage  $V_{pvref}$  and this voltage is compared with the sensed PV array voltage. The result is provided to the PI controller to generate a pulse signal for the switching operation of the converter.

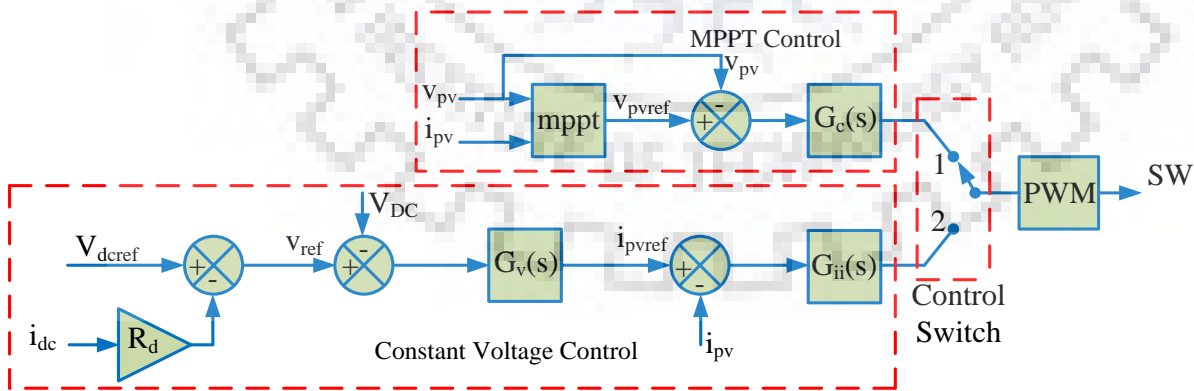


Fig. 2. 22: Control Schematics for PV Boost DC/DC Converter

In the voltage control mode, an average current control method with outer voltage control loops and inner current control loops is used to regulate the current of the PV array. The current reference  $I_{pvref}$  for the current regulator is calculated from the outer voltage loop. The boost

converter input voltage controlled to follow the reference MPPT voltage to achieve the same with the measured PV array voltage, as shown in Fig. 2.23.

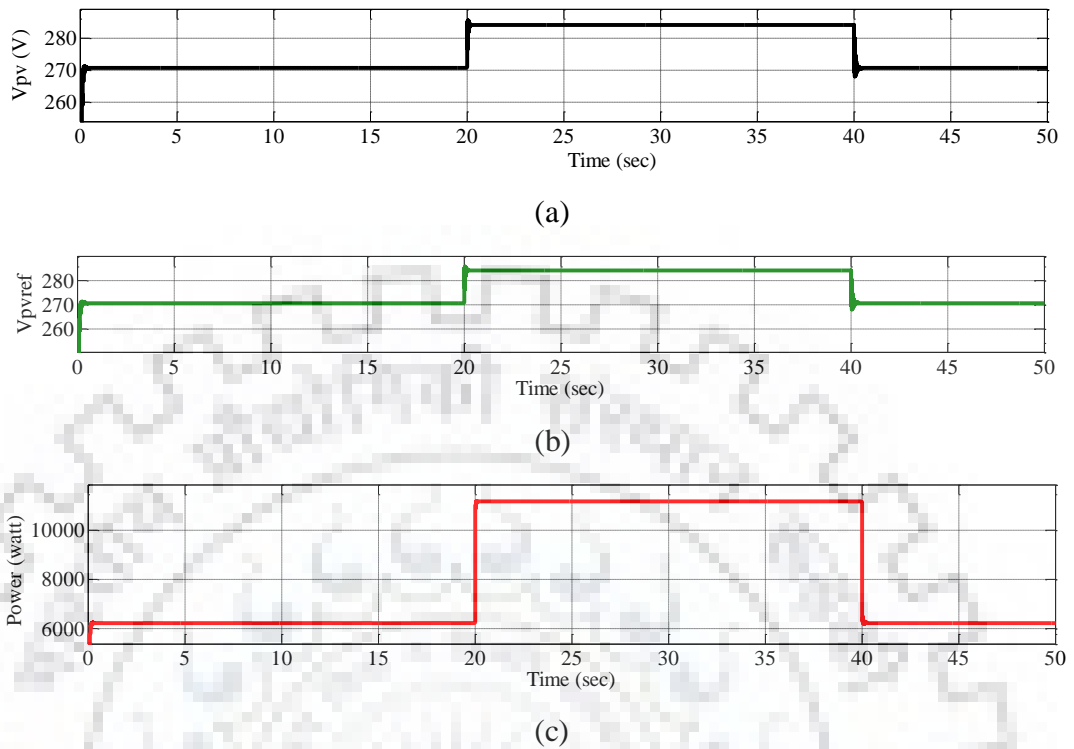


Fig. 2. 23: PV Boost Converter Input Voltage. (a) PV Array Voltage, (b) PV MPPT Output Voltage Reference

### c) The PV Boost Converter Small-Signal Modelling

The PV array dynamic model is a non-linear system. As a result, a linear model is necessary for small-signal analysis and designing a controller. The non-linear differential model of the PV array equation described in (2.82).

As shown in Fig. 2.20 (b), the slope of the PV  $i \times v$  curve in region – 2 is bigger than region – 1. The dynamic resistance is proportional to this slope, and accordingly, the system dynamics can be affected by the operating conditions. In [121], as shown that the current source curve operation is worse than the voltage source region. Consequently, the current source considered for controller design due to its most critical dynamic characteristics.

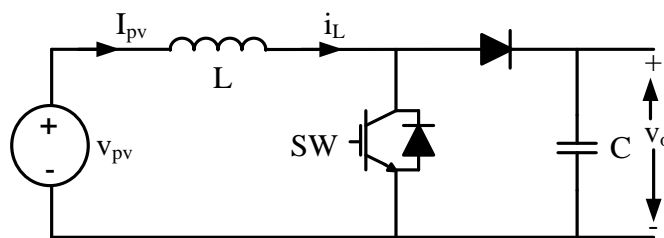


Fig. 2. 24: PV Interconnecting Converter in DC Microgrid



In Fig. 2.24, the PV interfacing converter dynamics are derived [121].

$$L \frac{d\Delta i_L(t)}{dt} = \Delta v_{pv}(t) - (1 - D)\Delta v_o(t) + V_o \Delta d(t) \quad (2.83)$$

$$C \frac{d\Delta v_o(t)}{dt} = (1 - D)\Delta i_L(t) - I_L \Delta d(t) + V_o \Delta d(t) \quad (2.84)$$

The function of the boost converter is to regulate the PV input voltage by adjusting its duty cycle to track the maximum power point and control the converter DC voltage in constant voltage control (CVC) mode. Converting (2.83), and (2.84) into the frequency domain, the control to inductor current and inductor current to output voltage transfers can be obtained and is given by (2.85) & (2.86).

$$G_{id}(s) = \frac{\Delta i_L(s)}{\Delta d(s)} = \frac{sCV_o + 2(1-D)I_L}{(LC)s^2 + \frac{L}{R}s + (1-D)^2} \quad (2.85)$$

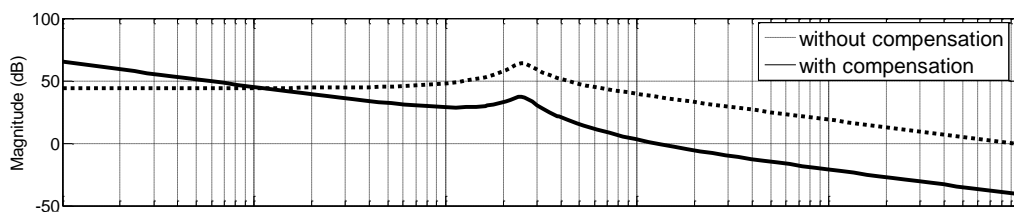
$$G_{iv}(s) = \frac{\Delta v_o(s)}{\Delta i_L(s)} = \frac{(1-D)V_o - (LI_L)s}{(CV_o)s + 2(1-D)I_L} \quad (2.86)$$

The solar boost converter's controller design method is similar to the wind converter controller design. Thus, the controller design is implemented similarly as the wind converter controller design based on the converter nominal parameters described in Table 2.4.

Table 2. 4: Rated Solar PV Boost Converter Parameters

1	PV array output voltage ( $V_{pv}$ )	300V
2	PV array current ( $I_{pv}$ )	40A
3	Duty Cycle (D)	0.5216
4	Inductance ( $L_{sol}$ )	7.8mH
5	Capacitance ( $C_{sol}$ )	440 $\mu$ F
6	Output Voltage ( $V_o$ )	665V
7	Rated Power ( $P_{sol}$ )	12kW

The calculated controller gains are  $k_{pi} = 0.0101$  and  $k_{ji} = 2$ . The frequency plot of the current control loop portrayed in Fig. 2.25.





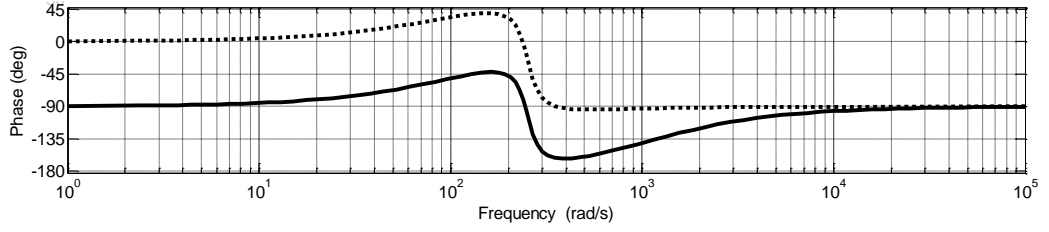


Fig. 2. 25: Solar Converter Bode Plot of Current Control Loop

### 2.3. Battery Energy Storage Modelling

Battery energy storage system modeled in different methods with various degrees of complexities. The easiest and usually used battery model includes parameters such as a controlled voltage source with an internal resistance connected in series with the source voltage [121]. The battery models characterize parameters such as self-discharge and overcharge resistance, internal resistance, and separate discharging and charging processes.

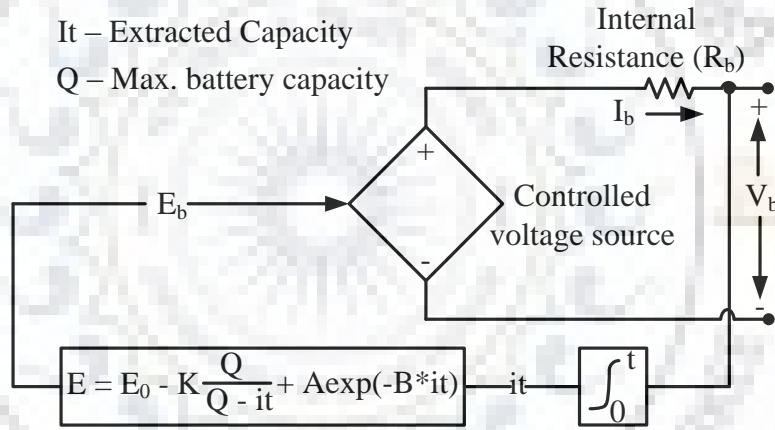


Fig. 2. 26: Simplified Battery Nonlinear Circuit Model

A generic battery model is proposed in [124] that incorporates SoC of the battery and the current that flows across the array to eliminate excessive complexity while analyzing the dynamics of the cell. Fig. 2.26 depicts the battery non-linear equivalent circuit model and the mathematically expressed as follows.

$$V_b = E_b - i_b R_b \quad (2.87)$$

$$E_b = E_0 - K \frac{Q}{Q - \int i_b dt} + A \exp(B * \int i_b dt) \quad (2.88)$$

Where  $E_b$  represent the open circuit battery voltage. The SoC of the battery is given by

$$\text{SoC}(t_i) = \frac{1}{Q(t_i)} \int \eta_c(t) I_b(t) dt \quad (2.89)$$

$$Q(t_i) = \frac{C_{\text{nom}} C_{\text{t coef}}}{1 + A_{\text{cap}} \left( \frac{|I_{\text{b}}(t)|}{I_{\text{nom}}} \right)^{B_{\text{cap}}}} (1 + \alpha_c \Delta T(t) + \beta_c \Delta T^2(t)) \quad (2.90)$$

$$C_{\text{nom}} = \frac{C_{\text{nom}}}{n} \text{ for } n \text{ hours} \quad (2.91)$$

### 2.3.1. The BESS Converter Modeling and Control

#### a) Bidirectional Buck/Boost Converter Modeling

The bidirectional battery interfacing converter depicted in Fig. 2.27 works as a buck converter in case of current flow from high to low voltage side and as a boost converter when current flows from low to high voltage side [80], [117].

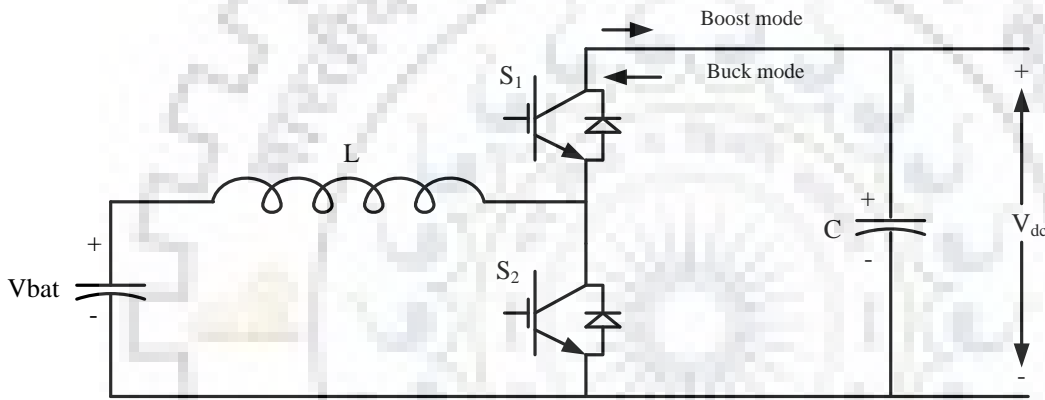


Fig. 2. 27: Bidirectional DC/DC Converter Circuit Topology

For the boost type converter, a similar average state-space model of boost converter for a wind power system described in the section above derived. Thus, to avoid redundancy, it is not explained here. The state-space model for the buck converter is calculated based on the converter switch turn on or off. Hence the circuit structure also changed accordingly. During switch closed:

$$L \frac{di_L}{dt} = V_{\text{dc}} - V_{\text{bat}} \quad (2.92a)$$

$$C \frac{dv_{\text{bat}}}{dt} = i_L - \frac{V_{\text{bat}}}{R} \quad (2.92b)$$

Where C and L represent converter capacitance and inductance respectively, while  $v_{\text{bat}}$  battery terminal voltage,  $i_L$  is current through the inductor and  $v_{\text{dc}}$  the input DC bus voltage. Similarly, in case of the switch is opened, the state-space equation derived as:

$$L \frac{di_L}{dt} = -V_{\text{bat}} \quad (2.93a)$$

$$C \frac{dv_{bat}}{dt} = i_L - \frac{V_{bat}}{R} \quad (2.93b)$$

The average state-space model is formulated

$$L \frac{d\Delta i_L}{dt} = D\Delta v_{dc} + V_{dc}\Delta d - \Delta v_{bat} \quad (2.94)$$

$$C \frac{d\Delta v_{bat}}{dt} = \Delta i_L - \frac{\Delta v_{bat}}{R} \quad (2.95)$$

Applying small perturbation in (2.94) – (2.95) and transforming to the frequency domain, the control to inductor current and inductor current to output voltage transfer function is obtained.

$$G_{id} = \frac{sCV_{dc} + 2(1-D)I_L}{(LC)s^2 + \frac{L}{R}s + (1-D)^2} \quad (2.96)$$

$$G_{iv} = \frac{\Delta v_{dc}}{\Delta i_L} = \frac{(1-D)V_{dc} - (LI_L)s}{(CV_{dc})s + 2(1-D)I_L} \quad (2.97)$$

The transfer functions described in (2.96) and (2.97) used to design the PI controller's gains [117].

### b) Battery Bidirectional Converter Control

In DC $\mu$ G, BESS is connected to the DC bus via a bidirectional buck-boost DC/DC converter to achieve better control performance [125]. Based on the DC bus voltage status at the point of standard coupling (PCC), the BESS can be controlled either in discharging or charging mode. The main control objective is to regulate the DC grid by charging the battery during excess generation output power available and by releasing the battery in case of generation deficiency.

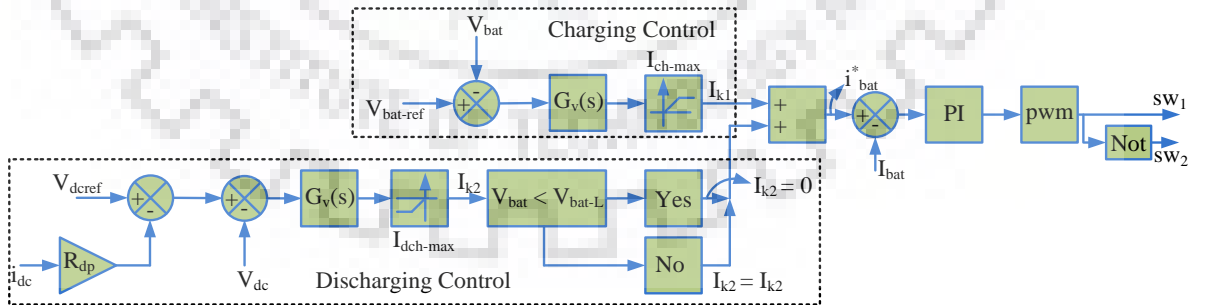


Fig. 2. 28: Battery BDC Control Block

The schematic control block diagram for the battery control proposed in this study shown in Fig. 2.28, where  $V_{bat}$  and  $V_{batref}$  represent the measured and desired battery voltages,  $V_{bat,L}$  is the battery voltage at 40% SoC,  $I_{bat}^*$  is battery reference current,  $I_{bat}$  the steady battery current. The battery charging and discharging status is determined by  $I_{bat}^*$ , where  $I_{bat}^*$  represent the

summation of charging and discharging battery output current ( $I_{k1} + I_{k2}$ ), as shown in Fig. 2.28. Moreover, when  $I_{bat}^* > 0$  the bidirectional DC/DC converter works in boost mode, and hence the battery is discharging to regulate the DC bus power balance, while  $I_{bat}^* < 0$  battery is in charging mode [125]. Thus the seamless transition among the various methods is ensured. This operation is verified using the real-time simulation via the OPAL-RT simulator and displayed in chapter three.

**c) Controller Design of Battery Converter**

The discharging (boost mode) and charging (buck mode) of the battery bidirectional interfacing converter can share a similar transfer function for the current controller design [16]. Such type of control referred to as a unified controller. In the centralized control system, the converter switches operate in a complementary manner through a single controller. The inductor current reference determines the discharging and charging status of the battery. That is when  $I_{Lref}$  is the positive battery is charging and  $I_{Lref}$  is the negative battery is discharging, as portrayed in Fig. 2.29.

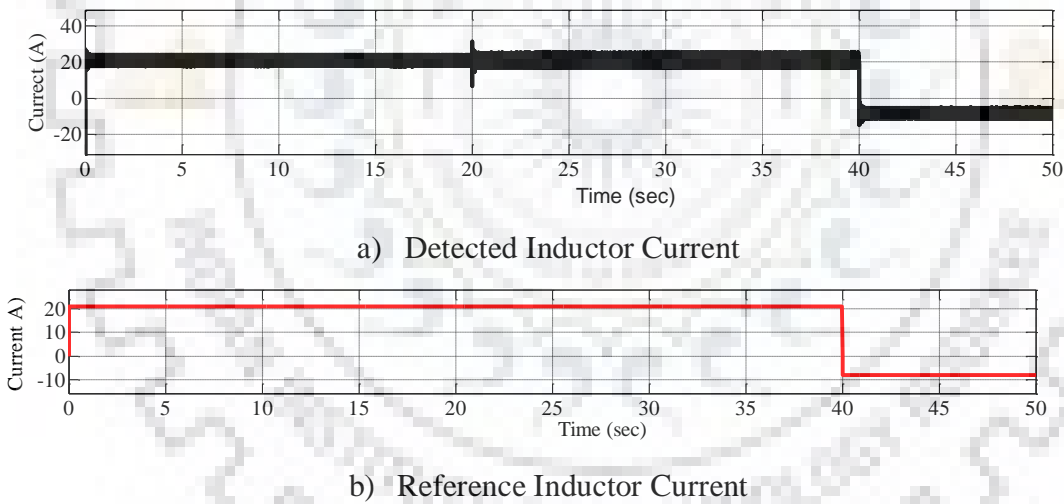


Fig. 2. 29: Battery Bidirectional Converter Inductor Current

**d) Current Control Loop Design for Battery Interfacing Converter**

The boost and buck mode of the bidirectional DC-DC converter share the same plant transfer function for internal current control, a unified control method employed.

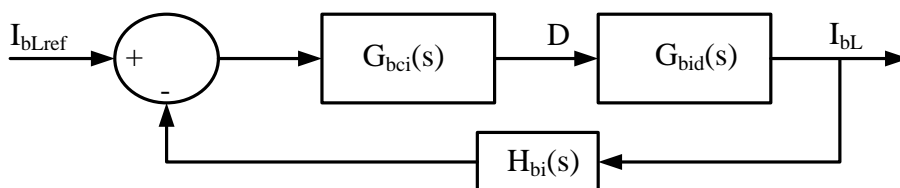


Fig. 2. 30: Battery Current Control Loop Block Diagram

Accordingly, the boost mode used for the control design. The control system block diagram, as shown in Fig. 2.30. The control to inductor current transfer function derived as:

$$G_{bid}(s) = \frac{V_o Cs + 2\frac{V_o}{R}}{L_B Cs + \frac{L_B}{R}s + (1-D)^2} \quad (2.98)$$

Where  $\Delta d$  and  $\Delta i_L$  are the change in duty cycle and inductor current, respectively. Similar to the wind and solar converter controller, the battery current controller transfer function is described by:

$$G_{bci}(s) = k_{bpi} + \frac{k_{bii}}{s} \quad (2.99)$$

The transfer function of the internal control loop in the open-loop system defined by the product of the feedback path loop and gains in the forward, and it is given by:

$$G_{boi}(s) = G_{bci}(s) * G_{bid}(s) * H_{bi}(s) \quad (2.100)$$

The battery converter parameters used in the simulation listed in Table 2.5.

Table 2. 5: Battery Bidirectional Converter Parameters

1	Battery voltage ( $V_B$ )	240V
2	Battery current ( $I_B$ )	21A
3	Duty Cycle (D)	0.62
4	Inductance ( $L_B$ )	5.1mH
5	Capacitance ( $C_B$ )	200 $\mu$ F
6	Output Voltage ( $V_o$ )	634V
7	Rated Power ( $P_B$ )	5kW

The frequency response plot of (b) using the rated of the converter parameters portrayed in Fig. 2.31. The proportional and integral constants of the controller designed to obtain the phase margin of  $60^\circ$  at a cut-off frequency of 3krad/sec. Thus controller gain constants are calculated as  $k_{bpi} = 0.101$  and  $k_{bii} = 32$ .

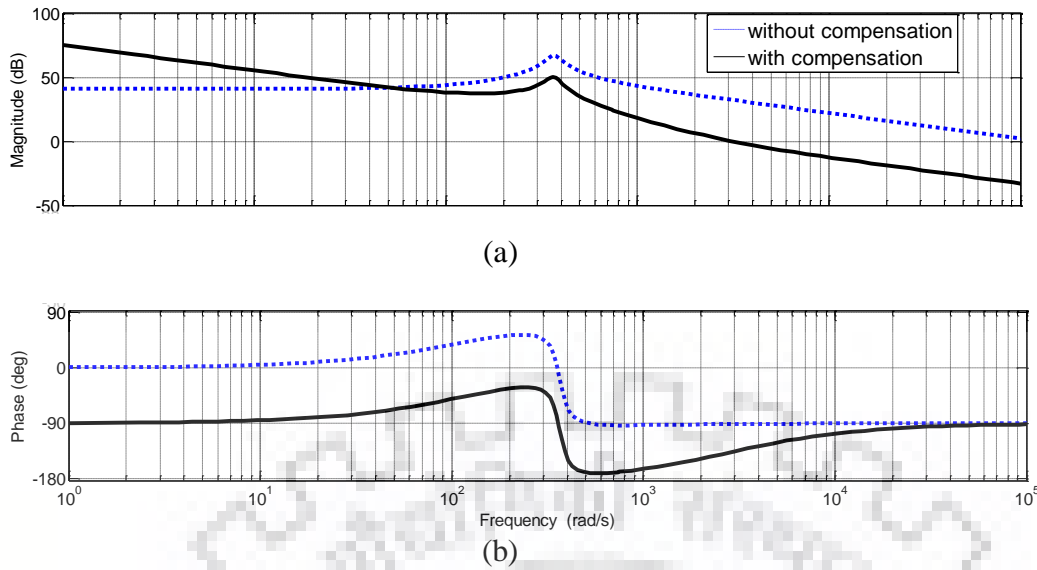


Fig. 2. 31: Battery Converter Current Control Loop Bode Plot

In a similar approach and analysis as the wind boost converter, the voltage control of the battery converter also designed, and the controller gains are achieved by  $k_{b_{pv}} = 0.0055$  and  $k_{b_{iv}} = 2.85$ . The frequency bode plot with and without the compensation depicted in Fig. 2.32.

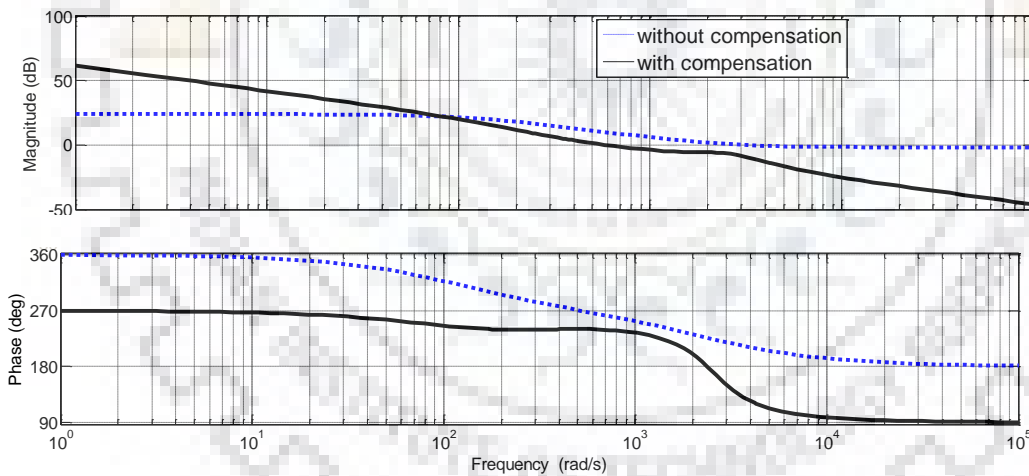


Fig. 2. 32: Battery Converter Boost Bode Plot for Voltage Control Loop

## 2.4.Summary

The modeling and control of renewable energy sources (such as wind and solar), battery energy storage, and grid-connected VSC described independently. An autonomous control scheme based on local functions such as current, voltage, and droop control is employed through the power electronic converters that connect the source units to the typical DC grid. The power electronic interface converters play a vital role in the reliable and efficient operation of the

system for integrated service. Step input source disturbances applied to the source units. The PI controllers used in all of the modules due to the control scheme presents zero steady-state error. For wind and solar power generation units, MPPT control and voltage mode droop control implemented. At rated conditions, it observed from simulation results that the desired rated value achieved. However, due to the decrease in input conditions for renewable energy sources, the generation output power also decreased. The MPPT control tracks the desired reference voltage to match with the output rectified DC voltage of the wind system and PV module voltage with the change in wind speed and solar irradiation, respectively. In the end, the proposed units modeling and design verified using MATLAB/SIMULINK simulation.







## **CHAPTER 3: DECENTRALIZED CONTROL SCHEME OF DC MICROGRID UNDER SOURCE DISTURBANCES**

The increased demands of energy and environmental problems have motivated the DGs integration in the new distribution power networks. In the past decades, DGs sources solar, wind, and ESSes have been integrated into the AC distribution to resolve the lack of energy supply. In the recent time, DC $\mu$ Gs have been employed in various areas such as telecommunications, automotive, academic institutions, data centers, and high-speed railways distribution system due to development in power electronics technologies [4], [126]. Most of the distributed energy sources are natively generates DC power, examples solar, fuel cell, and ESSes. The DC $\mu$ G system can reduce the number of power conversions stage, and this benefits the system with higher efficiency, reduced cost, and more straightforward structure [52], [75], [93], [127], [128], [129], [64]. Besides, the DC $\mu$ G topology enables the integrated parallel operation of multiple DERs. Furthermore, it provides advantages such as suitable integration of ESSes, improved power system redundancy, and flexibility. In this chapter, the decentralized control and integrated operation of multiple hybrid sources of DC $\mu$ G are described.

### **3.1. Development of DC Microgrid Architectures**

Low voltage DC (LVDC) distribution systems with a high power quality have proposed for uninterrupted power supply application in industrial use in 1993 [130], before the idea of microgrid introduced in 2002 [13]. The system demonstrated with a ring structure of DC bus, as shown in Fig. 3.1. The distribution system includes BESS to smooth the power supply system in case of AC supply outage. The anticipated objective of this structure was to obtain reliable and uninterruptable power for the critical loads.

On the other hand, the structure of LVDC distribution simplified to reduce costs for widespread applications. Because of this, the commonly used single bus DC $\mu$ G system is a suitable solution for low cost and simple structures due to ESS is directly linked with the bus, as depicted in Fig. 3.2. The single bus system is inexpensive and has a simple structure. This type of DC bus widely used in telecommunication DC power distributions. In that scheme, all the source and load subsystems linked with the universal DC bus. The stability of the bus voltage regulated with the direct connection of ESS terminals to the primary DC grid or at the PCC of the DC $\mu$ G [130], [131].

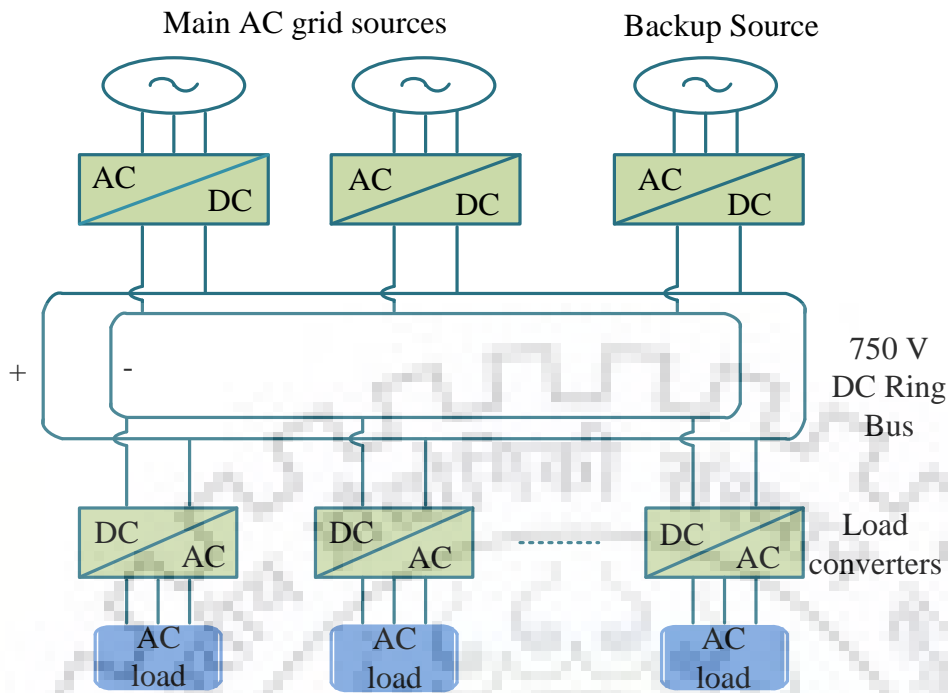


Fig. 3. 1: DC Microgrid Ring Bus Topology

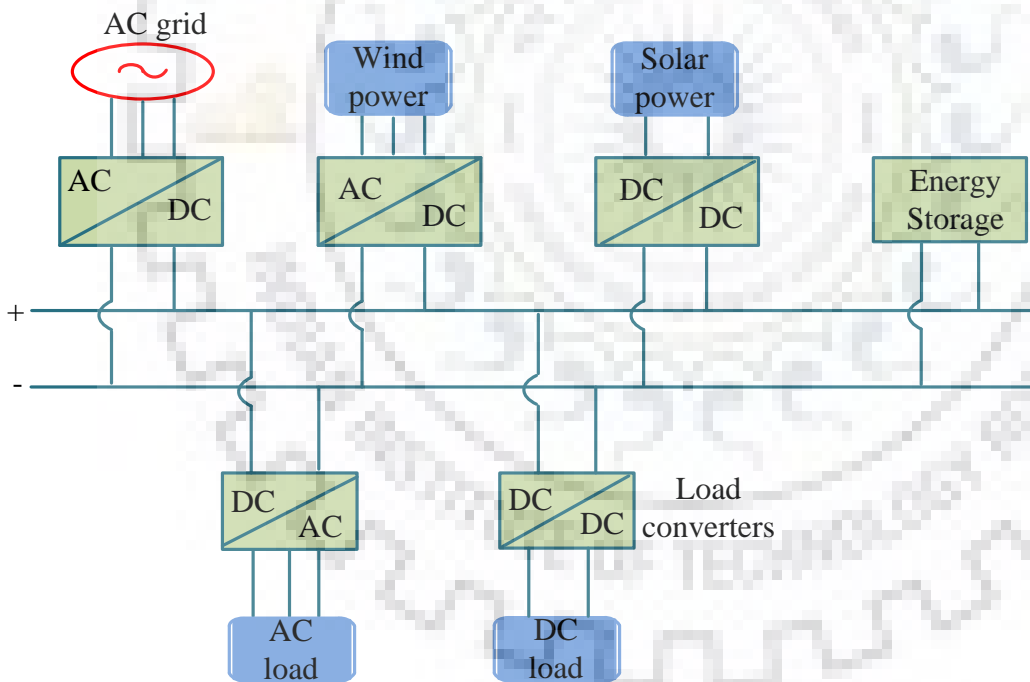


Fig. 3. 2: DC Microgrid Single Bus Topology with ESS Directly Connected

However, this topology has a limitation since the bus voltage fluctuating with the discharging and charging of BESS. Moreover, it is not comfortable to keep the power balance with the changing bus voltage. An alternative solution to the topology shown in Fig. 3.2 is proposed in [132], [133]. In this topology, the ESS interfaced with the DC bus via a bidirectional DC/DC converter, as depicted in Fig. 3.3, and it allows us to monitor operational battery status and optimize DC $\mu$ G operations. Due to the RES intermittent generation outputs caused by varying

environmental input conditions and limited power capacity of BESS, an AC grid interface incorporated that enable to improve continuous and reliable power supply in a DC $\mu$ G system.

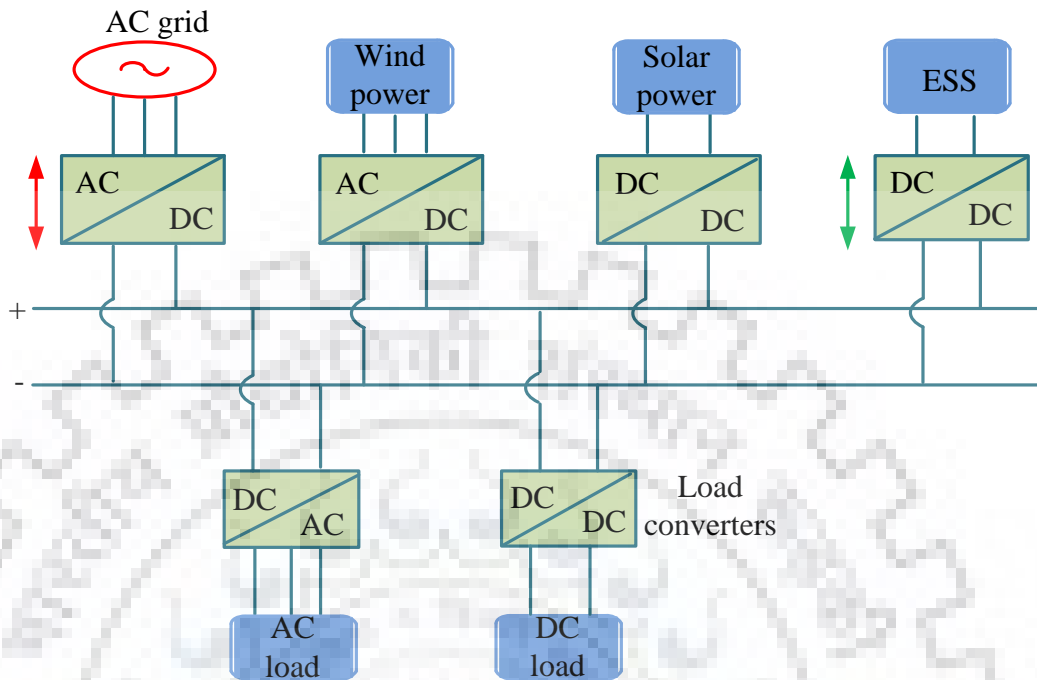


Fig. 3. 3: DC Microgrid Topology with ESS Connected via Bidirectional DC/DC Converter

Bipolar low voltage three-wire distribution DC $\mu$ G architecture with high power quality supply proposed in [2]. Fig. 3.4 shows the typical block diagram of the bipolar low voltage DC $\mu$ G architecture. The middle line used as a neutral line that connects the AC ground with the DC earth terminal. Accordingly, it provides two different active line-to-ground voltages, and hence, the system gives two different DC voltages. Loads connected with an alternative option between the three lines; thereby, the flexibility of the system is enhanced. The unbalanced loads eliminated with the method employed a voltage balancer in the DC bus between the positive and negative terminals to regulate DC voltage balance.

Besides the aforementioned DC $\mu$ G architectures, different topologies enable the system to achieve high flexibility and reliability. For example, a meshed topology that can employ in the multiterminal DC grid and DC multibus system used to form an independent power network. But structures of these topologies are complex; as a result, their system control is complicated [14]. In this study, a low voltage DC $\mu$ G topology illustrated in Fig. 3.3 chosen.

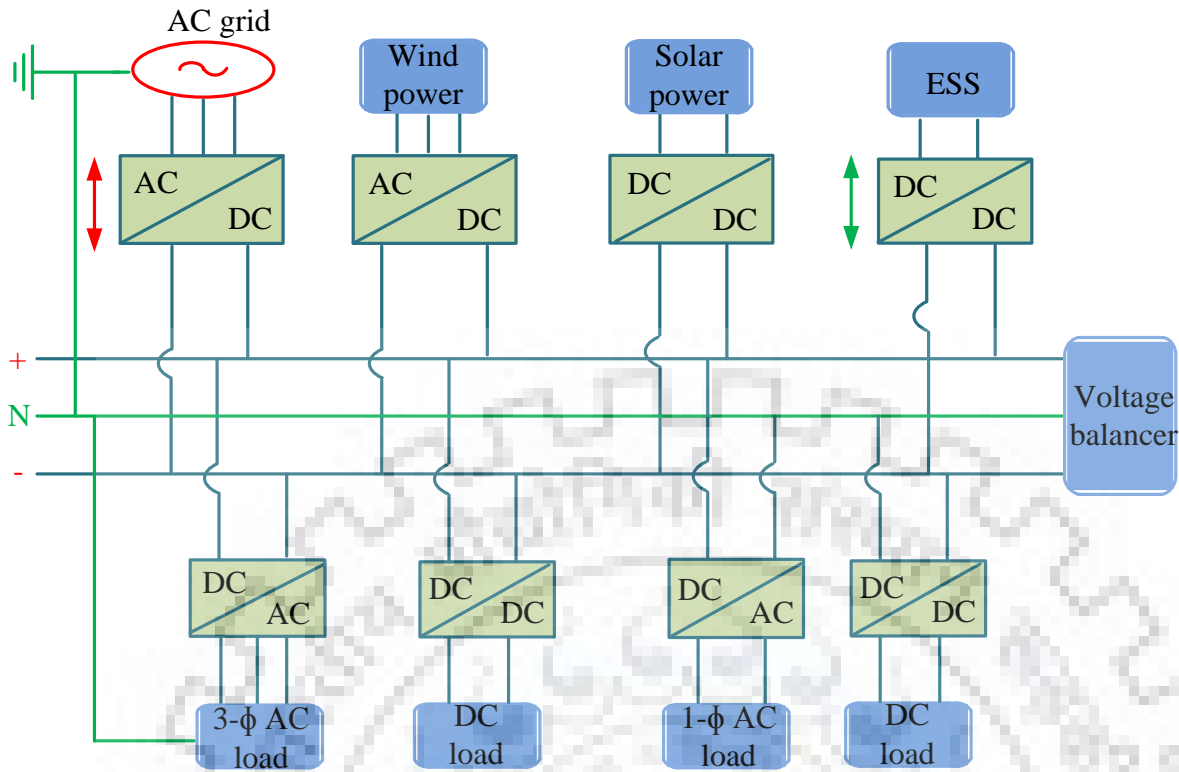


Fig. 3. 4: DC Microgrid Bipolar Topology Type

## 3.2. The DC Microgrid Power Management and Operation Strategy

### 3.2.1. DC Microgrid Power Management Techniques

In the hybrid DC $\mu$ G system, the DC bus voltage used as a control parameter for balancing power flow among the various terminals. The surplus/lack of generation output causes the DC bus voltage rising or dropping, respectively, with the change in input environmental conditions (such as wind speed and irradiation) and charging/discharging of BESS. These would result in power unbalance and causes voltage instability [72], [134]. Thus with the hybrid source DC $\mu$ G architecture proposed in this work, the system terminals broadly categorized into two; slack and power terminals. These terminals facilitate the system to maintain the bus voltage in the stable limit. The power terminals, such as variable generations (solar and wind power), regulate the power balance by delivering surplus power to the DC grid. However, the slack terminals maintain the power balance by absorbing or supplying the excess/deficit to/from the microgrid. The proposed DC $\mu$ G architecture shown in Fig. 3.5.

In this study, three different operating modes described; Mode-I (Islanding mode with battery charging and DG regulating bus voltage), Mode-II (Grid-connected with rectification mode), and Mode-III (Islanding mode with battery discharging).

The main control concern in the DC microgrid is to regulate the power balance in the existence of intermittent sources and loads. The power management is achieved by load shedding or using backup generation and energy storage. The DBS enables multiple sources of operation utilizing a droop control approach. The DC bus signaling is a control method that consists of voltage droop control and voltage level signaling.

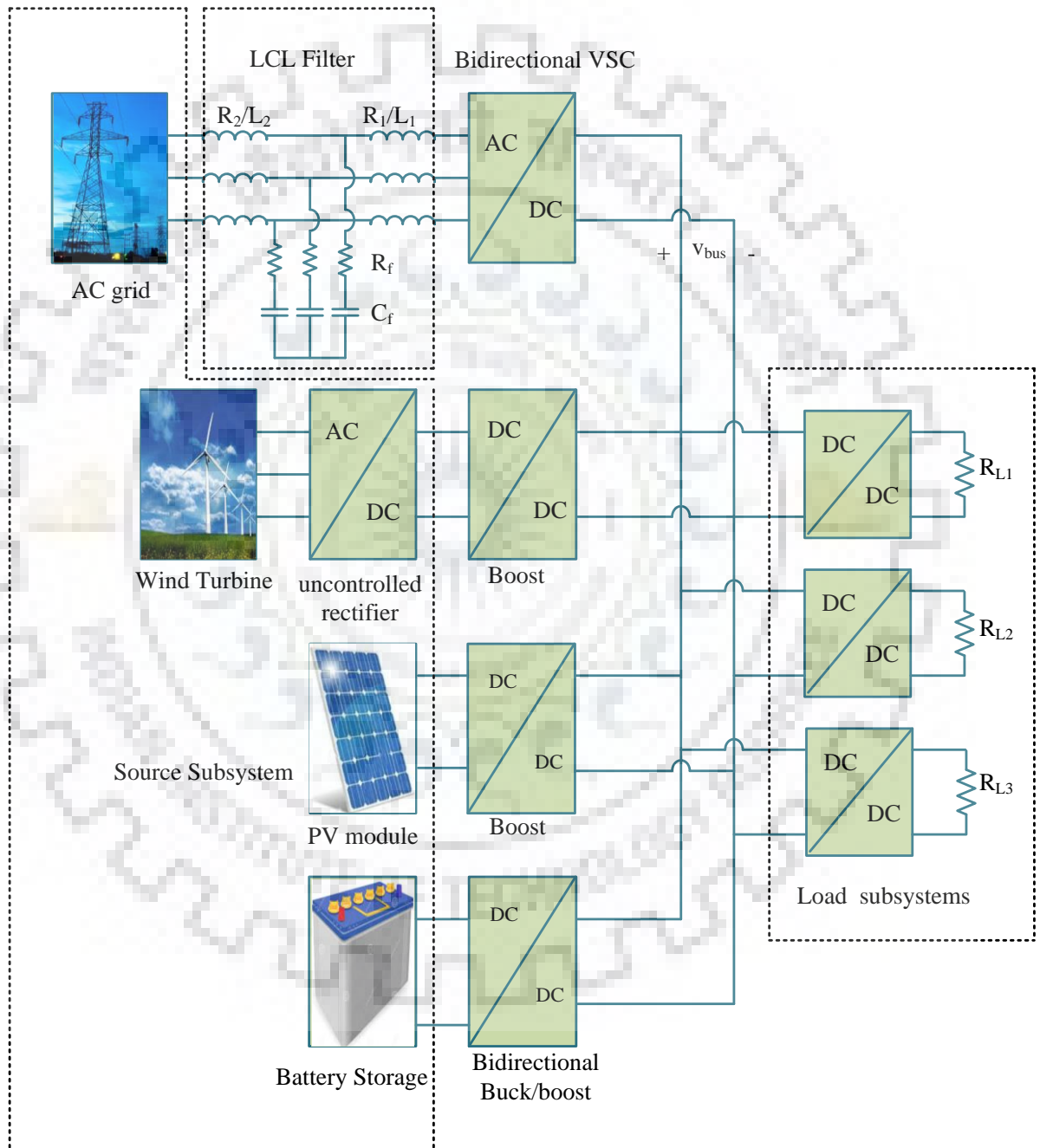


Fig. 3. 5: The Proposed DC Microgrid Configuration

The system mode switching is determined based on the bus voltage signal described by the logic system shown in Fig. 3.6. In this control method, the rectified G-VSC DC voltage set as

the nominal DC bus voltage ( $V_{DCn}$ ),  $\delta_{h2}$  and  $\delta_{h1}$  are designed at 5% and 2.5% higher than  $V_{DCn}$  respectively, but  $\delta_{L1}$  and  $\delta_{L2}$  are set at 2.5% and 5% below  $V_{DCn}$ , respectively, for BESS operation. Furthermore, wind and solar terminal voltages designed at  $V_{DCn} + \delta_{h2}V_{DCn}$  and  $V_{DCn} + \delta_{h1}V_{DCn}$  respectively. Whereas the battery storage and grid designed at  $V_{DCn} - \delta_{L1}V_{DCn}$  and  $V_{DCn}$  respectively; where  $\delta_{h2}$ ,  $\delta_{h1}$ ,  $\delta_{L1}$  &  $\delta_{L2}$  parameters that determine voltage levels [51].

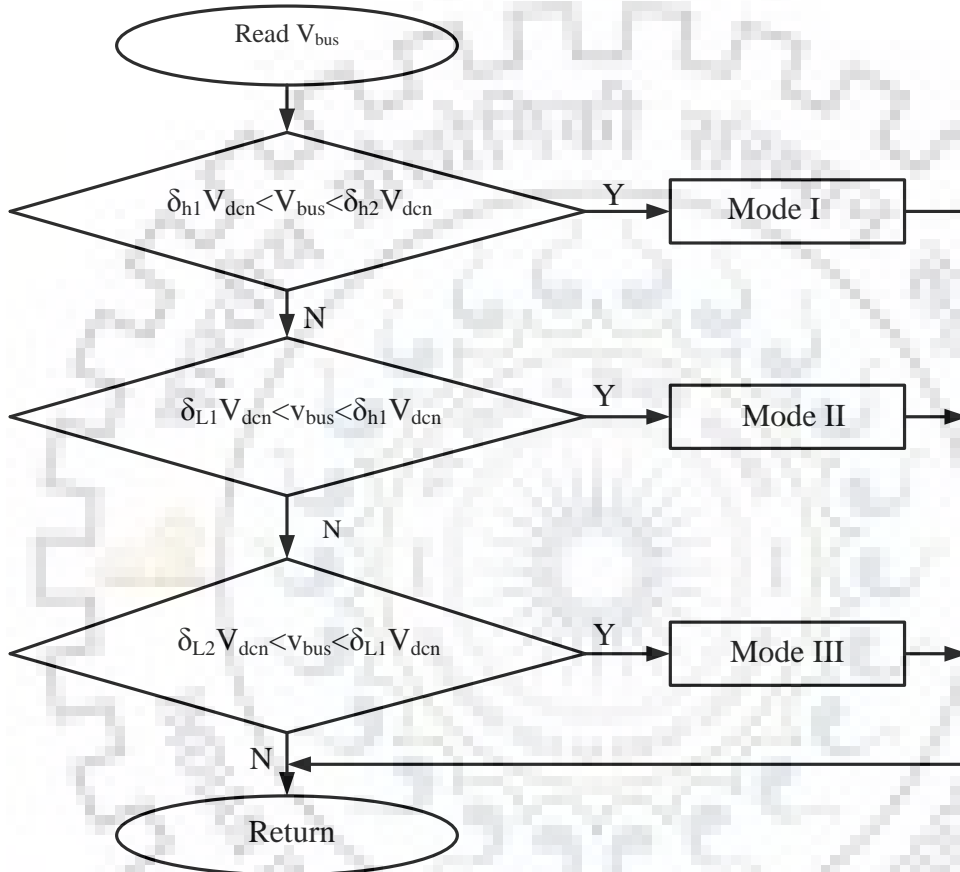


Fig. 3. 6: The System Switching Mode Logic Flow Chart

In practice for power balancing at the DC bus, there are many various interconnecting control problems such as practical usage of the energy storage system, exploiting DGs power production, and regulating bus voltage within the particular margin [22].

Accordingly, in the proposed hybrid DC $\mu$ G with multiple sources, the optimized operation is implemented through a decentralized control method that uses a DC bus signaling control technique. This control method allows the adaptive mode transition among the different operating modes [135], [136]. The control approach based on the bus voltage level is employed to regulate the proper function of the hybrid DC $\mu$ G system under varying input conditions.

### 3.2.2. DC Microgrid Operation

The microgrid operation broadly classified as islanding and grid-connected operating modes. In the two working ways, different controls, power management, and operation strategy methods applied to maintain the bus voltage. Due to the uncertainties such as the fluctuations of solar and wind power generation, grid-connection situation, and load changes made microgrid to operate in different modes to guarantee reliable and safe power supply [128]. The operating way of the hybrid DC $\mu$ G proposed in this study is categorized into three, as shown in Fig. 3.7. The system power management algorithm described in Fig. 3.8. The intended objective is to control the power flow among the autonomously controlled sources and storage unit and maintain the stability of the DC bus voltage within a specific range. The power flow at the various mode of operation presented in Table 3.1.

Table 3. 1: Power Flow Operation at Various Operating Modes

Operating Modes	DC $\mu$ G Operation type	Power Flow VSC	Power Flow Battery
DG	Islanded	$P_{\text{grid}} = 0$	$P_{\text{bat}} < 0$
G-VSC	Grid-connected	$P_{\text{grid}} > 0$	$P_{\text{bat}} < 0$
BESS	Islanded	$P_{\text{grid}} = 0$	$P_{\text{bat}} > 0$

#### a) Distributed Generation Mode

Fig. 3.7 (a) shows how the DG works. In this mode, the DC $\mu$ G works island-like. In this mode, the load power is less than the generation power. Due to the low load requirement, the bus voltage rises to the maximum limit, and the bus voltage works in the range of  $1.025V_{\text{DCn}} < v_{\text{bus}} < 1.05V_{\text{DCn}}$ . The excess energy from the DGs delivered to the battery for charging during this time. The DGs converter changes from MPPT control to constant voltage control to control the bus voltage. At this time, AC-grid disconnected, and the battery bidirectional converter regulates the bus by absorbing the excess power.



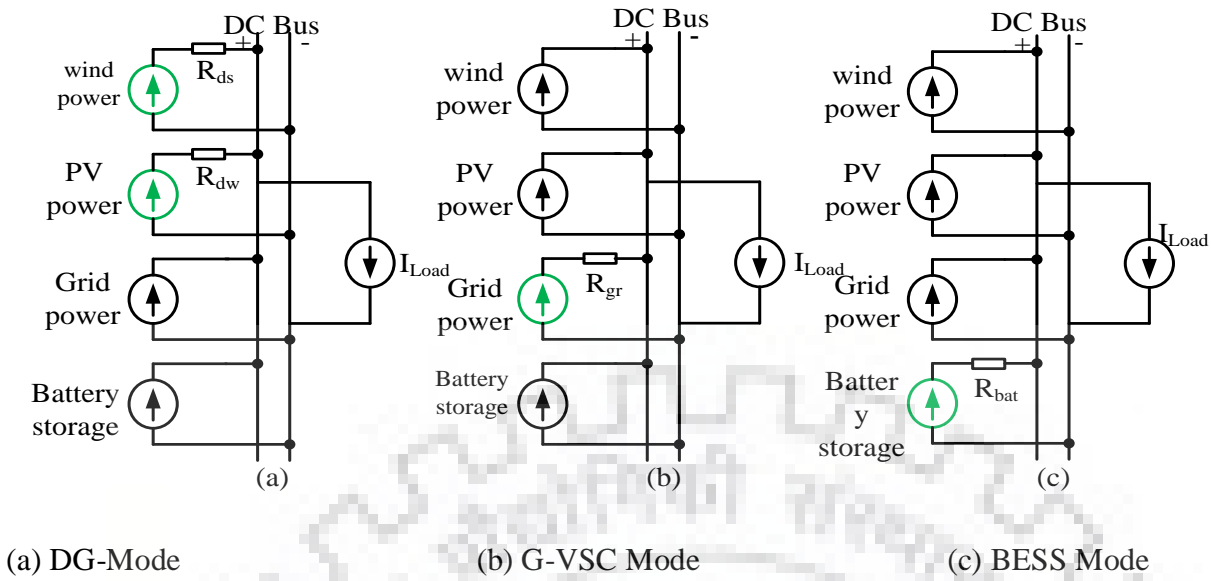


Fig. 3. 7: Operating Mode Definitions [18]

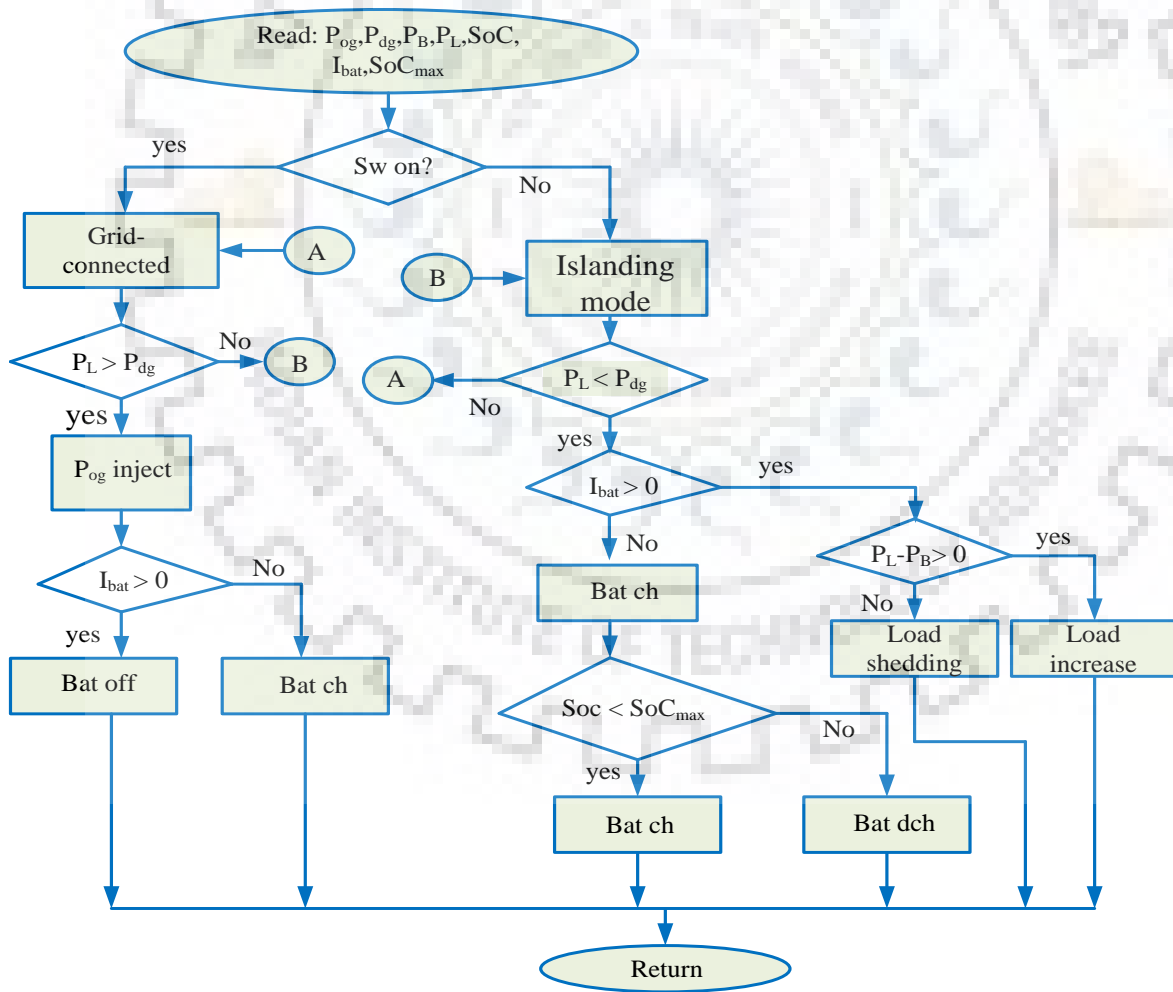


Fig. 3. 8: Power Management Schemes



### b) Grid-Connected Mode

The three-phase VSC is used to connect the AC network to a common DC link. This converter used to regulate voltage, current, and harmonics due to the non-linear switching processes of the converter. In this study, the grid-connected system set up to compensate for the lack of performance in insufficient generations of general directors to meet the load requirements by exporting electricity to the DC bus. During this period, the VSC assumed as a voltage source and the operating mode shown in Fig. 3.7 (b). The DGs converter during this mode operates at MPPT control. The battery energy system works in a charging operation. In this scenario, the operating bus voltage is between the range of  $0.975V_{DCn} < v_{bus} < 1.025V_{DCn}$ , where  $V_{DCn}$  is nominal DC bus voltage and  $v_{bus}$  the reference bus voltage.

### c) Battery Storage Mode

This operating mode portrayed in Fig. 3.8 (c). The VSC disconnected from the grid. However, the demand power is higher than the generation power. Since generation is less than power demand, the battery is regulating the DC bus power balance with discharging operation. Hence, it works as a voltage source. The DGs are working in MPPT control. During this time, the bus voltage decreased due to the decrease in generation power and increased power demand. In this case, the bus voltage is operating in the range of  $0.95V_{DCn} < v_{bus} < 0.975V_{DCn}$ .

## 3.3. DC Microgrid Power Flow Analysis

In the DC microgrid system, the main issues of power management are to regulate the active power balance among the energy sources, loads, BESS, and AC utility grid under any circumstance to ensure stable DC bus voltage. The DC voltage at the PCC maintained with a specific variation of limit [134]. The uncharacteristic DC-link energy can disturb the system operation or leads the entire system to collapse. For multiple sources of DC microgrid in a steady-state condition, the power balance equation can be formulated by:

$$P_{DG} + P_{Bat} + P_{AC} - P_{Load} = 0 \quad (3.1)$$

Where  $P_{DG}$ ,  $P_{Bat}$ ,  $P_{AC}$ , and  $P_{Load}$  represent DG, battery, AC grid, and load power, respectively. In the DC microgrid power network, the impedance of the transmission line has no imaginary parts, and the bus voltage has no phase angle.

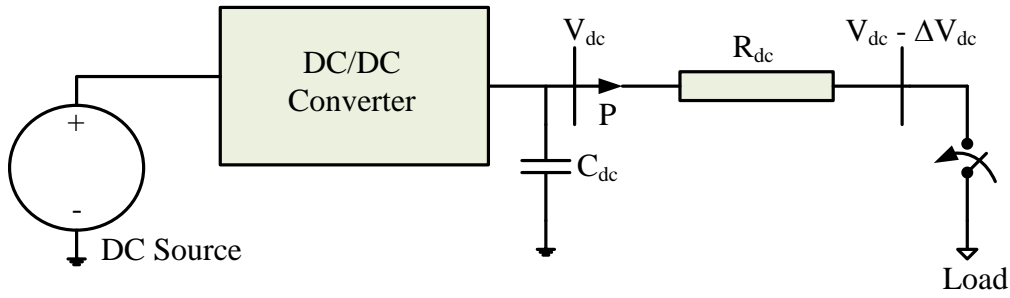


Fig. 3. 9: DC Grid Simplified Power System

Voltage and current are the only parameters used to control DC flow. In the DC network (see Fig. 3.9), the active power flow is proportional to the DC voltage ( $V_{DC}$ ). Therefore, the dynamic power can be controlled by the intermediate circuit voltage, as described by equation (1):

$$P = V_{DC} \frac{\Delta v_{DC}}{R_{DC}} \quad (3.2)$$

Where

$\Delta v_{DC}$  is the voltage drop over the line resistance ( $R_{DC}$ )

In DC grid increasing load, decreases the voltage of DC-link capacitor ( $C_{DC}$ ).

### 3.4. DC Microgrid Control Strategies

The wind and solar distributed generations are becoming the most popular distributed renewable energy sources for microgrid applications. A hybrid wind and PV source with a grid-connected system provides more reliability and higher quality power to the load than a system with a single source in the microgrid system [22]. In such an order, the power electronic interfacing converters are used for integrating the different DERs and regulate the voltage, frequency, and power between the source and load subsystems. The increasing number of RES penetrations in the new distribution network and the increased consumer energy demands from a nearby site encouraged the deployment of DC $\mu$ G with multiple sources and energy storage opportunities for reliability as well as stability issues in the integrated systems [23], [24], [25]. In the case of different sources of DC $\mu$ G interfaced in parallel, each reference in the network participates in supporting each other via an integrated and power management control strategies. Consequently, this can provide various benefits such as the optimal operation of the DC $\mu$ G subsystem through a coordinated control scheme that maximizes utilization of DGs and BESS [23], [26]. Also, it maintains the reliability and power balance of the DC $\mu$ G during distributed generation intermittency and load disturbances [24], [25]. The fluctuating output characteristics of DGs, the dynamic interaction between the source and load interfacing

converters, and a sudden load changing are the leading causes of stability problems of bus voltage in the microgrid system in various sources integrated [22]. Therefore, for realizing the reliable and flexible operation of DC $\mu$ G with various electronically coupled sources, different control techniques are proposed in [23], [137], and [117]. Integrated service of DC $\mu$ G with multiple source control schemes that are suitable for load sharing broadly classified into two: namely passive and active load sharing [138], [139].

In the case of proactive load sharing approaches, there are three different popular control methods: namely centralized control [140], master-slave control [62], [141], and average current control [142]. However, these control approaches have the drawback that requires communication in the central power that coordinates the parallel operation of each unit. The central control mechanism degrades the system reliability, flexibility, and it is more susceptible to failure with a single point fault in the system. In addition, the master control solution also has a similar limitation with centralized control which in result failure of voltage regulation if the master-slave face failure [62].

A decentralized control (passive load sharing) structure is reported in [71], [72], [136], for multiple sources of DC $\mu$ G. This control system enables to perform local control variables at individual interfacing converters to realize the power regulation and voltage. Besides, every power converter in the method employed independent control without any communication link between different units, and hence, this decrease system cost while improving the reliability of the system.

The control scheme uses a droop control that can be implemented by the addition of a "virtual resistor" in the local function. The droop control allows the load sharing in parallel operation of different sources. Because of its reliability and modularity, droop controls have been employed in the DC $\mu$ G system [71], [136]. Thus, for practical and reliable operation of DC $\mu$ G, a suitable integrated control strategy is required.

In this study, the coordinated decentralized control strategy for the various sources and loads proposed. A DC $\mu$ G composed of wind-solar hybrid RES and BESS with grid-connected or islanded operations that allow flexible and reliable performance with seamless mode transition presented. The proposed control system uses the DC bus voltage level as a communication signal. The DC bus voltage signaling is implemented with autonomously controlled source units to stabilize the DC bus voltage variations. Due to the fluctuating behavior of the wind speed and solar insolation of RES and sudden load changes, the bus voltage varies. Moreover,

the system realizes the optimal operation of the DC $\mu$ G by maximizing the distributed generations with voltage and maximum power control mode with the decrease/increase in load demand, maintaining the economical service of ESS, and regulating the bus voltage within the particular margins.

### 3.5. Basic Concept and Analysis of Droop Control

The droop control is an autonomous or independent control with no communication link between the parallel interfacing converters. The control techniques are mainly used for load sharing purposes and maintain grid frequency and amplitude of AC voltage in the case of AC microgrid and DC voltage in DC $\mu$ G systems. Moreover, the control scheme suppresses the circulating current between the micro source units. Initially, the concept of droop control was used in the AC power system to control reactive and real power flows, in the case of several generators paralleled the primary grid.

#### 3.5.1. Droop Control in AC Microgrid

In the AC microgrid, the droop control used to control the real and reactive power exchanges. The voltage droop (responsive power control) and frequency droop (real power control) characteristics are applied in voltage mode control, as depicted in Fig. 3.10. The control strategies used to regulate the load sharing without the need for communication links and control the active and reactive power transfer with the utility grid assuming grid frequency and amplitude of the AC voltage under control [143].

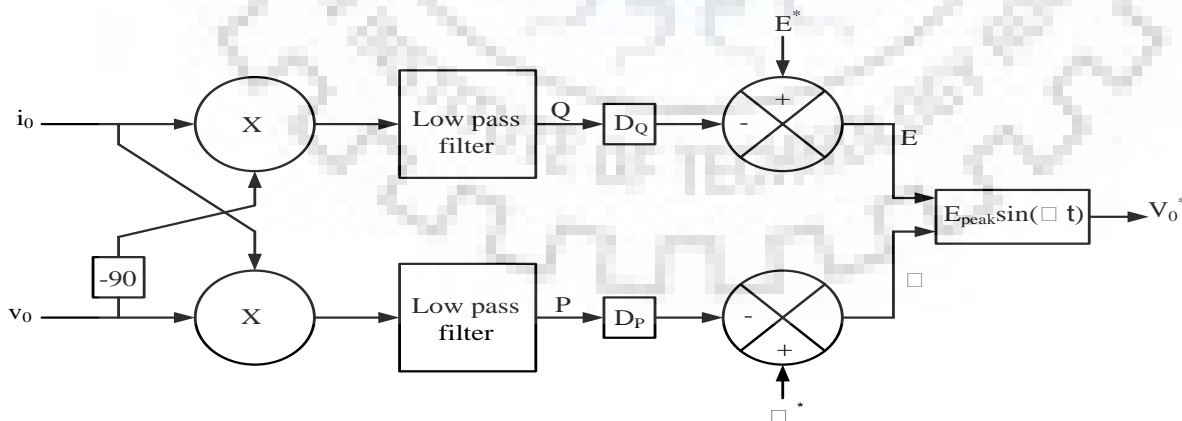


Fig. 3. 10: AC Microgrid Droop Control Scheme

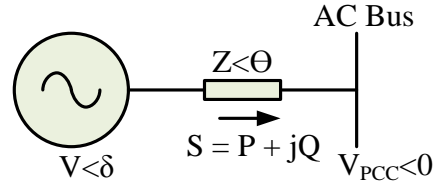


Fig. 3. 11: Simplified AC Equivalent Circuit

The droop control principle for the AC microgrid described with a simplified VSC equivalent circuit coupled to the AC bus (see Fig. 3.11). Neglecting the high harmonics and switching ripples, the converter modeled by AC source voltage  $V\angle\delta$ . Moreover, the voltage at PCC described as  $V_{PCC}\angle 0$  and the line impedance and output impedance of the converter represented as a single equivalent impedance of  $Z\angle\theta$ . Thus, the system complex power provided to the typical AC bus formulated as:

$$S = V_{PCC}I^* = \frac{V_{PCC}V\angle\theta-\delta}{Z} - \frac{V_{PCC}^2\angle\theta}{Z} \quad (3.3)$$

From (3.3), active and reactive powers derived as:

$$P = \frac{V_{PCC}V}{Z} \cos(\theta - \delta) - \frac{V_{PCC}^2}{Z} \cos(\theta) \quad (3.4)$$

$$Q = \frac{V_{PCC}V}{Z} \sin(\theta - \delta) - \frac{V_{PCC}^2}{Z} \sin(\theta) \quad (3.5)$$

The real line impedance,  $Z\angle\theta$ , is to be purely inductive,  $\theta = 90^\circ$ , then (2) is simplified to:

$$P = \frac{V_{PCC}V}{Z} \sin\delta \quad (3.6)$$

$$Q = \frac{V_{PCC}V\cos\delta - V_{PCC}^2}{Z} \quad (3.7)$$

If the phase difference between the common AC bus voltage  $\delta$  and the converter output voltage is insignificant, then  $\cos\delta \approx 1$  and  $\sin\delta \approx \delta$ . As a result, the voltage and frequency droop characteristics employed and fine-tuned to generate the voltage reference of the converter [143], as illustrated in Fig. 3.10 according to:

$$\omega = \omega^* - k_p P \quad (3.8)$$

$$E = E^* - k_q Q \quad (3.9)$$

Where  $\omega^*$  and  $E^*$  the distributed source angular frequency and output voltage RMS at no-load, respectively. The droop parameters,  $k_p$  and  $k_q$  are design parameters and can be determined

based on the nominal power rating of the converter by considering frequency deviations and maximum tolerable voltage.

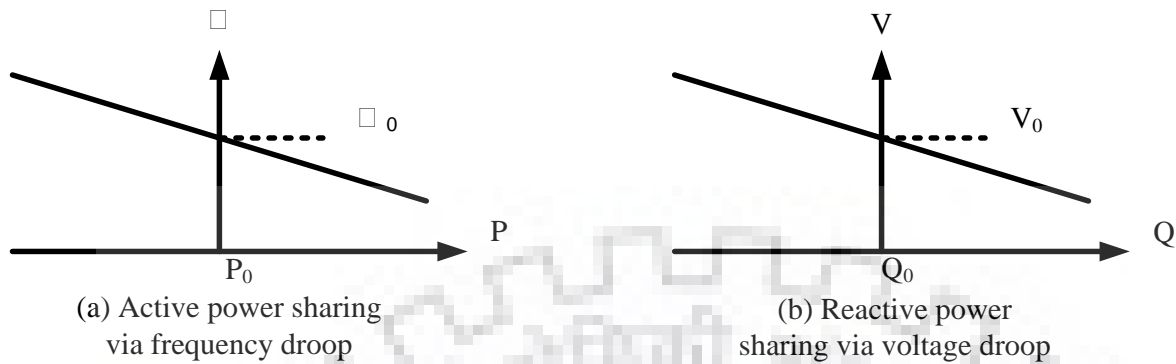


Fig. 3. 12: Droop Control Characteristic

As shown in Fig. 3.12, frequency, and Voltage are the two parameters that required to control in AC microgrids. Frequency is controlled by decreasing or increasing the input mechanical power, and voltage is controlled by absorbing or injecting reactive power [143].

### 3.5.2. Droop Control in DC Microgrid

The DC $\mu$ G power system has no frequency. As a result, it cannot form reactance. Besides, there will be no phase-shift between current and DC voltage, as well as reactive power that does not exist in the DC system. Thus, DC voltage is the only parameter required controlling. The DC voltage regulated by injecting energy into the DC grid. For example, if the supplied power is higher than the power demand of the existing loads, then the DC bus voltage increases. On the other hand, if all the generating sources and loads connected to a universal DC bus via their interfacing converters, the sum of each converter's output power should always be zero [134]. For this reason, a suitable DC voltage controller in DC $\mu$ G must continuously monitor the power balance to provide appropriate instructions to the microgrid components such as generating sources, loads, and converters.

The droop control introduced to eliminate the dependence on one power converter. Furthermore, it facilitates collective voltage control among the various converters that paralleled to the DC network. With droop control, the system keeps on operating even if with single failure or interruption of one of the voltages regulating terminal. The continuing terminals are responsible for managing the bus voltage within its specified margins. The droop control primarily employed for load sharing purposes. The feedback signal for droop control



can be chosen as an output current or power in DC $\mu$ G to control the DC bus voltage, and it implemented in the local control scheme [75].

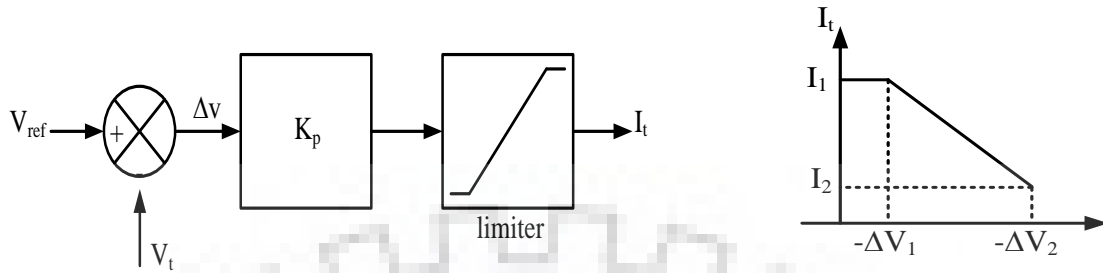


Fig. 3.13 (a) Control block of DC voltage with droop

Fig. 3.13 (b) I-V characteristics of DC voltage droop

Fig. 3. 13: DC Voltage Droop Control and I-V Characteristics Schematics

The power-based method employs a P-V characteristic curve for controlling the voltage, while the current-based approach uses an I-V characteristic curve (see Fig. 3.13b). For individual terminals that operate in voltage droop mode, the power (current) and voltage represented in a linear relationship characteristic, as depicted in Fig. 3.13 (a).

### 3.5.3. Analysis of Droop Control in DC Power System

In DC, the power system droop control usually used to maintain the reliability and modularity inherent in its scheme. With the droop control approach, the output voltage of the unit decreases as the output load current increases. The droop equation can be described mathematically by (3.10)

$$V_{bus} = V_{ref} - R_d i_o \quad (3.10)$$

The (3.10) shows that the desired output DC bus voltage managed with the change in distributed energy resources output current.  $V_{ref}$  and  $R_d$  are controllable parameters and represent the DERs converter reference voltage and droop resistance, respectively. The droop resistance is calculated by:

$$R_d = \frac{\Delta v_{bus}}{i_{max}} \quad (3.11)$$

The distributed sources working in voltage droop mode, each reference in the system are accountable to make the bus voltage stable so that the current at each terminal converter is given by [51]:

$$i_s = i_1 + i_2 + i_3 + i_4 \quad (3.12)$$

Assume that all sources have the same reference voltage with constant voltage control operation [144], the reference bus voltage calculated as:

$$V_{bus} = V_{ref} - \frac{1}{\sum_{i=1}^n \frac{1}{R_{di}}} i_s = V_{ref} - R_d i_o \quad (3.13)$$

The power change supplied from parallel sources analyzed by considering a simplified two sources supplying power to the load. The DC $\mu$ G source components listed in Table 3.2. The equivalent steady-state analysis of the simplified circuit modeled using source units as a voltage source in series with droop impedance depicted in Fig. 3.14.

Table 3. 2: DC $\mu$ G Components Design Parameter

Units	Types of interfacing converter	Rated power	Droop resistance
Wind turbine	Boost converter (nonisolated)	7 kW	1.25 $\Omega$
PV Module	Boost converter (nonisolated)	11 kW	0.86 $\Omega$
AC grid	3-phase VSC	5 kW	1.90 $\Omega$
Batter (ESS)	Bidirectional Buck/boost	5 kW	1.90 $\Omega$

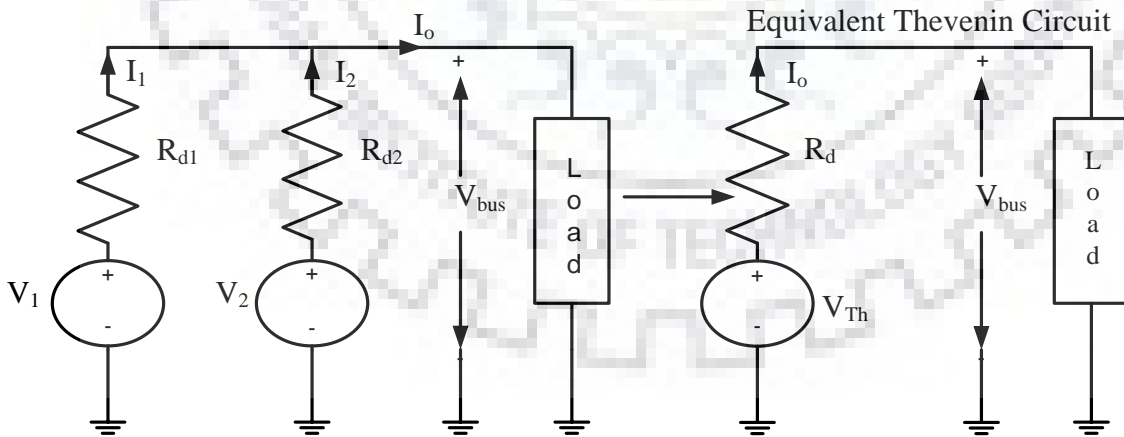


Fig. 3. 14: A Simplified Equivalent Circuit for Two Sources Connected in Parallel Supplying a Load and Its Thevenin Equivalent [144]

Thus the change of current delivered by source is given by:

$$I_1 - I_2 = \frac{2(V_1 - V_2)}{R_{d1} + R_{d2}} + \frac{(R_{d1} - R_{d2})}{R_{d1} + R_{d2}} I_o \quad (3.14)$$



$$V_{bus} = V_{Th} - R_d I_0 \quad (3.15)$$

Where  $V_{Th} = \frac{V_1 R_{d2} + V_2 R_{d1}}{R_{d1} + R_{d2}}$  and  $R_d = \frac{R_{d1} R_{d2}}{R_{d1} + R_{d2}}$

Equation (3.14) & (3.15) shows that the change in current delivered by each generating unit is inversely proportional to the sum of droop resistances. Consequently, as the total droop resistances increased, this decreases the difference between currents. However, increasing droop resistances leads to poor voltage regulation. Thus, there must be a trade-off between load sharing and voltage regulation [144].

### 3.6. Constant Power Load Modelling

For proper functioning, every load in DC microgrid requires a specific voltage level. As a result, this enables the system to have a point of load converter. In this case, the buck converter tightly regulated to sustain constant output voltage, as depicted in Fig. 3.15 [75], [51].

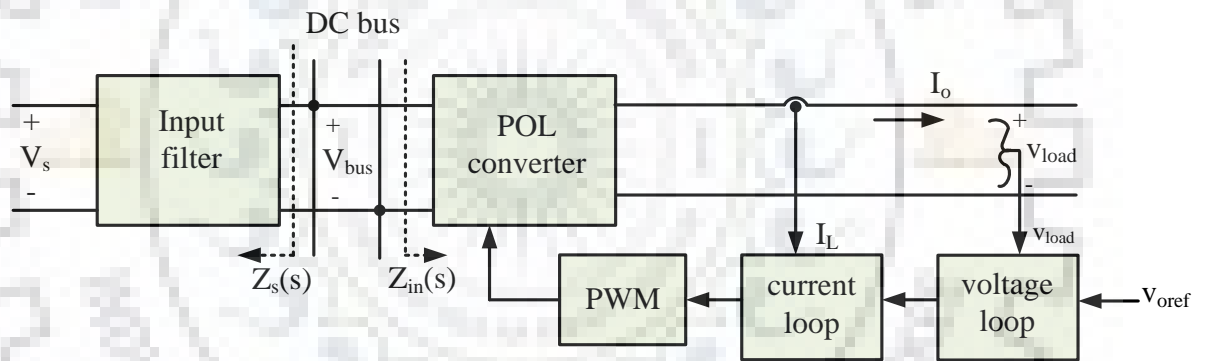


Fig. 3. 15: Point of Load Converter (buck) Schematics with Input Filter

The input impedance of the system is not equal; however, the output and input power of POL converters are approximately equivalent. Thus the POL behaves as CPL. Regardless of any changes in the primary DC bus voltage, the load output voltage maintained constant by adjusting the duty ratio of the POL converter via tuning the voltage control loop. The output load converter is kept constant with a dual PI controller system (voltage and current control loop).

The CPL can be described mathematically as a voltage-controlled current source:

$$i_{CPL} = \frac{P_{CPL}}{V_{bus}} \quad (3.16)$$

The CPLs supplied from the universal DC bus via the transmission lines. Each transmission line of the load is modeled with a differential equation to form a single equivalent circuit transmission line [145]. The differential equations are described by

$$\begin{aligned}
\frac{di_1}{dt} &= \frac{1}{L_1} (V_{sr} - v_{c1}) - \frac{r_1}{L_1} i_1 \\
\frac{di_2}{dt} &= \frac{1}{L_2} (V_{sr} - v_{c2}) - \frac{r_2}{L_2} i_2 \\
\frac{di_3}{dt} &= \frac{1}{L_3} (V_{sr} - v_{c3}) - \frac{r_3}{L_3} i_3 \\
&\vdots \\
\frac{di_n}{dt} &= \frac{1}{L_n} (V_{sr} - v_{cn}) - \frac{r_n}{L_n} i_n
\end{aligned} \tag{3.17}$$

Where  $L_i$  and  $r_i$  are the transmission line impedance of  $CPL_i$ ; whereas  $v_{ci}$  and  $i_i$  the input voltage and current, respectively. The sources supply the total input current is given by:

$$i_{eq} = i_1 + i_2 + i_3 \dots + i_n \tag{3.18}$$

Suppose that the same reference voltage  $V_{sr}$  for all interfacing source converters coupled in parallel, the following condition met:

$$V_{sr} = V_{s1} = V_{s2} = V_{s3} = V_s \tag{3.19}$$

And assuming the ratio of the transmission lines are approximately equal.

$$\frac{r_1}{L_1} \approx \frac{r_2}{L_2} \approx \dots \approx \frac{r_n}{L_n} \tag{3.20}$$

Thus, the single differential equation can be described by:

$$\frac{di_{eq}}{dt} = \frac{d}{dt} \sum_{i=1}^3 i_i \approx \left( \sum_{i=1}^3 \frac{1}{L_i} \right) (V_s - v_{eq}) - \sum_{i=1}^3 \frac{r_i}{L_i} i_{eq} \tag{3.21}$$

Where  $L_{eq}$  can be calculated by

$$L_{eq} = \frac{1}{\sum_{i=1}^n \frac{1}{L_{ki}}} \tag{3.22}$$

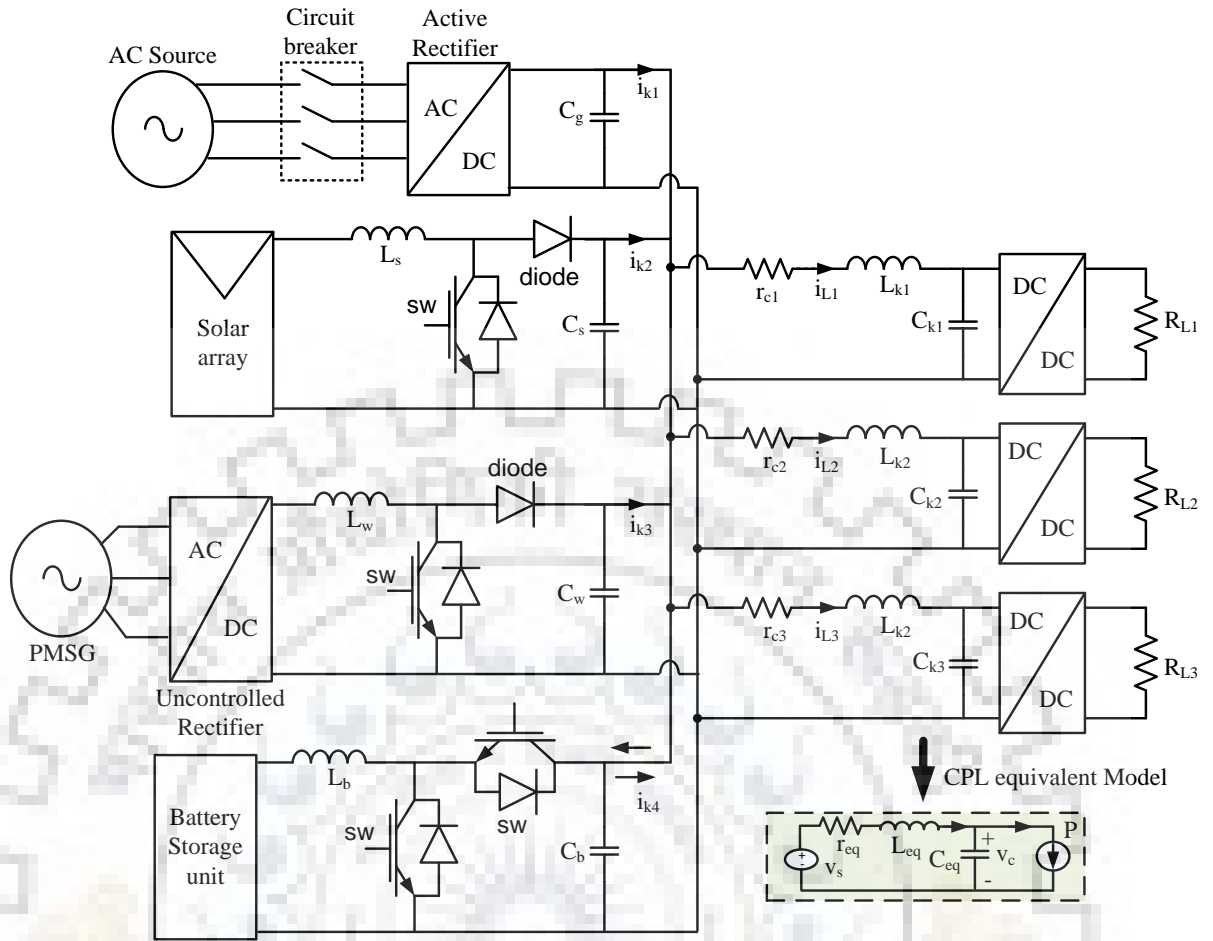


Fig. 3. 16: Proposed DC Microgrid Equivalent Circuit, Model

Multiplying both sides of (3.21) by (3.22), the simplified equation described as:

$$L_{eq} \frac{di_{eq}}{dt} = \frac{d}{dt} \sum_{i=1}^3 i_i \approx (V_s - v_{eq}) - R_{eq} i_{eq} \quad (3.23)$$

And where  $R_{eq} = L_{eq} \frac{r_i}{L_i}$ .

$L_{eq}$  and  $R_{eq}$  are the equivalent inductance and resistance of the simplified line model. With this value, the n differential equation reduced to a single differential equation. Similarly, the equivalent capacitance calculated by:

$$C_{eq} = C_1 + C_2 + C_3 \quad (3.24)$$

The simplified single-line equivalent of the proposed DC microgrid circuit represented in Fig. 3.16. The total power  $P$  realized by the difference between CPS generation and consumption power  $P_{CPL}$ .

### 3.7. Concept of the Real-Time Simulator

Real-time simulations are essential to verify the controller performance and accuracy since models developed in real-time executed at the same rate as the actual physical system. The OPAL-RT simulator interacts with Matlab/Simulink SimPowerSystems through RT-LAB software. The fundamental purpose of the simulator is to implement real-time, HIL, and control-in-the-loop (CIL) simulations. In this chapter, the developed DC $\mu$ G model with Simulink using SimPowerSystems is performed in real-time simulation using ARTEMiS-SSN solver. This solver used to decouple large power systems state-space into smaller groups, whose solutions can be obtained simultaneously by using a nodal admittance method. Also, it provides a fast and accurate real-time simulation of DC $\mu$ G systems using the most advanced processors. The ARTEMiS-SSN performs parallel execution by assigning multiple cores per CPU for computations of subsystems that contain several state-space nodal (SSN) groups. The DC $\mu$ G system shown in Fig.3.5 consists of significant electrical components (such as grid source, wind turbine generator, solar PV array, and battery blocks) and smaller power electronic components (such as switches and breakers). The proposed DC $\mu$ G simulated with a time-step of 20 $\mu$ s on 2.8 cores, 3.2 GHz processor speed, and 16 GB RAM of the OPAL-RT simulator. The real-time simulation performed by decoupling the more significant electrical components into smaller electrical components with ARTEMiS-SSN. The parallel tasks built from the Simulink model using RT-LAB, and each task assigned on the processor of the multicore computer and the whole simulation can be run [146]. The DC $\mu$ G model simulation set up via the OPAL-RT digital simulator presented in Fig. 3.17.

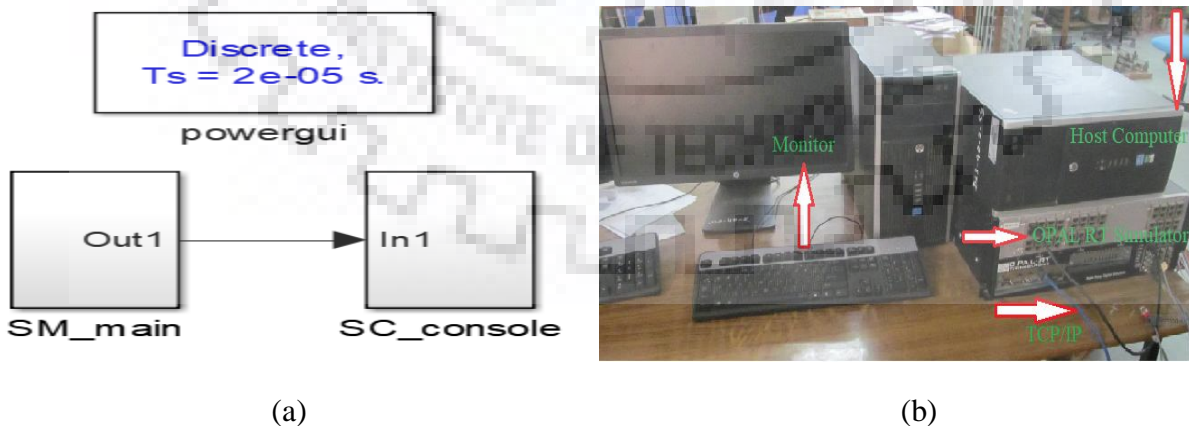


Fig. 3. 17: The set up of real-time simulation with OPAL-RT Simulator; (a) Simulink Model Using RT LAB, (b) Simulator Set-up Picture

### 3.8. Simulation Result Discussion

The effectiveness of the decentralized control scheme using DC bus voltage signaling verified via the hybrid DC microgrid system model developed in Matlab/Simulink. With some modification, it is simulated using OPAL-RT, RT-LAB real-time simulation environment. The simulation carried out using a fixed-step and sample time of 20 $\mu$ sec. The proposed DC $\mu$ G architecture shown in Fig. 3.5 consists of G-VSC, PV array, and wind turbine interfaced with the DC grid via their respective power converters. The boost DC/DC converter connects the PV and wind power sources with the DC grid. While the BESS linked to the primary DC grid via a bidirectional buck/boost converter. The DC loads are supplied power from the universal DC bus through buck DC/DC interface converter. Uncertainties such as the fluctuations of solar and wind power generation change the microgrid operation system categorized into three different operating modes to guarantee a reliable and safe power supply. Accordingly, the control system of the micro sources and load are programmed to change mode transitions between the various alternatives. The DC bus voltages are operating in the proposed DC $\mu$ G at the different modes listed in Table 3.3.

Table 3. 3: Bus Voltages at Different Operating Modes

DG-Mode	G-VSC Mode	BESS Mode
$\geq 665\text{V}$	$\geq 650\text{V}$	$\geq 634\text{V}$

The DC $\mu$ G bus voltage nominal rating chosen to be 650 V. The specific tolerable operating bus voltage designed is to be in the range 620 V to 680 V, as presented in Fig. 3.18.

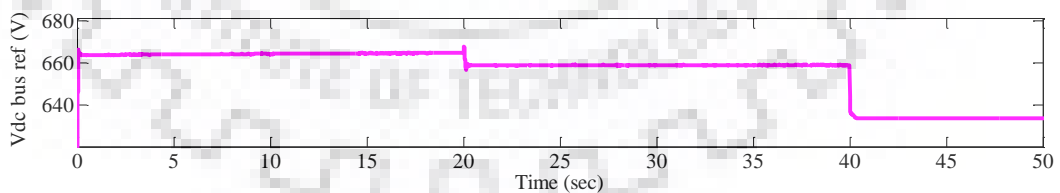


Fig. 3. 18: DC Bus Reference Voltage

#### Case 1: Distributed generation mode

A sudden change input disturbance is applied using step signal for PV and wind turbine source units, as shown in Fig. 3.19 (a) and Fig. 3.20 (a). In this scenario, the DGs interfacing boost converter employed two control strategies, such as the constant power and constant voltage

control to regulate the DC $\mu$ G bus voltage. Since the solar and wind power boost DC/DC converter is unidirectional, the converter output currents are positive, as can be observed in Fig. 3.19 (b) & 3.20 (b).

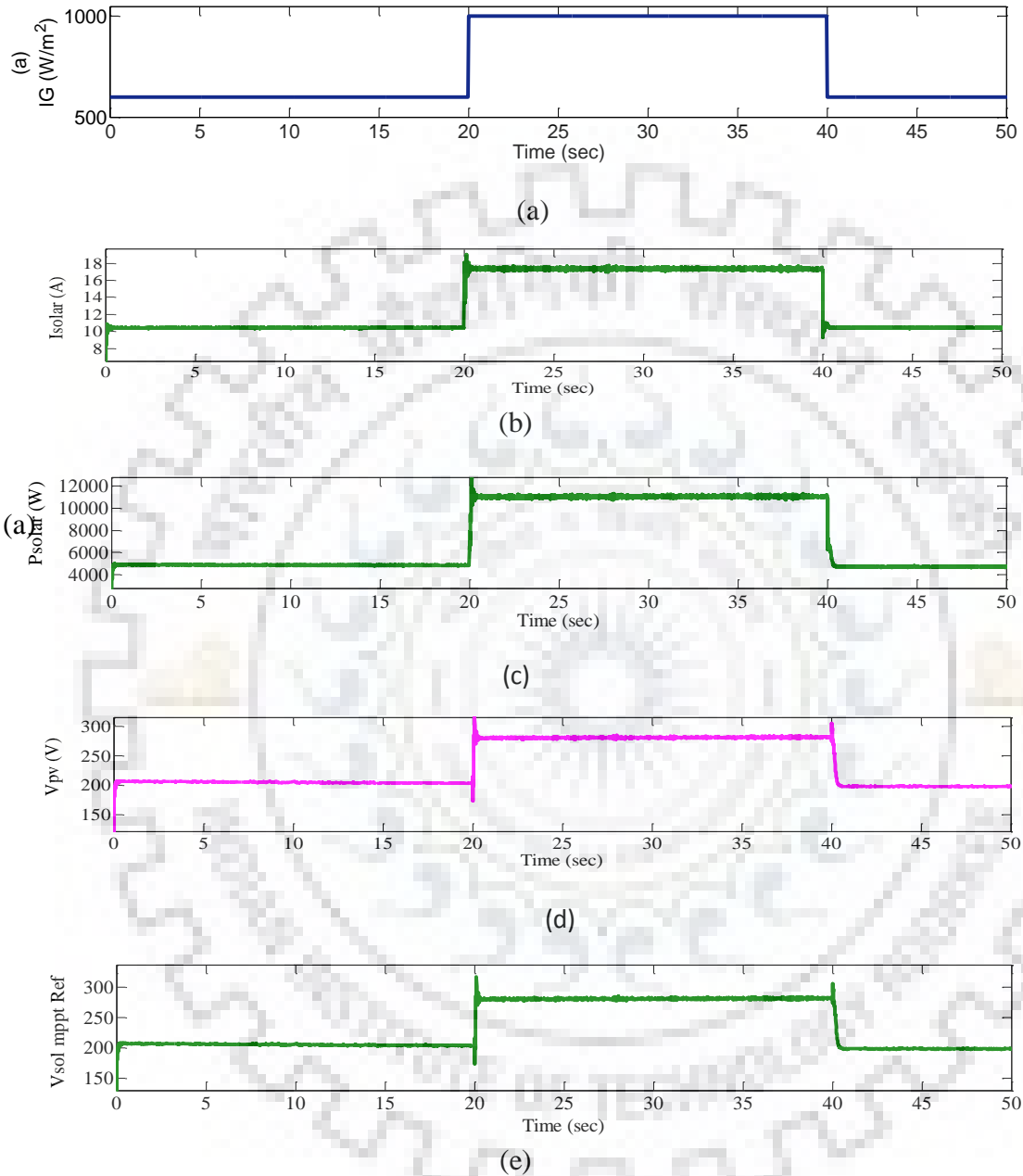


Fig. 3. 19: Simulation Result of Solar Power Components; (a) Irradiation, (b) Converter Output Current, (c) Converter Output Power, (d) Input Boost Converter Voltage, (e) Solar MPPT Reference Voltage

During the period  $t = 0$  to  $t = 20$  sec, the load demand is less than a generation. As a result, the DG converters terminals take responsibility for adjusting the bus voltage by functioning in voltage droop control mode. Due to low load demand, the bus voltage increased, and it is working in the range between 665 V to 682 V (see Fig. 3.18). As soon as the maximum power point reached, it remains operating in this mode in a constant power source control.

Fig. 3.19 (b) & 3.20 (b) depict the output power generation variation from wind and PV, respectively. During the time duration  $t = 0 - 20$  sec, the power generation from wind and PV is more than demanded by load, which is 2.5 kW and 5 kW, respectively (total production is 7.5 kW). However, the overall demand power is 2.5 kW and is less than the full DG power, as shown in Fig. 3.23 (b). In this period, the DC $\mu$ G is in islanding mode with generation from DGs is higher than the power required by the load. As a result, the surplus power from DGs is charging the battery. Besides, in this mode, the battery is regulating the bus by absorbing the extra energy. Due to the less load power demand, the bus voltage is higher than the nominal bus voltage. Consequently, the DG interfacing converter's shift to the constant voltage control limiting the bus voltage within its acceptable range.

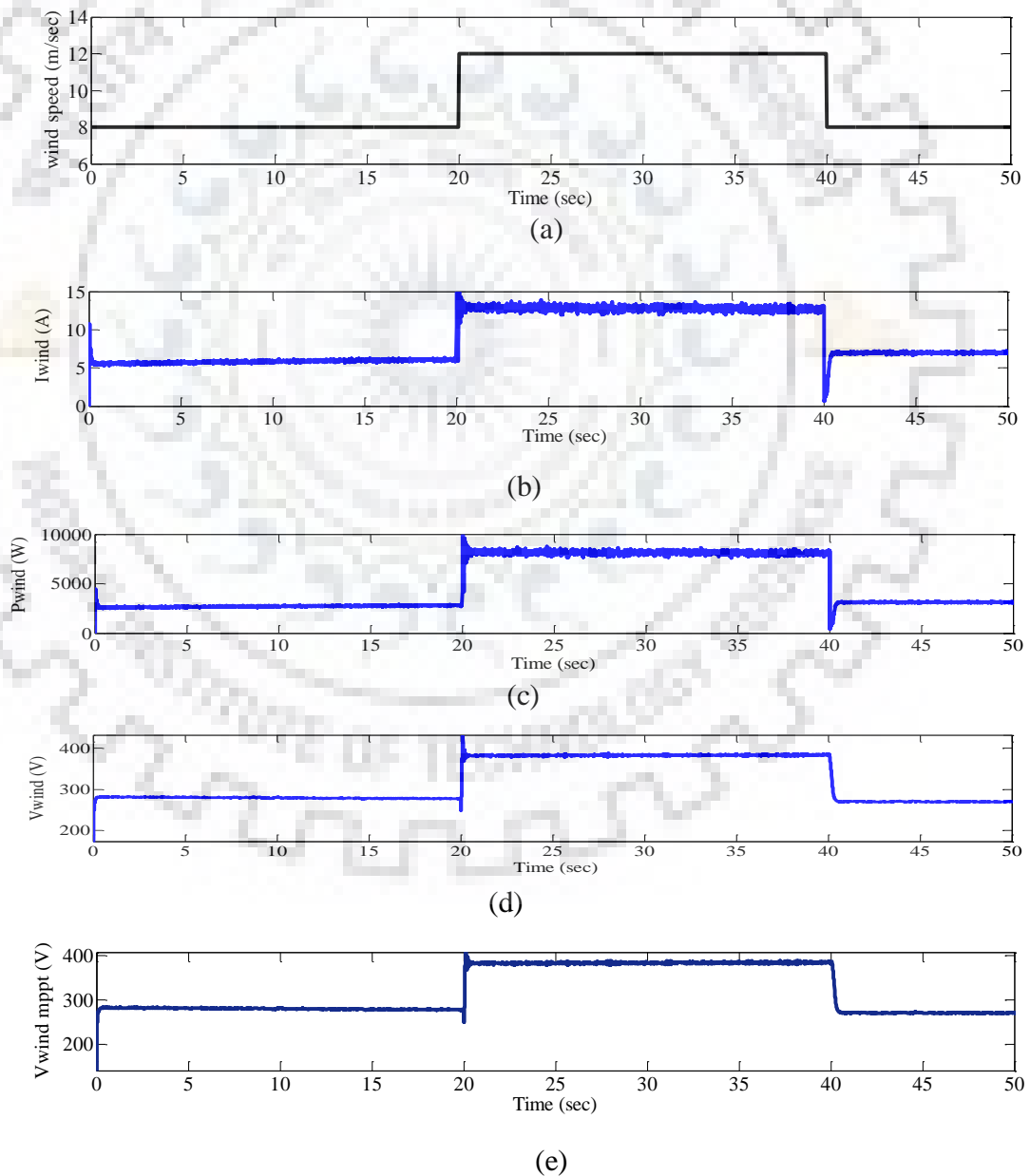


Fig. 3. 20: Simulation Result of Wind Generation Components; (a) Wind Speed, (b) Converter Output Current, (c) Converter Output Power, (d) Input to Boost Converter Voltage, (e) Wind MPPT Reference Voltage

**Case 2: Grid Connected Mode**

In this case, the DC bus voltage is operated in the range between 650 V- 665 V, as shown in Fig. 3.18 from the 20 - 40-sec duration. Similarly, as shown in Fig. 3.19 (a) and 3.20 (a), PV and wind turbines operate with 1000 (W/m<sup>2</sup>) insolation and 12 (m/s) wind speed respectively and work in MPPT control mode.

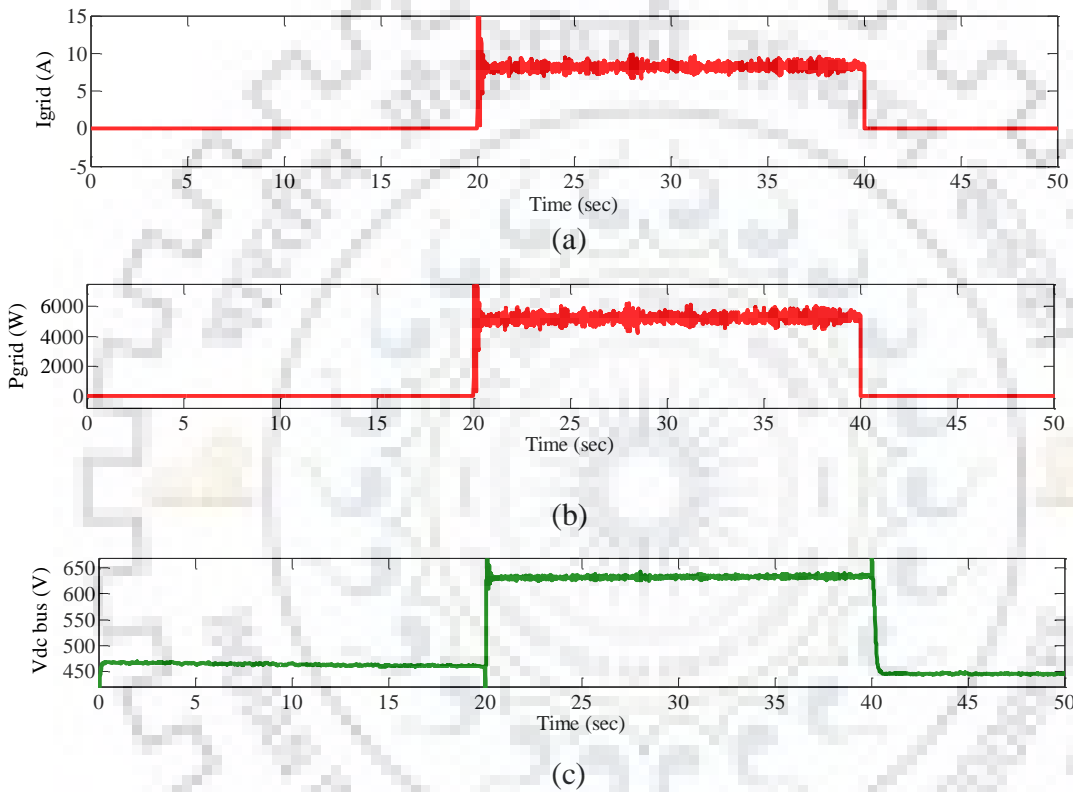


Fig. 3. 21: G-VSC Output Parameters; (a) Current, (b) Power (watt), (c) DC Voltage

During this period, the power demand is increased to 23 kW, as shown in Fig. 3.22 (b) & 3.23 (b). In this scenario, DGs are also operating at their maximum PowerPoint. However, in this duration, the total DGs generation power is 18 kW (11 kW from solar and 7 kW from wind), as can be observed from Fig. 3.19 (b) & 3.20 (b). Thus to compensate the deficit G-VSC is connected to supply 5 kW power as illustrated in Fig. 3.21 (b). As a result, G-VSC is regulating the bus by delivering the deficient power for the load and increase reliability.

**Case 3: Battery Energy Storage Mode**

During the period  $t = 40.01 - 50$  sec, the G-VSC is disconnected, and the power generation from DG also decreased from 18 kW to 8 kW. At this time, the load power is 10 kW, as



depicted in Fig. 3.23 (b) that is greater than the generation capacity. In this scenario, since generation decreased, the DC bus voltage also reduced. Thus, the BESS has changed operation to the discharging mode to full-fill the power mismatch. Accordingly, the BESS discharging 2 kW, as depicted in Fig. 3.22 (b) power to maintain the power balances on the DC bus and bus voltage is operating in the range of  $620 \leq V_{bus} < 634$  V.

Table 3. 4: System Parameter

Source units	Parameters	Values	Units
Wind	Power rated	7	kW
	Sw. frequency	5	kHz
	Rectified DC voltage	400	V
Solar	Power rated	12	kW
	Sw. frequency	5	kHz
	PV Module Voltage	300	V
G-VSC	Power rated	5	kW
	Sw. frequency	5	kHz
	Rectified DC voltage	650	V
BESS	Battery Voltage	240	V
	Sw. frequency	5	kHz
	Power rated	5	kW
Load	Power	2.24 ~18	kW

The battery current is positive when discharging and negative when charging. Depending on the SoC information, the battery converter monitors the discharge and charge status of the battery system and adjusts the current limits accordingly. The bus voltage control sets the static mode according to a predefined algorithm for optimal energy consumption.

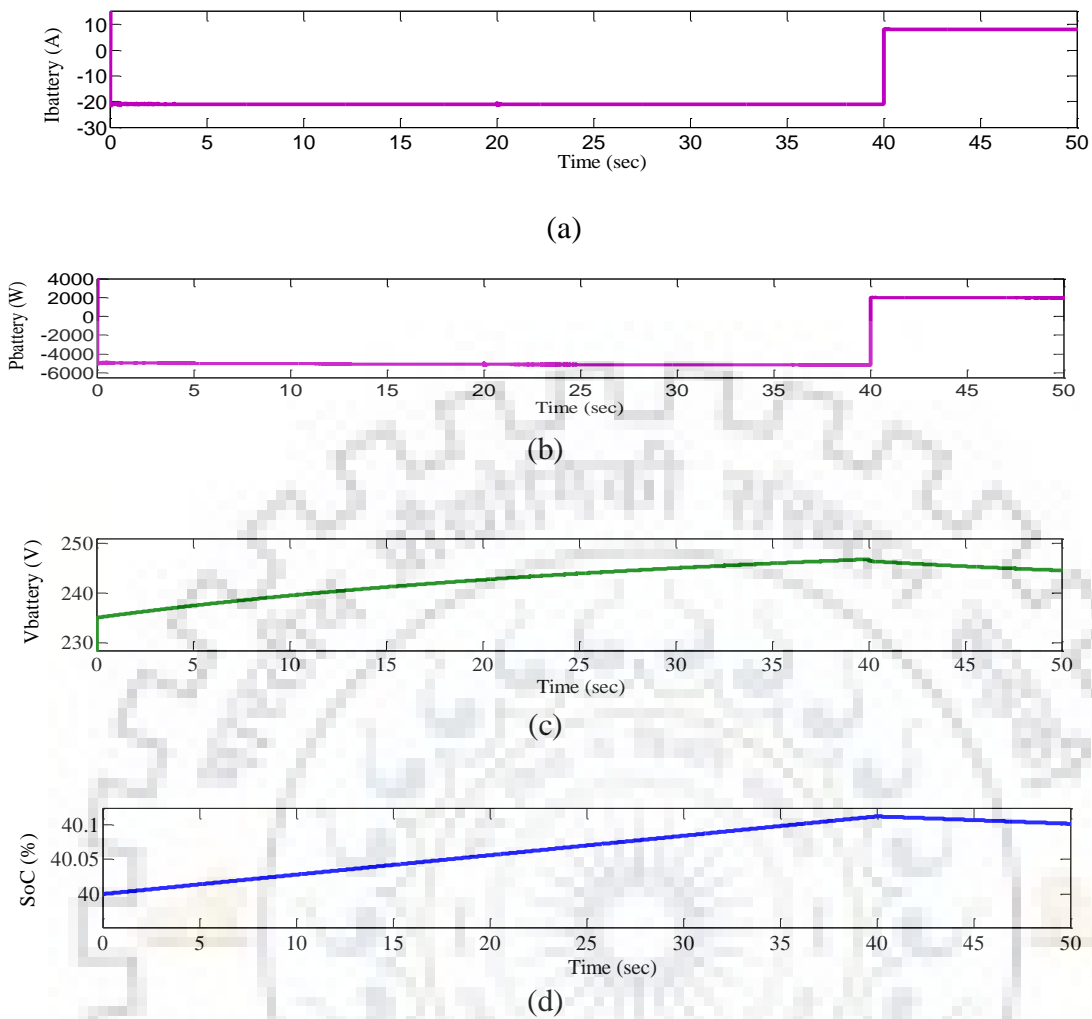


Fig. 3. 22: Battery Real-Time Simulation Results; (a) Current, (b) Power, (c) Voltage, (d) SoC

In DC $\mu$ G, the constant power load commonly controlled through the point of capacity (POL) DC/DC converter or inverter. Besides, the converter controller bandwidth should be sufficiently high to make the load power autonomous from the fluctuation of bus voltage. Hence, in the proposed DC $\mu$ G, the average current mode with a dual PI controller is employed for load converter control to generate a PWM signal for the switching device. The output voltage sensed and compared with the desired voltage. If the error signal is zero, the load voltage accurately follows the desired voltage regardless of the change in input voltage disturbance. Thus, the intended objective is to obtain a constant load voltage irrespective of the input voltage variation. The desired output load voltage is achieved by tuning the voltage controller of POL converters and setting the duty cycle to keep the output voltage constant while the input voltage varies.

The real-time simulation results, as shown in Fig. 3.23 validates the correctness proposed control. In Fig. 3.23 (a) & 3.21(c), despite variation in output load current and input DC voltage, the load output voltage kept constant, as depicted in Fig. 3.23 (e).

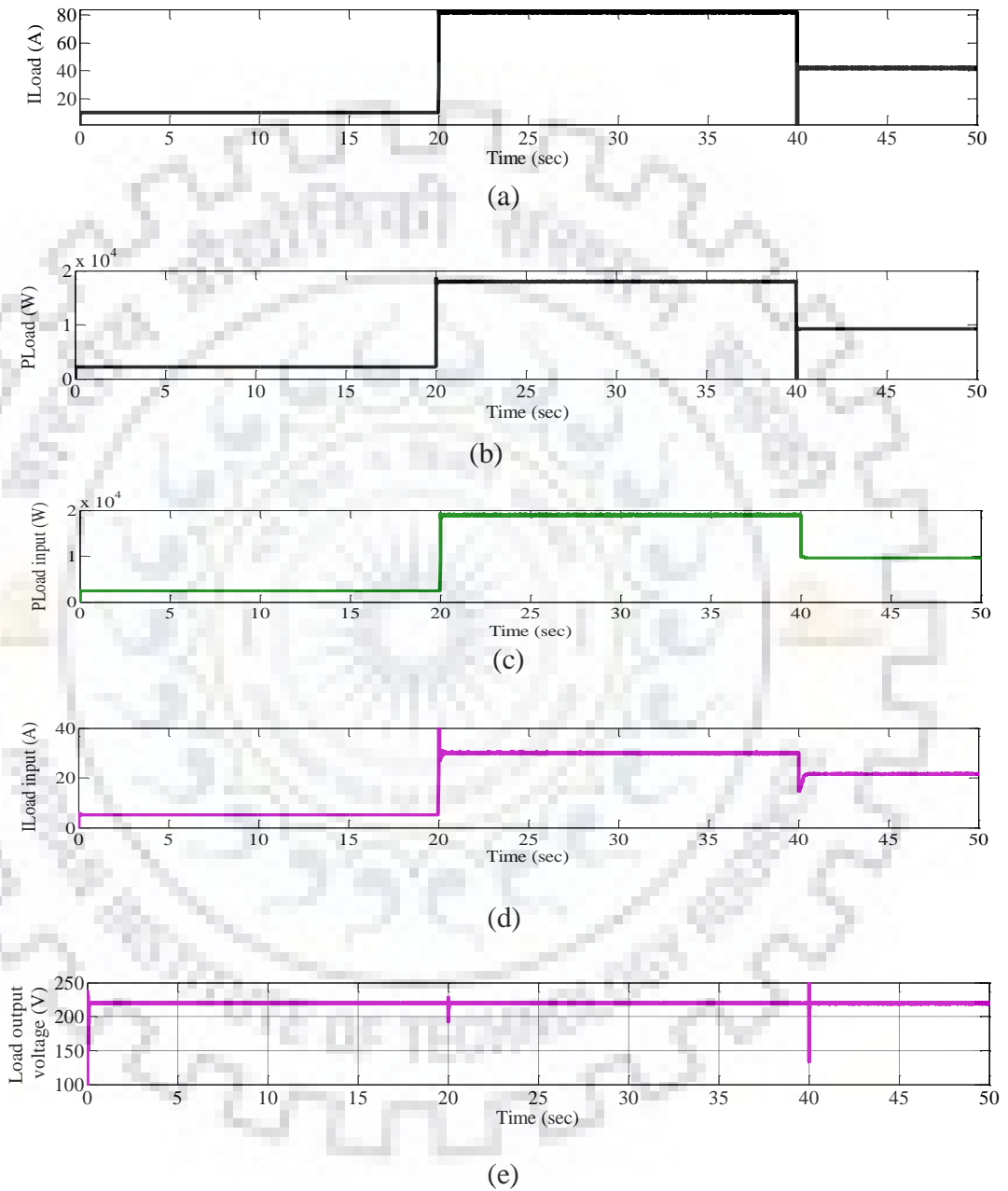


Fig. 3. 23: CPL Real-Time Simulation Results; (a) Output Current, (b) Output Power, (c) Input Power, (d) Input Current, (e) Output Voltage

### 3.9. Summary

DC $\mu$ G with multiple renewable energy sources and energy storage systems is presented in this chapter using the decentralized control structure. The control solution entirely based on the independent control operation of source converter's (as described in chapter two). The bus voltage level used as a communications link to enables various operating modes depending on the generating source capacities. Due to the generation output and sudden load changing impacts, three ways of operations implemented in this chapter to sustain the system reliability and flexible services. The operating mode characteristics of the proposed system are described based on the bus voltage signal that allows smooth mode transitions and reliable load sharing. The proposed DC $\mu$ G model is developed in Matlab/Simulink SimPowerSystems and verified with real-time simulation using OPAL-RT with small modifications. Thus, the work reported in this chapter confirms the usefulness of the suggested DC $\mu$ G control method.



## **CHAPTER 4: STABILITY ANALYSIS OF DC MICROGRIDS WITH CONSTANT POWER LOADS**

In a microgrid, stability defined as the capability of maintaining power supply for the load demand without undesirable changing aspects of power flow and voltage. The DC $\mu$ G stability issues are directly interrelated with the energy conversion system through the interfacing power converters. The DC $\mu$ G has typical interconnected distributed power topologies in which the power converter interconnect between the portions of the policy with various voltages levels. The instability in the system occurs due to the tightly controlled load side converters that act as constant power loads (CPLs). The load side CPL converter small-signal model contains negative input resistance. This negative incremental impedance causes the system poorly damped and can cause unstable poles in the frequency domain and worsen system stability [80]. The factors which challenge the DC $\mu$ G power management system and DC bus voltage stability are the DGs output power fluctuation and continually changes of load power. Thus, the dynamic security of DC $\mu$ G requires managing the power balance of the different components of the DC $\mu$ G system. Since the generation and demand power mismatches typically result in DC bus voltage instability [147], [148], and [75].

The DC $\mu$ G stability can be analyzed broadly with two scales, namely: large and small-signal stability study. The large-signal stability deals with the security of a system that can sustain more significant deviation due to large step changes and faults and have various operating settle point [149]. The large-signal stability analysis does not require linearization of mathematical models, and only non-linear numerical analysis implemented. A Lyapunov-based approach is the most commonly used for large-signal stability analysis [149]. The merit of this method is that it enables the region of attraction estimation for a stable operating point and provides an approximate disturbance size that tolerated.

The small-signal stability issue is related to the deviation of small-signal that can be caused by small local perturbations, controller response mismatches, and system damping. The source controller systems interaction could cause local fluctuations; as a result, it needs to analyze the influence of the deviation in the system. The study of small-signal stability depends on linearizing the non-linear mathematical model at the equilibrium point. The linear stability analysis methods, such as the Nyquist stability criterion, eigenvalue, and sensitivity analysis, use the linearized model for small-signal stability analysis [80].

The stability concerns addressed to enhance the performance of DC $\mu$ G, particularly DC $\mu$ G operating with different voltage ranges. Moreover, proper DC bus voltage control strategies play a vital role in the system with various operating voltage levels to ensure good power quality and stable operation of the DC $\mu$ G [51]. Different techniques reported in the literature to solve stability problems caused by non-linear CPL. An admittance/impedance-based design is proposed in [78]. In [145], stability analysis based on small-signal and attenuation amplification using frequency-dependent virtual impedance for DC $\mu$ G with the presence of CPL proposed. Similarly, in [80], stability improvement using virtual impedance was proposed. In [150], passive damping composed of series resistor-capacitor (RC) that are in parallel with the DC-link capacitance investigated to alleviate the interactions of CPL's negative resistance with input filter. The DC $\mu$ G stability analyzed with linear based on small-signal analysis and non-linear based on large-signal analysis [80], [145]. The intermittent characteristics of DGs and the negative input resistance behaviour of CPLs in DC $\mu$ G with multiple sources are non-linear systems operating with different voltage levels. In this study, passive input filter damping and Nyquist stability analysis used to solve the stability problems. The dynamic filter interaction with the load converter dynamics also eliminated with an optimum damping resistor design.

#### 4.1. Characteristics of CPL Connected to DC Bus

The RES based DC $\mu$ G commonly comprises multiple cascaded parallel connected sources converters to ensure the reliability and flexibility of power supply [151]. Thus it referred to as a multi-converter DC distributed power system [151], [152]. In a converter dominated DC distributed power system, cascading of the interface converter enables to achieve the desired load converter regulation. However, because of the tightly controlled load converter, it acts as a CPL that cause stability problem in the system due to the incremental negative resistance in the small-signal model.

The simple equivalent DC transmission line circuit, as shown in Fig. 4.1. The source converter output voltage is denoted by  $V_s$ , and this voltage supply the load via series inductance, the resistance of DC transmission line and DC bus capacitance  $C$  with a non-linear load that represents as a current source that can be described by  $\frac{P}{V_{bus}}$ , where  $V_{bus}$  represent the DC bus voltage across the capacitor.

At a given operating point, the product of load current and voltage remains constant. The presence of CPL in the system resulted in the occurrence of a nonlinearity term  $\frac{P}{V_{bus}}$  [75]. The current-voltage characteristic curve of the CPL depicted in Fig.4.2.

$$I = \frac{P}{V_{bus}} \quad (4.1)$$

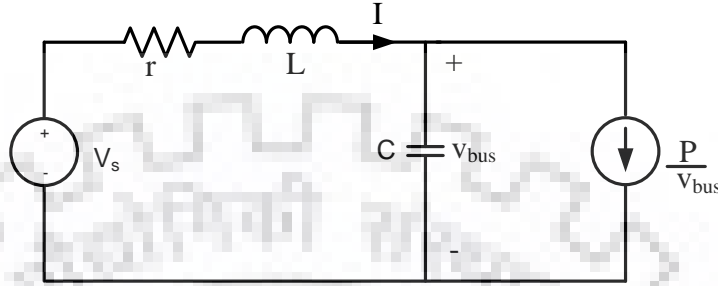


Fig. 4. 1: Simplified DC Microgrid Source Circuit

The derivation of equation (4.1) concerning  $v_{bus}$ , gives the equivalent negative resistance with the given operating point that can be expressed by:

$$\frac{\partial I}{\partial V_{bus}} = -\frac{P}{V_{bus}^2} = -\frac{1}{R_{CPL}} \quad (4.2)$$

From (4.2) it can be realized that  $R_{CPL}$  is depending on the actual bus current and voltage.

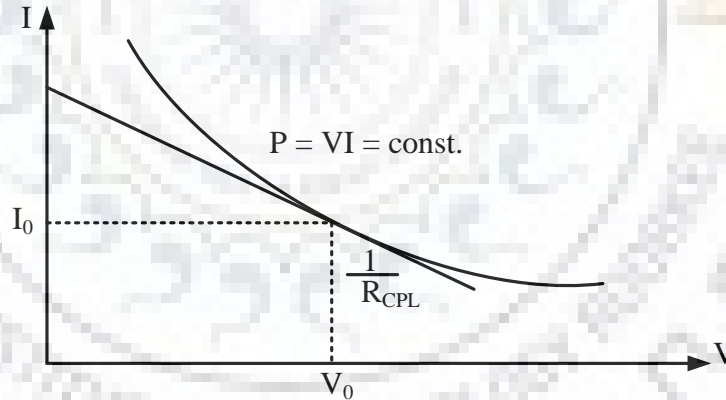


Fig. 4. 2: CPL I – V Characteristic Curve

## 4.2. Causes of DC Microgrid Instability

The DC $\mu$ G control system can choose the various operating modes based on the real condition. In the case of the DG system, the renewable DG sources generate output power with uncertainties due to the change in input environmental conditions. As a result, the DG system operates at either voltage source with droop controlled or MPPT controlled mode to regulate the stability of DC bus voltage [73], [112]. Likewise, the BESS also operate in charging mode (act as CPL) and shift to work with droop control in discharging method and hence regulate bus

voltage in islanded manner. A DC $\mu$ G realized as a group of converters providing power from generating sources into the universal bus, and another cluster of converters is transmitting the energy from the main bus into load subsystems. In this view, since the POL converters adjust the output voltage with higher bandwidth, the dynamics of these converters could be modeled by CPL, whose small-signal analysis contains negative resistance that leads the microgrid stability problem [153], [154].

In actual practice, the load interfacing converter injects a pulsating current into the power stage. This current contains a high order harmonics at multiples of the switching frequency ( $f_{sw}$ ), and this can cause the current spikes due to switching transitions. Moreover, the input source voltage transient also cause conducted audio susceptibilities [155],[156].

### 4.3. Dynamics of POL Converter

In practice, no ideal voltage controller exists. The addition of the input filter at the supply side destabilizes the control feedback system due to the interaction with filter dynamics. Thus, the closed-loop input impedance exact analysis for the load converter is required to examine and quantify the communication between the supply-side and the load subsystem. The POL converter closed-loop input impedance derived from the configuration of load, loop gain, and converter filter of the system control scheme. The input impedance comprises two portions. These are one that dominates the high-frequency part and the other that dominate the low-frequency region. These two regions bind together with loop gain by defining the phase and magnitude responses of the two. The open-loop impedances (4.3) represent the high-frequency portion where the negative resistance (4.4) part corresponds to the low-frequency portion. The impedances expressions described in (4.3) [157].

$$Z_D(s) = \frac{R}{D^2} \frac{(1+s\frac{L}{R}+s^2LC)}{(1+sRC)} \quad (4.3)$$

$$Z_N(s) = -\frac{R}{D^2} \quad (4.4)$$

Where C, L, R, and D are capacitance, inductance, resistance, and duty cycle of the POL converter, respectively. The loop gain calculated by multiplying the feedback path and the transfer functions represented in a forward way. It is derived from the regulated load converter and mathematically expressed as

$$T(s) = H(s)G_{cv}(s)G_{vd}(s) \quad (4.5)$$



Where  $H(s)$  is feedback gain;  $G_{CV}(s)$  voltage compensator; and  $G_{vd}(s)$  the power plant transfer function. The closed-loop input impedance can be derived from (4.3), (4.4) and (4.5) and described by

$$\frac{1}{Z_{in}(s)} = \frac{1}{Z_N(s)} \frac{T(s)}{1+T(s)} + \frac{1}{Z_D(s)} \frac{1}{1+T(s)} \quad (4.6)$$

At low frequencies, the magnitude of the loop gain is high where the input impedance follows the impedance  $Z_N(s)$ . However, the loop-gain decreased at high frequencies where the impedance  $Z_D(s)$  is high.

The stability characteristics of the system interaction investigated by observing the interaction of load converter closed-loop input impedance and the supply output filter impedance. The load converter essentially has independent linearized inputs such as load current  $\hat{i}_{load}$ , supply-side voltage  $\hat{v}_{DC}$  and control input  $\hat{v}_{ref}$ . In the open-loop system, the change in output load voltage derived from the linear combination of those inputs. However, with the closed-loop control system, the control inputs become changing with the system calculated by the controller or compensator from the voltage error.

The variation of output load voltage can be expressed by [157]

$$\hat{v}_{load} = \hat{v}_{ref} \frac{1}{H(s)} \frac{T(s)}{1+T(s)} + \hat{v}_{DC} \frac{G_{vg}(s)}{1+T(s)} - \hat{i}_{load} \frac{Z_{out}(s)}{1+T(s)} \quad (4.7)$$

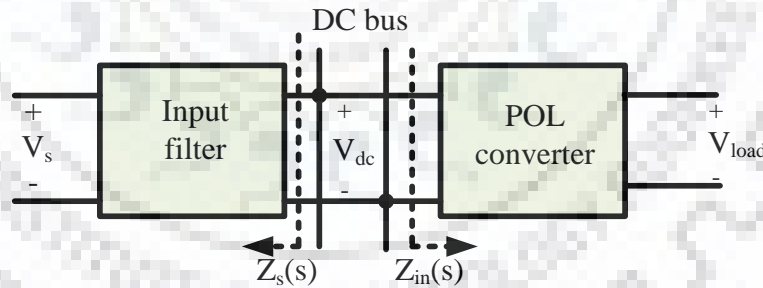


Fig. 4. 3: Load and Source Thevenin Equivalent Circuit Model

The expression in (4.7) experiences certain modifications when the input voltage  $\hat{v}_{DC}$  is provided via the input filter. The transmission line characteristics analyzed with the Thevenin equivalent circuit illustrated in Fig. 4.3. With this view, the relationship between  $\hat{v}_s$  and  $\hat{v}_{DC}$  can be established by employing a voltage divider rule in Fig. 4.3.

$$\hat{v}_{DC} = \frac{Z_{in}(s)}{Z_{in}(s)+Z_s(s)} \hat{v}_s = \frac{1}{1+\frac{Z_s(s)}{Z_{in}(s)}} \hat{v}_s = \frac{1}{1+T_{MLG}(s)} \hat{v}_s \quad (4.8)$$

The stability of the system quantified from the relation  $\frac{Z_s(s)}{Z_{in}(s)}$  or the minor loop gain of the system that can be described by [156], [158]

$$T_{MLG}(s) = \frac{Z_s(s)}{Z_{in}(s)} = \frac{Z_s(s)}{Z_N(s)} \frac{T(s)}{1+T(s)} + \frac{Z_s(s)}{Z_D(s)} \frac{1}{1+T(s)} \quad (4.9)$$

#### 4.4. Input Filter for Stability Improvement

The input filter is applied between power sources and load converters to attenuate disturbances due to switching devices and also limit the conducted electromagnetic interference (EMI). The input filter is required to avoid the ripple currents of the converter switching from being reflected in the source. Also, it prevents the propagation of input voltage disturbances to the load converter [156] [159].

But when a well-designed input filter added at the input of the POL converter, it degrades the converter internal control system. The high peak magnitude of the filter impedance at resonant frequency interacts with the converter control system. Consequently, this results in degradation of the converter open-loop control due to the negative input resistance of the converter interaction with the filter dynamics [157], [160]. The interface between the load converter and input filter output impedance investigated through the open-loop transfer function of the POL converter [161].

Two steps realize the load converter system design. Firstly the converter parameter is designed as per the performance requirement. Secondly, a low-pass input filter that contributes satisfactory attenuation to improve disturbance added to the input POL converter. However, the addition of an input filter degrades dynamic converter performance on the converter control system. Also, it has an impact on the POL converter control to output, line to control, and output impedance transfer functions [157].

##### 1) Effect of Input Filter on Converter Control System

To examine how the input filter alters the dynamic converter performance, buck converter topology, including input filter components and resistive load portrayed in Fig. 4.4.

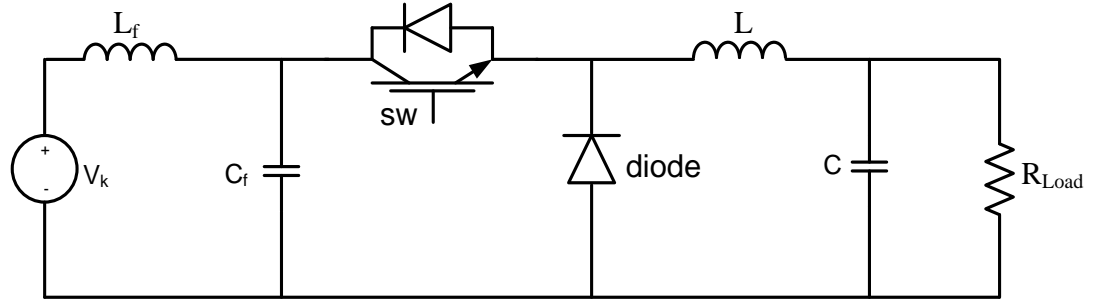


Fig. 4. 4: Load Buck Converter with Damped Input-Filter Circuit Diagram

With the continuous conduction mode operation, the POL converter designed, and voltage mode control employed for the feedback control scheme. The open-loop converter output voltage to duty cycle transfer function is derived using the averaged model of the buck converter and is given by:

$$G_{vd}(s) = \frac{\Delta v}{\Delta d} = V_{in} \frac{a_2 s^2 + a_1 s + a_0}{b_4 s^4 + b_3 s^3 + b_2 s^2 + b_1 s + b_0} \quad (4.10)$$

Where the numerator and denominator coefficients described in the following:

$$a_0 = 1, a_1 = -D^2 L_f / R_L, a_2 = L_f C_f$$

$$b_0 = 1, b_1 = (L + D^2 L_f) / R_L, b_2 = L_f C_f + LC + D^2 L_f C, b_3 = L_f C_f C / R_L, b_4 = L_f C_f LC$$

Note that with the addition of this input filter results in additional resonance mode at the input filters resonant frequency. In the (4.10), the system consists of extra right-half plane zeroes and complex poles due to the interaction with filter dynamics. As a result, this introduces  $-360^\circ$  of phase shift.

#### 4.5. Damping of Input Filter

The stability problem those as mentioned above solved by employing the input filter is damped by connecting the damping resistor in series with a blocking capacitor across the filter capacitor. The circuit topology, which is one of the practical methods of input filter damping, is illustrated in Fig. 4.5.

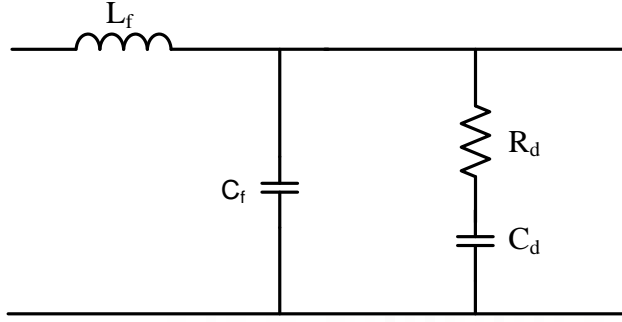


Fig. 4. 5: Input Passive Damping Equivalent Circuit

The damping resistor ( $R_d$ ) in series with the DC blocking capacitor ( $C_d$ ) added to reduce the peak impedance (see Fig. 4.6) at the filter cut-off frequency. The capacitor used to block the current flowing through the damping resistor and prevent power dissipation in the damping resistor. The blocking capacitor should be more significant than the filter capacitor so as not to affect the cut-off point of the primary filter. However, if the bandwidth of the POL converter feedback control is close to or higher than input filter resonant frequency, then the phase margin of the control loop becomes negative, resulting in an unstable system. The optimum passive damping of input filter design, which compromises the stability problem, is added to the filter circuit [157].

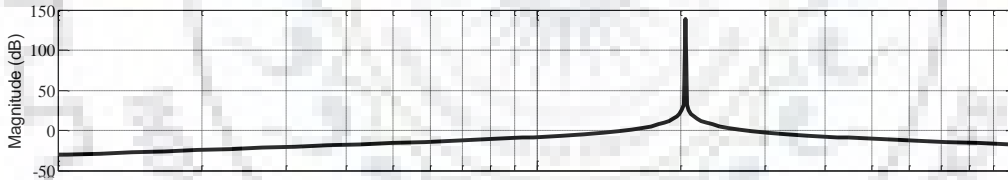


Fig. 4. 6: Magnitude of Input Filter Output Impedance

The optimum value of damping resistance ( $R_d$ ) obtained at the minimum value of filter output impedance ( $Z_o$ ). The combination of the damped input filter with the negative converter input resistance gives positive total resistance. The amount of this damping resistance approximated using the filter peak output impedance as given in (4.11) [155]:

$$|Z_o|_{\max} = R_o \frac{\sqrt{2(2+n)}}{n} \quad (4.11)$$

Where  $R_o = \sqrt{\frac{L_f}{C_f}}$ . The optimum value of  $R_d$  can be estimated by the following expression:

$$R_d(\text{optimum}) = R_o \sqrt{\frac{(2+n)(4+3n)}{2n^2(4+n)}} \quad (4.12)$$

Where  $n = \frac{C_d}{C_f}$ ,  $C_d$  represent the blocking capacitor.

#### 4.6. Stability Analysis Using Nyquist Stability Criteria

The control to output open-loop transfer function ( $G_{vd}(s)$ ) of POL converter with damped input filter expressed as [155]:

$$G_{vd}(s) = V_g \frac{s^3 a_3 + s^2 a_2 + s a_1 + 1}{s^5 b_5 + s^4 b_4 + s^3 b_3 + s^2 b_2 + s b_1 + b_0} \quad (4.13)$$

Where the numerator and denominator coefficients expressed in the following:

$$\begin{aligned} a_0 &= 1, \quad a_1 = nC_f R_d - D^2 L_f / R \\ a_2 &= L_f C_f (1 + n - \frac{nD^2 L_f}{R}), \quad a_3 = nL_f C_f^2 R_d \\ b_0 &= 1, \quad b_1 = nC_f R_d + (L + D^2 L_f) / R \\ b_2 &= C(D^2 L_f + L) + L_f C_f + nL_f C_f + nC_f R_d (L + D^2 L_f) R \\ b_3 &= \frac{L_f C_f L (1+n)}{R} + nC_f R_d (L_f C_f + LC + D^2 L_f C) \\ b_4 &= L_f C_f LC (1 + n) + nL_f L R_d C_f^2 / R \\ b_5 &= nL_f C_f^2 L C R_d \end{aligned}$$

The input filter introduces complex zeroes on the right half-plane leading the system to unstable. Thus, the Routh-Hurwitz criteria used to find the stability conditions that make the system stable from the closed-loop characteristic equation of  $(1 + G_{vd}(s))$ . Accordingly, from the characteristic equation, the following two conditions derived to determine at which the real signs of zero and poles are negative.

$$L_f C_f (1 + n) - \frac{nL_f D^2 R_d}{R} > 0 \quad (4.14)$$

$$\frac{D^2 L_f C_f^2 (1+n)}{R} - nL_f C_f (D^4 L_f + nC_f) R_d + \frac{n^2 D^2 C_f^2}{R} R_d^2 > 0 \quad (4.15)$$

With designed values of  $R_d$  and  $C_d$  where  $C_d = nC_f$ , the stability of the closed-loop is analyzed using the open-loop transfer function  $G_{vd}(s)$ . The filter inductance is designed based on the switching frequency of the converter. In this case, 5kHz switching frequency used. The filter cut-off frequency taken to be a decade below ( $\approx 240\text{Hz}$ ) than voltage control cut-off frequency of regulator and the filter inductance can be estimated by [162]:

$$L_f = \frac{1}{\omega_{cf}^2 C_f} \quad (4.16)$$

Where  $\omega_{cf}$  is the input filter cut-off frequency, ( $\omega_{cf} \approx 1600\text{rad/sec}$ )

Stability of the closed-loop of POL converter investigated from the open-loop transfer function,  $G_{vd}(s)$ . With the inclusion of well-designed input filter with optimum damping parameters the source output impedance ( $Z_o$ ) will become sufficiently smaller than the load converter input impedance. Accordingly, this makes the effect of the input filter on the closed-loop control system becomes negligible, and the converter control works properly with better performance. With a well-damped input filter, the control system performance of the load converter cannot be affected [155].

#### 4.7. Result Discussion

The stability of the system analyzed under source and load variations. Four types of sources are employed to form a DC $\mu$ G in this study. Wind and solar PV sources categorized as DG sources, and they are connected in parallel and interfaced with the primary DC grid through a boost DC-DC converter. BESS is connected to the DC bus via bidirectional buck/boost DC-DC converter, whereas the AC grid coupled through G-VSC to the point of standard coupling (PCC).

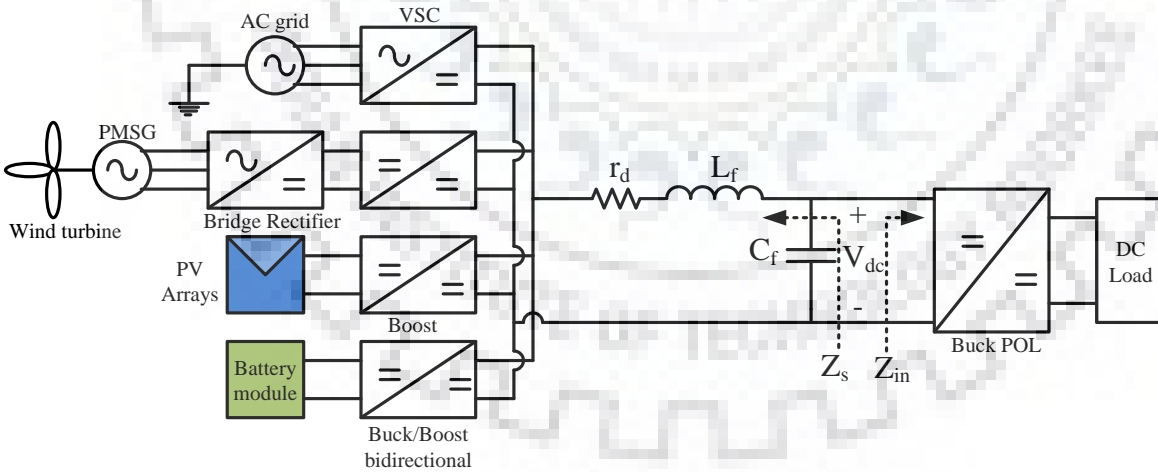


Fig. 4. 7: Equivalent Circuit of Proposed DC $\mu$ G

A single equivalent circuit represents the proposed DC $\mu$ G with the transmission line placed between the loads and the sources, as shown in Fig. 4.7. The system stability examined by observing the load input impedance and source output impedance at the DC bus interface depicted in Fig. 4.7. The converter control loop stability investigated using Nyquist stability

criteria. The frequency responses of the impedances obtained from the small-signal analysis at the DC bus interface point. The dynamic study of load converter control to output transfer function with a damped input filter investigated to mitigate the instability problems with filter dynamics. Fig. 4.8 shows the frequency bode-plot of the open-loop transfer function  $G_{vd}(s)$  of the POL converter without and with input filter. The result, as shown in Fig.4.8 simulated using the filter and POL converter parameters  $L_f = 300\mu\text{H}$ ,  $C_f = 480\mu\text{F}$ ,  $L = 100\mu\text{H}$ ,  $C = 170\mu\text{F}$ ,  $D = 0.48$ ,  $n = 4$ ,  $R_d = 0.84$ ,  $C_d = 1.92\text{mF}$  and  $R = 21.6\Omega$ . The green line shows magnitude and phase response of the undamped input filter while the blue is without the addition of the input filter.

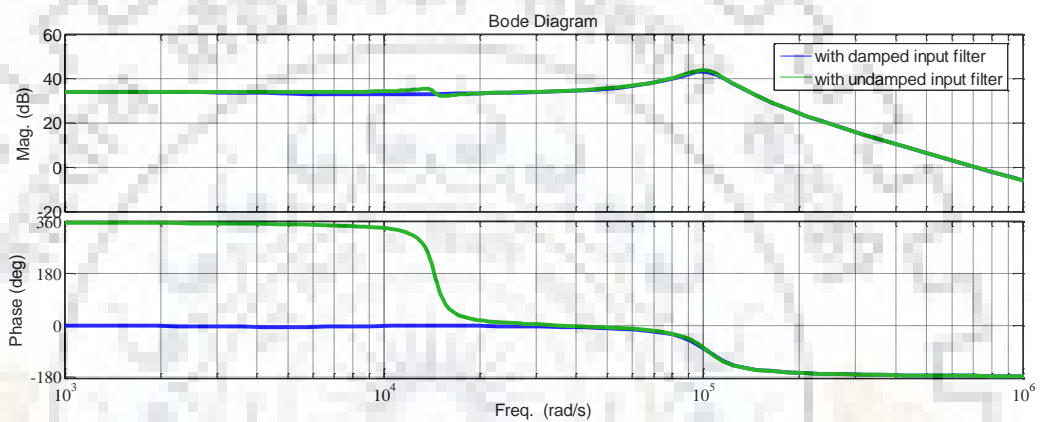


Fig. 4. 8: Bode Plot of Control to Output ( $G_{vd}(s)$ ) Without and With Undamped Input Filter

Without the inclusion of the input filter, the POL converter open-loop control to output voltage transfer function does not have zeros in the right-half plane (see Fig. 4.9), and it regarded as a minimum phase-type. However, with the inclusion of the input filter, a sophisticated conjugate pair of zeroes in the right-half s-plane is introduced, as depicted in Fig. 4.10. Hence, this shows lightly damped, or undamped input filter applied at the input terminal of the POL converter causes instability on the converter control system.

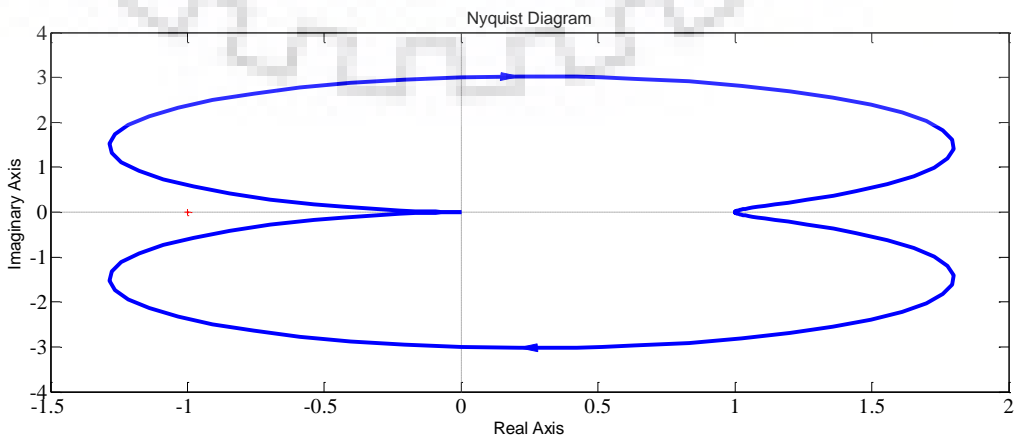




Fig. 4. 9: Nyquist Plot of Control to Output ( $G_{vd}(s)$ ) without Input Filter

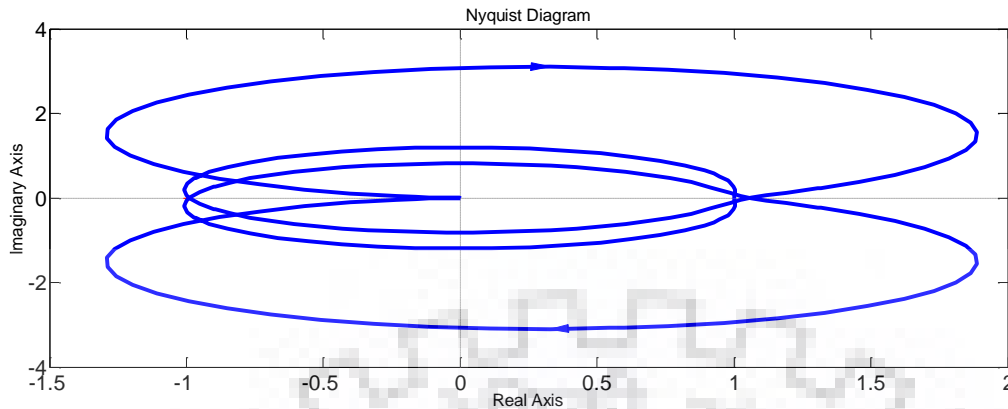


Fig. 4. 10: Nyquist Plot of Control to Output ( $G_{vd}(s)$ ) with Undamped Input Filter

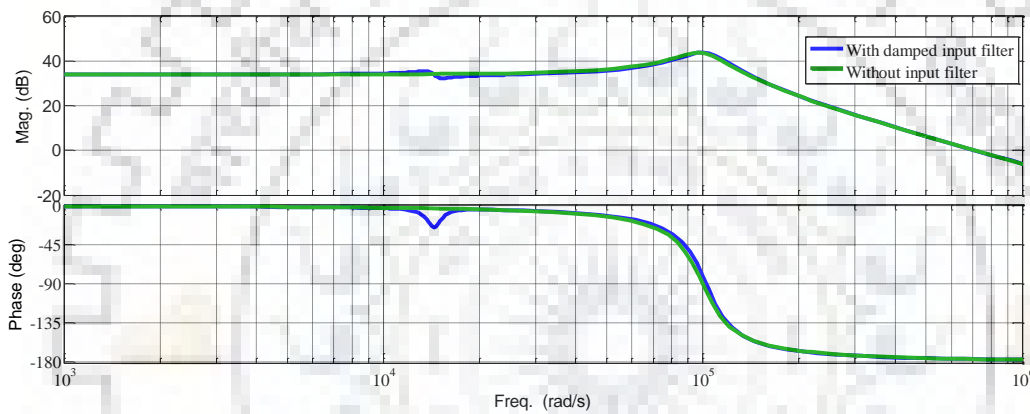


Fig. 4. 11: Bode Plot of  $G_{vd}(s)$  Buck DC / DC Load Converters with and without a Damped input filter

Fig. 4.11 shows the Bode diagram of the converter transfer function without an input filter and with a damped input filter. Initially, the Buck DC/DC converter control for the output transfer function is stable when no input filter added. However, with the addition of a damped input filter, the system is stable. After attenuating the input filter, the result of control to output transfer function is roughly equivalent to that without an input filter, as shown in Fig. 4.12.

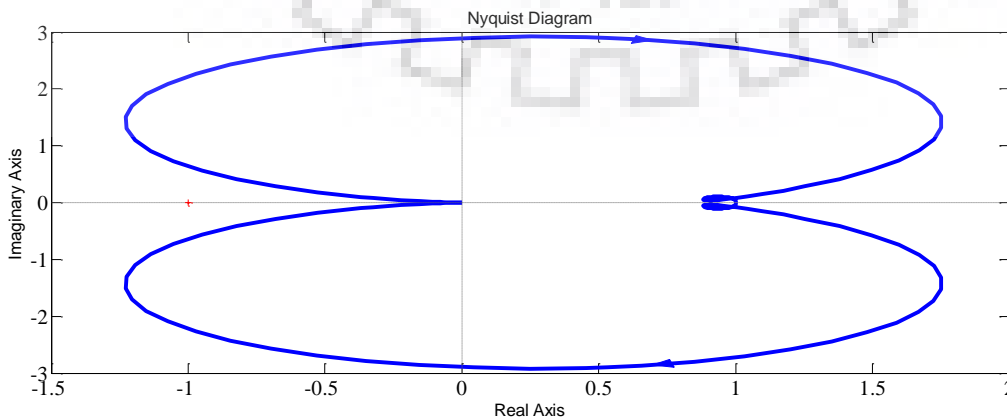


Fig. 4. 12: Nyquist Plot of  $G_{vd}(s)$  Buck DC/DC POL Converter with Damped Input Filter



The instability problem analyzed with the converter control to output voltage transfer functions, and using the Routh-Hurwitz criteria, the stability condition is determined. With optimum damping resistor designed value addition, the system made stable, and using the Nyquist stability criteria, the stability condition is verified. The Nyquist diagram without and with a damped input filter illustrated in Fig. 4.9, and Fig. 4.12, respectively, showing both plots, the results are similar. Thus, this verifies the system is stable.

The impedances bode-plot at the point of standard coupling achieved using the average system model small-signal analysis at 18 kW operating point, as portrayed in Fig. 4.13. The result shows the load input impedance reflects the CPL characteristics at lower frequency ( $\angle Z_L = -180^\circ$ ). The system stability examined by observing the load input impedance ( $Z_S$ ) and source output impedance ( $Z_L$ ) at DC bus connection. The system is stable since the magnitude of  $Z_L$  greater than  $Z_S$  with an appropriate margin, as depicted in Fig. 4.13.

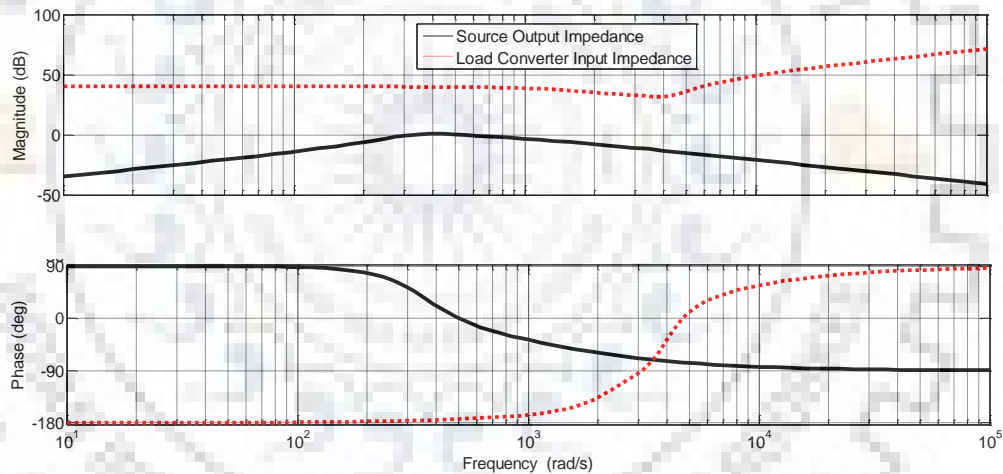


Fig. 4. 13: Converter Input and Source Output Impedance

#### 4.8. Summary

DC  $\mu$ G with multiple sources under various operating bus voltage and CPL is explored in this chapter. The stability problems due to the source and load converter impedance mismatches as well as due to the uncertainties of DGs operation analyzed and method of improvement is proposed. The input filter is employed to mitigate disturbances due to switching devices and avoid electromagnetic interferences. The optimum damping resistance value of the input filter is designed to eliminate instability problems on the POL converter feedback control loop due to

the filter dynamic interactions with sources. The stability condition is verified by using the Nyquist stability criterion.



# CHAPTER 5: CONCLUSION AND FUTURE RESEARCH WORK

## 5.1. Conclusion

Microgrids are an important model for integrating different ESSes and DGs power sources. Initially, the concept of the microgrid is realized as a group of source converters supplying power to the common bus and another group of converters transporting power from the common bus to the load. This made the microgrid appropriate for power generation and fair utilization of small-scale DERs.

In this thesis, multiple source DC microgrids with single bus topology and constant power load is investigated. The sources are controlled autonomously and connected in parallel to the common DC grid through power electronic converters for integrated operations. Combining the DERs to the main DC grid through interfacing power electronic converter provides flexibility in power level and energy conversion system. The DC microgrid operation is performed both in grid-connected and islanded modes with the decentralized scheme under droop control. The droop control is applied to allow the power-sharing to the load and to eliminate the circulating current among the sources. The proposed DC microgrid is implemented in three different operating modes based on the energy dominating source. Namely: DG, G-VSC and BESS modes. The proposed DC $\mu$ G topology with all its components supported with relevant mathematical analysis and independently controlled. The corresponding design is simulated in Matlab/Simulink and the effectiveness of the decentralized droop control scheme at DC $\mu$ G is checked with CPL.

This thesis work begins with the literature surveys on the DC microgrid developments, application, control techniques, power management techniques and stability. There is three main control scheme of DC $\mu$ G have been described. Those control systems are centralized, distributed and decentralized. Reviews on these control strategies, stability improvements and coordinated operation of DC $\mu$ G were investigated. From the literature survey analysis, the research problems, objectives of the research and proposed solutions are presented in chapter 1.

The contributions of the research work have been summarized at the end of each chapter. In addition, the main conclusions of this thesis work are précised in the following.

- Modeling and autonomous control of each DC power source unit have been implemented based on the local control functions such as current, voltage, DGs maximum power control and droop control through the power electronic converters that connect the source units to the common DC grid. The power electronic interface converters employed to maintain the power flow and terminal voltage that facilitate the reliable and efficient operation of the integrated system. Step input source disturbances are applied to the source units. The average current mode controllers are used in all of the modules due to the control scheme presents zero steady-state error.
- In G-VSC the grid phase angle and frequency are regulated by employing advanced lead compensator to compensate for the double frequency content in three-phase supply. The synchronous rotating reference frame transformation also implemented to generate the qd-axis parameters which in turn used for the control of active and reactive power through the inner current controller. The DC voltage control is implemented with the proportional-integral controller via the outer control loop. The high switching harmonic frequency due to converter switching operation is mitigated by employing the LCL filter on the grid-side of the VSC.
- For wind and solar power generation units, MPPT control and voltage mode droop control is implemented to regulate the intermittent power output of wind and solar power generations. At rated conditions, the desired rated value is achieved. However, due to the decrease in input conditions for renewable energy sources, the generation output power also decreased and hence the DGs interfacing converter terminals voltage also decreased. The MPPT control tracks the desired reference voltage to match with the output PV module voltage and rectified DC voltage of the wind turbine with the change in solar radiation and the wind speed, respectively.
- The decentralized control method is proposed for the hybrid source DC microgrid units in order to coordinate the integrated operations and to facilitate suitable load sharing through droop control. The control strategy is implemented using the bus voltage levels as a communication link that enables various operating modes depending on the generating source input conditions. Because of the generation output and sudden load changing impacts, three modes of operations are implemented to sustain the system reliability and flexible operations of the DC microgrid. The proposed DC $\mu$ G model is developed in Matlab/Simulink SimPowerSystems and verified with real-time simulation using RT-LAB in the OPAL-RT simulator.

- The input filter is employed at the input of load converters to mitigate disturbances due to switching devices and limit the electromagnetic interferences. This filter flattens the input current from the supply-side and mitigates the high-frequency changes at the input terminals of the POL converter. In the filter, the resistor in series with the capacitor is connected across the filter capacitor. The damping resistor is used to damp out the peak impedance at the resonant frequency while the blocking capacitor is employed to avoid the power dissipation across the damping resistance. The optimum value of the damping resistance is designed to eliminate the instability problems on the POL converter feedback control loop due to the dynamic filter interactions with sources. The stability condition is verified by using the Nyquist stability criterion using MATLAB/SIMULINK.
- The passive damping input filter used to decouple the load converter and supply system small-signal dynamic interaction. The impedance mismatch of the subsystems is compensated by a suitable selection of the damping resistor. It is demonstrated that source the output impedance is much lower than the input impedance of the load.

## **5.2. The Future Work**

In the modern distribution network, the renewable energy sources penetration and consumers regulated by power electronics is increasing. DC microgrids are suitable for the integration of sustainable energy sources and modern DC electronic loads such as solar PV, ESS, and fuel cells in an efficient way. However, still, further research investigation of DC microgrid required in the following areas.

- A decentralized control scheme that supports plug-and-play operation, and that does not affect the system stability of the multiple source DC microgrid topologies with constant power load requires further investigation.
- The harmonized integration of the multiple sources of the DC microgrid with all protection systems is another foreseen research problem.
- Analysis of DC microgrid under grid disturbance or fault condition and distortion
- Experimental hardware implementation of the integrated multiple sources operations of the DC microgrid.



## BIBLIOGRAPHY

- [1] S. Chowdhury, S. P. Chowdhury, and P. Crossley, *Microgrids and active distribution networks*. 2009.
- [2] H. Kakigano, Y. Miura, and T. Ise, "Low-voltage bipolar-type dc microgrid for super high quality distribution," *IEEE Trans. Power Electron.*, vol. 25, no. 12, pp. 3066–3075, 2010.
- [3] M. Gulin et al., "Control of a DC microgrid," *IEEE Trans. Ind. Electron.*, vol. 4, no. 3, pp. 395–402, 2015.
- [4] M. Kumar, S. C. Srivastava, and S. N. Singh, "Control strategies of a DC microgrid for grid connected and islanded operations," *IEEE Trans. Smart Grid*, vol. 6, no. 4, pp. 1588–1601, 2015.
- [5] R. S. Bhatia, S. P. Jain, D. K. Jain, and B. Singh, "Battery energy storage system for power conditioning of renewable energy sources," *Proc. Int. Conf. Power Electron. Drive Syst.*, vol. 1, pp. 501–506, 2005.
- [6] E. S. Sreeraj, K. Chatterjee, and S. Bandyopadhyay, "Design of isolated renewable hybrid power systems," *Sol. Energy*, vol. 84, no. 7, pp. 1124–1136, 2010.
- [7] P. Bajpai and V. Dash, "Hybrid renewable energy systems for power generation in stand-alone applications: A review," *Renew. Sustain. Energy Rev.*, vol. 16, no. 5, pp. 2926–2939, 2012.
- [8] European Environment Agency, *EEA technical report: Renewable energy in Europe - approximated recent growth and knock-on effects*, no. 1. 2015.
- [9] T. Logenthiran, D. Srinivasan, and D. Wong, "Multi-agent coordination for DER in microgrid," *2008 IEEE Int. Conf. Sustain. Energy Technol. ICSET 2008*, pp. 77–82, 2008.
- [10] T. Ackermann, "Distributed generation : a definition," *Electr. Power Syst. Res.*, vol. 57, pp. 195–204, 2001.
- [11] H. E. Murdock and F. Bariloche, "REN21 is a global multi stakeholder network dedicated to the rapid uptake of renewable energy worldwide .," no. June, 2018.
- [12] S. R. Mohanty, P. K. Ray, N. Kishor, and B. K. Panigrahi, "Classification of disturbances in hybrid DG system using modular PNN and SVM," *Int. J. Electr. Power Energy Syst.*, vol. 44, no. 1, pp. 764–777, 2013.
- [13] R. H. Lasseter, "MicroGrids," in *IEEE Power Engineering Society Winter Meeting*, 2003, pp. 305–308.
- [14] D. Kumar, F. Zare, and A. Ghosh, "DC microgrid technology: system architectures, AC



- grid interfaces, grounding schemes, power quality, communication networks, applications, and standardizations aspects,” *IEEE Access*, vol. 5, pp. 12230–12256, 2017.
- [15] Y. Yoldaş, A. Önen, S. M. Muyeen, A. V. Vasilakos, and İ. Alan, “Enhancing smart grid with microgrids: Challenges and opportunities,” *Renew. Sustain. Energy Rev.*, vol. 72, no. January, pp. 205–214, 2017.
- [16] M. Singh, V. Khadkikar, A. Chandra, and R. K. Varma, “Grid interconnection of renewable energy sources at the distribution level with power-quality improvement features,” *IEEE Trans. Power Deliv.*, vol. 26, no. 1, pp. 307–315, 2011.
- [17] A. K. Rathore, D. R. Patil, and D. Srinivasan, “Non-isolated bidirectional soft-switching current-fed LCL resonant DC/DC Converter to interface energy storage in DC microgrid,” *IEEE Trans. Ind. Appl.*, vol. 52, no. 2, pp. 1711–1722, 2016.
- [18] H. Lotfi and A. Khodaei, “AC versus DC microgrid planning,” *IEEE Trans. Smart Grid*, vol. 8, no. 1, pp. 296–304, 2017.
- [19] P. Sanjeev, N. P. Padhy, and P. Agarwal, “Peak energy management using renewable integrated DC microgrid,” *IEEE Trans. Smart Grid*, vol. 9, no. 5, pp. 4906–4917, 2018.
- [20] Shivam and R. Dahiya, “Distributed control techniques for effective current sharing and voltage regulation in DC distributed systems,” *Electr. Power Components Syst.*, vol. 45, no. 19, pp. 2141–2150, 2017.
- [21] Z. Wang, Z. Chen, and X. Wang, “Research of the DC microgrid topology,” *Proc. 28th Chinese Control Decis. Conf. CCDC 2016*, pp. 2855–2859, 2016.
- [22] D. Wu, F. Tang, T. Dragicevic, J. C. Vasquez, and J. M. Guerrero, “A control architecture to coordinate renewable energy sources and energy storage systems in islanded microgrids,” *IEEE Trans. Smart Grid*, vol. 6, no. 3, pp. 1156–1166, 2015.
- [23] X. Li et al., “Flexible interlinking and coordinated power control of multiple DC microgrids clusters,” *IEEE Trans. Sustain. Energy*, vol. 9, no. 2, pp. 904–915, 2018.
- [24] S. Moayedi and A. Davoudi, “Distributed tertiary control of DC microgrid clusters,” *IEEE Trans. Power Electron.*, vol. 31, no. 2, pp. 1717–1733, 2016.
- [25] L. Meng, T. Dragicevic, J. Roldán-Pérez, J. C. Vasquez, and J. M. Guerrero, “Modeling and sensitivity study of consensus algorithm-based distributed hierarchical control for DC microgrids,” *IEEE Trans. Smart Grid*, vol. 7, no. 3, pp. 1504–1515, 2016.
- [26] S. Moayedi and A. Davoudi, “Cooperative power management in DC microgrid clusters,” *2015 IEEE 1st Int. Conf. Direct Curr. Microgrids, ICDCM 2015*, pp. 75–80, 2015.



- [27] Y. Ito, Y. Zhongqing, and H. Akagi, "Micro-grid based distribution power generation system," 4th Int. Conf. Power Electron. Motion Control IPEMC, pp. 1740–1745, 2004.
- [28] A. Kwasinski and P. T. Krein, "A microgrid-based telecom power system using modular multiple-input DC-DC converters," INTELEC, Int. Telecommun. Energy Conf., pp. 515–520, 2005.
- [29] D. Salomonsson, L. Soder, and A. Sannino, "An adaptive control system for a DC microgrid for data centers," IEEE Trans. Ind. Appl., vol. 44, no. 6, pp. 1910–1917, 2008.
- [30] H. Kakigano, Y. Miura, T. Ise, T. Momose, and H. Hayakawa, "Fundamental characteristics of DC microgrid for residential houses with cogeneration system in each house," IEEE Power Energy Soc. 2008 Gen. Meet. Convers. Deliv. Electr. Energy 21st Century, PES, pp. 1–8, 2008.
- [31] P. Biczel, "Microgrid, power electronic converters for DC," in 5th International Conference Workshop, CPES, 2007.
- [32] H. Kakigano, Y. Miura, T. Ise, and R. Uchida, "DC micro-grid for super high quality distribution - system configuration and control of distributed generations and energy storage devices," PESC Rec. - IEEE Annu. Power Electron. Spec. Conf., pp. 1–7, 2006.
- [33] M. Srinivasan and A. Kwasinski, "Decentralized control of a vehicular microgrid with constant power loads," 2014 IEEE Int. Electr. Veh. Conf. IEVC 2014, pp. 1–8, 2015.
- [34] L. Che and M. Shahidehpour, "DC microgrids: economic operation and enhancement of resilience by hierarchical control," IEEE Trans. Smart Grid, vol. 5, no. 5, pp. 2517–2526, 2014.
- [35] H. Kakigano, Y. Miura, and T. Ise, "Distribution voltage control for DC microgrids using fuzzy control and gain-scheduling technique," IEEE Trans. Power Electron., vol. 28, no. 5, pp. 2246–2258, 2013.
- [36] W. J. Ma, J. Wang, X. Lu, and V. Gupta, "Optimal operation mode selection for a DC microgrid," IEEE Trans. Smart Grid, vol. 7, no. 6, pp. 2624–2632, 2016.
- [37] M. Rodr, G. Stahl, S. Member, and L. Corradini, "Smart DC power management system based on software-configurable power modules," vol. 28, no. 4, pp. 1571–1586, 2013.
- [38] F. Farzan, S. Lahiri, M. Kleinberg, K. Gharieh, F. Farzan, and M. Jafari, "Microgrids for fun and profit: The economics of installation investments and operations," IEEE Power Energy Mag., vol. 11, no. 4, pp. 52–58, 2013.
- [39] A. More and W. P. Wang, "A More resilient grid: The U.S. Department of Energy Joins with Stakeholders in an R&D Plan," IEEE Power Energy Mag., vol. 13, no. April, pp. 26–34, 2015.

- [40] R. H. Lasseter and P. Paigi, "Microgrid: A conceptual solution," *PESC Rec. - IEEE Annu. Power Electron. Spec. Conf.*, vol. 6, no. June, pp. 4285–4290, 2004.
- [41] A. Arulampalam, M. Barnes, A. Engler, A. Goodwin, and N. Jenkins, "Control of power electronic interfaces in distributed generation Microgrids," *Int. J. Electron.*, vol. 91, no. 9, pp. 503–523, 2004.
- [42] F. Blaabjerg, Z. Chen, and S. B. Kjaer, "Power electronics as efficient interface in dispersed power generation systems," *IEEE Trans. Power Electron.*, vol. 19, no. 5, pp. 1184–1194, 2004.
- [43] R. Geometry and G. Analysis, "Power Electronics and its application in Renewable Energy Japan," *IEEE Circuits Syst. Mag.*, vol. 8, no. 5, pp. 52–66, 2008.
- [44] B. T. Patterson, "DC come home: DC microgrids and the birth of the 'enernet,'" *IEEE Power Energy Mag.*, vol. 10, no. 6, pp. 60–69, 2012.
- [45] C. L. Chen, Y. Wang, J. S. Lai, Y. S. Lee, and D. Martin, "Design of parallel inverters for smooth mode transfer microgrid applications," *IEEE Trans. Power Electron.*, vol. 25, no. 1, pp. 6–15, 2010.
- [46] S. J. Ahn, J. W. Park, I. Y. Chung, S. Il Moon, S. H. Kang, and S. R. Nam, "Power-sharing method of multiple distributed generators considering control modes and configurations of a microgrid," *IEEE Trans. Power Deliv.*, vol. 25, no. 3, pp. 2007–2016, 2010.
- [47] A. Mehrizi-Sani and R. Iravani, "Potential-function based control of a microgrid in islanded and grid-connected modes," *IEEE Trans. Power Syst.*, vol. 25, no. 4, pp. 1883–1891, 2010.
- [48] C. Cho, J. H. Jeon, J. Y. Kim, S. Kwon, K. Park, and S. Kim, "Active synchronizing control of a microgrid," *IEEE Trans. Power Electron.*, vol. 26, no. 12, pp. 3707–3719, 2011.
- [49] Y. Guan, P. Paigi, and M. R. Iravani, "Micro-grid autonomous operation during and subsequent to islanding process," *IEEE Trans. Power Deliv.*, vol. 20, no. 1, pp. 248–257, 2005.
- [50] D. Chen, L. Xu, and L. Yao, "DC voltage variation based autonomous control of DC microgrids," *IEEE Trans. Power Deliv.*, vol. 28, no. 2, pp. 637–648, 2013.
- [51] N. Zhi, H. Zhang, and X. Xiao, "Switching system stability analysis of DC microgrids with DBS control," *Conf. Proc. - IEEE Appl. Power Electron. Conf. Expo. - APEC*, vol. 2016-May, pp. 3338–3345, 2016.
- [52] W. Panbao, W. Wei, X. Dianguo, L. Guihua, and L. Ming, "An autonomous control

- scheme for DC micro-grid system,” *IECON Proc. (Industrial Electron. Conf.)*, pp. 1519–1523, 2013.
- [53] G. Feng, Z. Zhao, L. Yuan, K. Li, and X. Weng, “Coordinated control of DC voltage in the DC microgrid based on energy router,” {...} *Electrical Mach.*, 2016.
- [54] M. Kowsalya, A. Thamilmaran, and P. Vijayapriya, “Supervisor control for a stand-alone hybrid generation system,” *Int. J. Appl. Eng. Res.*, vol. 12, no. 14, pp. 4090–4097, 2017.
- [55] F. Valenciaga and P. F. Puleston, “High-order sliding control for a wind energy conversion system based on a permanent magnet synchronous generator,” *IEEE Trans. Energy Convers.*, vol. 23, no. 3, pp. 860–867, 2008.
- [56] Q. Shafiee, T. Dragičević, J. C. Vasquez, and J. M. Guerrero, “Hierarchical control for multiple DC-microgrids clusters,” *IEEE Trans. Energy Convers.*, vol. 29, no. 4, pp. 922–933, 2014.
- [57] K. De Brabandere, K. Vanthournout, J. Driesen, G. Deconinck, and R. Belmans, “Control of microgrids,” 2007 *IEEE Power Eng. Soc. Gen. Meet. PES*, pp. 1–7, 2007.
- [58] X. Lu, J. M. Guerrero, K. Sun, J. C. Vasquez, R. Teodorescu, and L. Huang, “Hierarchical control of parallel AC-DC converter interfaces for hybrid microgrids,” *IEEE Trans. Smart Grid*, vol. 5, no. 2, pp. 683–692, 2014.
- [59] T. Dragicevic, J. M. Guerrero, J. C. Vasquez, and D. Skrlec, “Supervisory control of an adaptive-droop regulated DC microgrid with battery management capability,” *IEEE Trans. Power Electron.*, vol. 29, no. 2, pp. 695–706, 2014.
- [60] C. Jin, P. Wang, J. Xiao, Y. Tang, and F. H. Choo, “Implementation of hierarchical control in DC microgrids,” *IEEE Trans. Ind. Electron.*, vol. 61, no. 8, pp. 4032–4042, 2014.
- [61] P. García, P. Arbolea, B. Mohamed, A. A. C. Vega, and M. C. Vega, “Implementation of a hybrid distributed/centralized real-time monitoring system for a DC/AC microgrid with energy storage capabilities,” *IEEE Trans. Ind. Informatics*, vol. 12, no. 5, pp. 1900–1909, 2016.
- [62] I. Federico, E. Jose, and F. Luis, “Master–slave DC droop control for paralleling auxiliary DC/DC converters in electric bus applications,” *IET Power Electron.*, vol. 10, no. 10, pp. 1156–1164, 2017.
- [63] S. Anand, B. G. Fernandes, and J. M. Guerrero, “Distributed control to ensure proportional load sharing and improve voltage regulation in low-voltage DC microgrids,” *IEEE Trans. Power Electron.*, vol. 28, no. 4, pp. 1900–1913, 2013.

- [64] X. Lu, J. M. Guerrero, K. Sun, and J. C. Vasquez, "An improved droop control method for dc microgrids based on low bandwidth communication with dc bus voltage restoration and enhanced current sharing accuracy," *IEEE Trans. Power Electron.*, vol. 29, no. 4, pp. 1800–1812, 2014.
- [65] P. Wang, X. Lu, X. Yang, W. Wang, and D. Xu, "An improved distributed secondary control method for DC microgrids with enhanced dynamic current sharing performance," *IEEE Trans. Power Electron.*, vol. 31, no. 9, pp. 6658–6673, 2016.
- [66] V. Nasirian, S. Moayedi, A. Davoudi, and F. L. Lewis, "Distributed cooperative control of dc microgrids," *IEEE Trans. Power Electron.*, vol. 30, no. 4, pp. 2288–2303, 2015.
- [67] L. Meng, T. Dragicevic, J. M. Guerrero, and J. C. Vasquez, "Dynamic consensus algorithm based distributed global efficiency optimization of a droop controlled DC microgrid," *ENERGYCON 2014 - IEEE Int. Energy Conf.*, pp. 1276–1283, 2014.
- [68] A. Tani, M. B. Camara, and B. Dakyo, "Energy management in the decentralized generation systems based on renewable energy - ultracapacitors and battery to compensate the wind/load power fluctuations," *IEEE Trans. Ind. Appl.*, vol. 51, no. 2, pp. 1817–1827, 2015.
- [69] J. Bryan, R. Duke, and S. Round, "Decentralized generator scheduling in a nanogrid using DC bus signaling," *IEEE Power Eng. Soc. Gen. Meet. 2004.*, pp. 977–982, 2005.
- [70] S. Peyghami, H. Mokhtari, and F. Blaabjerg, "Decentralized load sharing in an LVDC microgrid with an adaptive droop approach based on a superimposed frequency," *IEEE J. Emerg. Sel. Top. Power Electron.*, vol. 5, no. 3, pp. 1–1, 2017.
- [71] J. Peng, B. Fan, J. Duan, Q. Yang, and W. Liu, "Adaptive decentralized output-constrained control of single-bus DC microgrids," *IEEE/CAA J. Autom. Sin.*, vol. 6, no. 2, pp. 424–432, 2019.
- [72] Y. Gu, X. Xiang, W. Li, and X. He, "Mode-adaptive decentralized control for renewable DC microgrid with enhanced reliability and flexibility," *IEEE Trans. Power Electron.*, vol. 29, no. 9, pp. 5072–5080, 2014.
- [73] X. Zhang, X. Ruan, and C. K. Tse, "Impedance-based local stability criterion for DC distributed power systems," *IEEE Trans. Circuits Syst. I Regul. Pap.*, vol. 62, no. 3, pp. 916–925, 2015.
- [74] A. Kwasinski and C. N. Onwuchekwa, "Dynamic behavior and stabilization of DC microgrids with instantaneous constant-power loads," *IEEE Trans. Power Electron.*, vol. 26, no. 3, pp. 822–834, 2011.
- [75] T. Dragicevic, X. Lu, J. C. Vasquez, and J. M. Guerrero, "DC Microgrids - part I: a

- review of control strategies and stabilization techniques,” *IEEE Trans. Power Electron.*, vol. 31, no. 7, pp. 4876–4891, 2016.
- [76] L. Guo, S. Zhang, X. Li, Y. W. Li, C. Wang, and Y. Feng, “Stability analysis and damping enhancement Based on frequency-dependent virtual impedance for DC microgrids,” *IEEE J. Emerg. Sel. Top. Power Electron.*, vol. 5, no. 1, pp. 338–350, 2017.
- [77] J. M. Guerrero, J. C. Vasquez, J. Matas, L. G. De Vicuña, and M. Castilla, “Hierarchical control of droop-controlled AC and DC microgrids - A general approach toward standardization,” *IEEE Trans. Ind. Electron.*, vol. 58, no. 1, pp. 158–172, 2011.
- [78] S. D. Sudhoff and S. F. Glover, “Admittance space stability analysis of power electronic systems,” *IEEE Trans. Aerosp. Electron. Syst.*, vol. 36, no. 3 PART 1, pp. 965–973, 2000.
- [79] P. Karlsson and J. Svensson, “DC bus voltage control for a distributed power system,” *IEEE Trans. Power Electron.*, vol. 18, no. 6, pp. 1405–1412, 2003.
- [80] X. Lu, K. Sun, J. M. Guerrero, J. C. Vasquez, L. Huang, and J. Wang, “Stability enhancement based on virtual impedance for DC microgrids with constant power loads,” *IEEE Trans. Smart Grid*, vol. 6, no. 6, pp. 2770–2783, 2015.
- [81] S. H. Ryu, J. H. Ahn, B. K. Lee, and K. S. Cho, “Single-switch ZVZCS quasi-resonant CLL isolated DC-DC converter for low-power 32 LCD TV,” 2013 *IEEE Energy Convers. Congr. Expo. ECCE 2013*, pp. 4887–4893, 2013.
- [82] K. Techakittiroj and V. Wongpaibool, “Co-existence between AC-distribution and DC-distribution: In the view of appliances,” 2009 *Int. Conf. Comput. Electr. Eng. ICCEE 2009*, vol. 1, pp. 421–425, 2009.
- [83] X. Yu, M. R. Starke, L. M. Tolbert, and B. Ozpineci, “Special family of PWM-based sliding-mode voltage controllers for basic DC–DC converters in discontinuous conduction mod,” *IET Electr. Power Appl.*, vol. 1, no. 1, pp. 643–656, 2007.
- [84] M. Amin, Y. Arafat, S. Lundberg, and S. Mangold, “Low voltage DC distribution system compared with 230 V AC,” 2011 *IEEE Electr. Power Energy Conf. EPEC 2011*, pp. 340–345, 2011.
- [85] M. H. Ryu, H. S. Kim, J. H. Kim, J. W. Baek, and J. H. Jung, “Test bed implementation of 380V DC distribution system using isolated bidirectional power converters,” 2013 *IEEE Energy Convers. Congr. Expo. ECCE 2013*, pp. 2948–2954, 2013.
- [86] B. A. Thomas, “Edison revisited: Impact of DC distribution on the cost of LED lighting and distributed generation,” *Conf. Proc. - IEEE Appl. Power Electron. Conf. Expo. - APEC*, pp. 588–593, 2010.



- [87] W. Yu, J. S. Lai, H. Ma, and C. Zheng, "High-efficiency dc-dc converter with twin bus for dimmable LED lighting," *IEEE Trans. Power Electron.*, vol. 26, no. 8, pp. 2095–2100, 2011.
- [88] G. C. Lazaroiu and D. Zaninelli, "A control system for dc arc furnaces for power quality improvements," *Electr. Power Syst. Res.*, vol. 80, no. 12, pp. 1498–1505, 2010.
- [89] G. F. Reed, "DC technologies: Solutions to electric power system advancements," *IEEE Power Energy Mag.*, vol. 10, no. 6, pp. 10–17, 2012.
- [90] T. F. Wu, C. H. Chang, L. C. Lin, G. R. Yu, and Y. R. Chang, "DC-bus voltage control with a three-phase bidirectional inverter for DC distribution systems," *IEEE Trans. Power Electron.*, vol. 28, no. 4, pp. 1890–1899, 2013.
- [91] D. Salomonsson and A. Sannino, "Low-voltage DC distribution system for commercial power systems with sensitive electronic loads," *IEEE Trans. Power Deliv.*, vol. 22, no. 3, pp. 1620–1627, 2007.
- [92] M. A. Redfern, "Smart DC micro-grids," *Proc. 2014 15th Int. Sci. Conf. Electr. Power Eng. EPE 2014*, pp. 173–178, 2014.
- [93] M. Fantauzzi, D. Iannuzzi, M. Pagano, A. Scalfati, and M. Roscia, "Building DC microgrids: Planning of an experimental platform with power hardware in the loop features," *2015 Int. Conf. Renew. Energy Res. Appl. ICRERA 2015*, vol. 5, pp. 1507–1512, 2015.
- [94] J. M. Carrasco et al., "Power-electronic systems for the grid integration of renewable energy sources: a survey," *Ieee Trans. Ind. Electron.*, vol. 53, no. 4, pp. 1002–1016, 2006.
- [95] M. P. Kazmierkowski and L. Malesani, "Current control techniques for three-phase voltage-source pwm converters: A survey," *IEEE Trans. Ind. Electron.*, vol. 45, no. 5, pp. 691–703, 1998.
- [96] Bose Bimal K., "Modern power electronics and AC drives -Prentice Hall PTR (2002).pdf." 2001.
- [97] R. I. Amirnaser Yazdani, *Voltage-sourced converters in power systems modeling, control and applications*. 2010.
- [98] E. Twining and D. G. Holmes, "Grid current regulation of a three-phase voltage source inverter with an LCL input filter," *IEEE Trans. Power Electron.*, vol. 18, no. 3, pp. 888–895, 2003.
- [99] Y. Tong, F. Tang, Y. Chen, F. Zhou, and X. Jin, "Design algorithm of grid-side LCL-filter for three-phase voltage source PWM rectifier," *IEEE Power Energy Soc.* 2008

- Gen. Meet. Convers. Deliv. Electr. Energy 21st Century, PES, pp. 1–6, 2008.
- [100] M. Liserre, F. Blaabjerg, and S. Hansen, “Design and control of an LCL-filter-based three-phase active rectifier,” *IEEE Trans. Ind. Appl.*, vol. 41, no. 5, pp. 1281–1291, 2005.
- [101] A. Reznik, M. G. Simões, A. Al-Durra, and S. M. Muyeen, “LCL filter design and performance analysis for small wind turbine systems,” *PEMWA 2012 - 2012 IEEE Power Electron. Mach. Wind Appl.*, pp. 1–7, 2012.
- [102] J. S. S. Prasad, T. Bhavsar, R. Ghosh, and G. Narayanan, “Vector control of three-phase AC / DC front-end converter,” *Sadhana*, vol. 33, no. October, pp. 591–613, 2008.
- [103] V. Kaura, VikramBlasko, “Operation of phase locked loop system under distorted utility grid,” *IEEE Trans. Ind. Appl.*, vol. 33, no. 1, pp. 58–63, 1997.
- [104] S. K. Chung, “A phase tracking system for three phase utility interface inverters,” *IEEE Trans. Power Electron.*, vol. 15, no. 3, pp. 431–438, 2000.
- [105] D. Jovcic and P. D. Baulcombe, “Instantaneous power theory and applications to power conditioning,” *CEUR Workshop Proc.*, vol. 1542, no. 3, pp. 33–36, 2011.
- [106] F. D. Freijedo, A. G. Yepes, Ó. López, A. Vidal, and J. Doval-Gandoy, “Three-phase PLLs with fast postfault retracking and steady-state rejection of voltage unbalance and harmonics by means of lead compensation,” *IEEE Trans. Power Electron.*, vol. 26, no. 1, pp. 85–97, 2011.
- [107] C. Wang, X. Li, L. Guo, and Y. W. Li, “A nonlinear-disturbance-observer-based DC-bus voltage control for a hybrid AC/DC microgrid,” *IEEE Trans. Power Electron.*, vol. 29, no. 11, pp. 6162–6177, 2014.
- [108] G. Joós, “Performance investigation of a current-controlled voltage-regulated PWM rectifier in rotating and stationary frames,” *IEEE Trans. Ind. Electron.*, vol. 42, no. 4, pp. 396–401, 1995.
- [109] M. Bojrup, *Advanced control of active filters in a battery charger application*. 1999.
- [110] L. Wang, *Modeling and control of sustainable power systems*. 2012.
- [111] N. Eghtedarpour and E. Farjah, “Control strategy for distributed integration of photovoltaic and energy storage systems in DC micro-grids,” *Renew. Energy*, vol. 45, pp. 96–110, 2012.
- [112] M. Beykverdi, A. Jalilvand, and M. Ehsan, “Decentralized control of low-voltage islanded DC microgrid using power management strategies,” *Am. J. Sci. Eng. Technol.*, vol. 1, no. 2, pp. 27–41, 2017.
- [113] V. Yaramasu, B. Wu, P. C. Sen, S. Kouro, and M. Narimani, “High-power wind energy

- conversion systems: State-of-the-art and emerging technologies,” *Proc. IEEE*, vol. 103, no. 5, pp. 740–788, 2015.
- [114] V. Agarwal, R. K. Aggarwal, P. Patidar, and C. Patki, “A novel scheme for rapid tracking of maximum power point in wind energy generation systems,” *IEEE Trans. Energy Convers.*, vol. 25, no. 1, pp. 228–236, 2010.
- [115] J. G. Sloomweg, H. Polinder, and W. L. Kling, “Representing wind turbine electrical generating systems in fundamental frequency simulations,” *Ieee Trans. Energy Conversion*, Vol. 18, No. 4, December 2003, vol. 18, no. 4, pp. 516–524, 2003.
- [116] K. Tan and S. Islam, “Optimum control strategies in energy conversion of PMSG wind turbine system without mechanical sensors,” *IEEE Trans. Energy Convers.*, vol. 19, no. 2, pp. 392–399, 2004.
- [117] M. Kumar, S. C. Srivastava, S. N. Singh, and M. Ramamoorthy, “Development of a control strategy for interconnection of islanded direct current microgrids,” *IET Renew. Power Gener.*, vol. 9, no. 3, pp. 284–296, 2015.
- [118] and S. K. Wu, Bin, Yongqiang Lang, Navid Zargari, *Power conversion and control of wind energy systems*. John Wiley & Sons, 2011.
- [119] M. A. Elgendy, B. Zahawi, and D. J. Atkinson, “Assessment of perturb and observe MPPT algorithm implementation techniques for PV pumping applications,” *IEEE Trans. Sustain. Energy*, vol. 3, no. 1, pp. 21–33, 2012.
- [120] J. Schönberger, R. Duke, and S. D. Round, “DC-bus signaling: A distributed control strategy for a hybrid renewable nanogrid,” *IEEE Trans. Ind. Electron.*, vol. 53, no. 5, pp. 1453–1460, 2006.
- [121] Z. Shuai, S. Mo, J. Wang, Z. J. Shen, W. Tian, and Y. Feng, “Droop control method for load share and voltage regulation in high-voltage microgrids,” *J. Mod. Power Syst. Clean Energy*, vol. 4, no. 1, pp. 76–86, 2016.
- [122] M. G. Villalva, T. G. De Siqueira, and E. Ruppert, “Voltage regulation of photovoltaic arrays: small-signal analysis and control design,” *IET Power Electron.*, vol. 3, no. 6, pp. 869–880, 2010.
- [123] G. M. Masters, *Renewable and efficient electric power systems*, vol. 42, no. 06. 2005.
- [124] and A.-I. D. Tremblay, Olivier, Louis-A. Dessaint, “A generic battery model for the dynamic simulation of hybrid electric vehicles,” in *In 2007 IEEE Vehicle Power and Propulsion Conference*, 2007, no. V, pp. 284–289.
- [125] K. Sun, L. Zhang, Y. Xing, and J. M. Guerrero, “A distributed control strategy based on DC bus signaling for modular photovoltaic generation systems with battery energy



- storage,” *IEEE Trans. Power Electron.*, vol. 26, no. 10, pp. 3032–3045, 2011.
- [126] K. A. Jadav, H. M. Karkar, and I. N. Trivedi, “A review of microgrid architectures and control strategy,” *J. Inst. Eng. Ser. B*, vol. 98, no. 6, pp. 591–598, 2017.
- [127] T. Dragičević, X. Lu, J. C. Vasquez, and J. M. Guerrero, “DC Microgrids - part II: a review of power architectures, applications, and standardization issues,” *IEEE Trans. Power Electron.*, vol. 31, no. 5, pp. 3528–3549, 2016.
- [128] J. Meng, Y. Wang, C. Wang, and H. Wang, “Design and implementation of hardware-in-the-loop simulation system for testing control and operation of DC microgrid with multiple distributed generation units,” *IET Gener. Transm. Distrib.*, vol. 11, no. 12, pp. 3065–3072, 2017.
- [129] G. Feng, Z. Zhao, L. Yuan, K. Li, and X. Weng, “Coordinated control of DC voltage in the DC microgrid based on energy router,” *19th Int. Conf. Electr. Mach. Syst. ICEMS 2016*, 2017.
- [130] R. Johnson, B.K. and Lasseter, “An industrial power distribution system featuring UPS properties,” in *IEEE IEEE Power Electronics Specialist*, 1993, pp. 759–765.
- [131] R. Mistry, K., Silverman, E., Taylor, T. and Willis, “Telecommunications power architectures: distributed or centralized,” in *IEEE Eleventh International Telecommunications Energy Conference*, 1989, pp. 1–11.
- [132] D. Boroyevich, I. Cvetković, D. Dong, R. Burgos, F. Wang, and F. Lee, “Future electronic power distribution systems - A contemplative view,” *Proc. Int. Conf. Optim. Electr. Electron. Equipment, OPTIM*, pp. 1369–1380, 2010.
- [133] and H. A. Ito, Youichi, Yang Zhongqing, “DC microgrid based distribution power generation system,” in *In The 4th International Power Electronics and Motion Control Conference*, 2004, pp. 1740–1745.
- [134] D. Chen and L. Xu, “Autonomous DC voltage control of a DC microgrid with multiple slack terminals,” *IEEE Trans. Power Syst.*, vol. 27, no. 4, pp. 1897–1905, 2012.
- [135] Q. Xu et al., “A decentralized dynamic power sharing strategy for hybrid energy storage system in autonomous DC microgrid,” *IEEE Trans. Ind. Electron.*, vol. 64, no. 7, pp. 5930–5941, 2017.
- [136] S. Peyghami, H. Mokhtari, and F. Blaabjerg, “Decentralized Load Sharing in a Low-Voltage Direct Current Microgrid with an Adaptive Droop Approach Based on a Superimposed Frequency,” *IEEE J. Emerg. Sel. Top. Power Electron.*, vol. 5, no. 3, pp. 1205–1215, 2017.
- [137] L. Che, M. Shahidehpour, A. Alabdulwahab, and Y. Al-Turki, “Hierarchical

- coordination of a community microgrid with AC and DC microgrids,” *IEEE Trans. Smart Grid*, vol. 6, no. 6, pp. 3042–3051, 2015.
- [138] H. Wang, Y. Chen, Y. F. Liu, J. Afsharian, and Z. Yang, “A passive current sharing method with common inductor multiphase LLC resonant converter,” *IEEE Trans. Power Electron.*, vol. 32, no. 9, pp. 6994–7010, 2017.
- [139] E. R. Sanseverino, G. Zizzo, V. Boscaino, J. M. Guerrero, and L. Meng, “Active load sharing technique for on-line efficiency optimization in DC microgrids,” *Conf. Proc. - 2017 17th IEEE Int. Conf. Environ. Electr. Eng. 2017 1st IEEE Ind. Commer. Power Syst. Eur. IEEEIC / I CPS Eur. 2017*, pp. 1–5, 2017.
- [140] P. García, P. Arboleya, B. Mohamed, A. A. C. Vega, and M. C. Vega, “Implementation of a hybrid distributed/centralized real-time monitoring system for a DC/AC microgrid with energy storage capabilities,” *IEEE Trans. Ind. Informatics*, vol. 12, no. 5, pp. 1900–1909, 2016.
- [141] A. Alfergani et al., “Control of master-slave microgrid based on CAN bus,” *2017 IEEE Jordan Conf. Appl. Electr. Eng. Comput. Technol. AEECT 2017*, vol. 2018-Janua, pp. 1–6, 2018.
- [142] J. J. Shieh, “Peak-current-mode based single-wire current-share multimodule paralleling DC power supplies,” *IEEE Trans. Circuits Syst. I Fundam. Theory Appl.*, vol. 50, no. 12, pp. 1564–1568, 2003.
- [143] A. Bidram and A. Davoudi, “Hierarchical structure of microgrids control system,” *IEEE Trans. Smart Grid*, vol. 3, no. 4, pp. 1963–1976, 2012.
- [144] A. P. N. Tahim, D. J. Pagano, E. Lenz, and V. Stramosk, “Modeling and stability analysis of islanded DC microgrids under droop control,” *IEEE Trans. Power Electron.*, vol. 30, no. 8, pp. 4597–4607, 2015.
- [145] L. Guo, S. Zhang, X. Li, Y. W. Li, C. Wang, and Y. Feng, “Stability analysis and damping enhancement based on frequency-dependent virtual impedance for DC microgrids,” *IEEE J. Emerg. Sel. Top. Power Electron.*, vol. 5, no. 1, pp. 338–350, 2017.
- [146] C. H. Yoo, W. J. Choi, I. Y. Chung, D. J. Won, S. S. Hong, and B. J. Jang, “Hardware-in-the-loop simulation of DC microgrid with multi-agent System for emergency demand response,” *IEEE Power Energy Soc. Gen. Meet.*, pp. 1–6, 2012.
- [147] A. T. Elsayed, A. A. Mohamed, and O. A. Mohammed, “DC microgrids and distribution systems: An overview,” *Electr. Power Syst. Res.*, vol. 119, pp. 407–417, 2015.
- [148] J. P. Torreglosa, P. García, L. M. Fernández, and F. Jurado, “Hierarchical energy management system for stand-alone hybrid system based on generation costs and

- cascade control,” *Energy Convers. Manag.*, vol. 77, pp. 514–526, 2014.
- [149] P. S. Kundur, *Power system dynamics and stability*. 2017.
- [150] A. Bin Jusoh, “The instability effect of constant power loads,” *Natl. Power Energy Conf. PECon 2004 - Proc.*, pp. 175–179, 2004.
- [151] S. Luo and I. Batarseh, “A review of distributed power systems part I: DC distributed power system,” *IEEE Aerosp. Electron. Syst. Mag.*, vol. 20, no. 8 II, pp. 5–15, 2005.
- [152] A. Emadi and M. Ehsani, “Multi-converter power electronic systems: Definition and applications,” *PESC, IEEE Annu. Power Elec. Spec. Conf.*, vol. 2, pp. 1230–1236, 2001.
- [153] W. Du, J. Zhang, Y. Zhang, and Z. Qian, “Stability criterion for cascaded system with constant power load,” *IEEE Trans. Power Electron.*, vol. 28, no. 4, pp. 1843–1851, 2013.
- [154] N. Eghtedarpour and E. Farjah, “Distributed charge/discharge control of energy storages in a renewable-energy-based DC micro-grid,” *IET Renew. Power Gener.*, vol. 8, no. 1, pp. 45–57, 2014.
- [155] R. W. Erickson, “Input Filter Design,” in *Fundamentals of Power Electronics*, vol. 1, pp. 378–408.
- [156] D. M. Mitchell, “Power Line Filter Design Considerations For dc-dc Converters,” *IEE Ind. Applicofionr Mogazine*, pp. 16–26, 1999.
- [157] R. W. Erickson, *Fundamentals of Power Electronics*, vol. 59. 2013.
- [158] A. Riccobono, S. Member, E. Santi, S. Member, and A. Power-electronics-based, “Comprehensive Review of Stability Criteria for DC Power Distribution Systems,” *IEEE Trans. Ind. Appl.*, vol. 50, no. 5, pp. 3525–3535, 2014.
- [159] F. and B. Liu, Q., Wang, “Frequency-domain EMI noise emission characterization of switching power modules in converter systems,” in *Twentieth Annual IEEE Applied Power Electronics Conference and Exposition*, 2005, pp. 787–792.
- [160] F. . Kelkar, S.S. and Lee, “Adaptive Input Filter Compensation for Switching Regulators,” *IEEE Trans. Aerosp. Electron. Syst.*, vol. 1, no. 1, pp. 57–66, 1984.
- [161] C. Louati, K., Sadarnac, D. and Karimi, “Input filter influence on the control stability of DC/DC converters,” in *IEEE International Symposium on Industrial Electronics*, 2004, no. 1, pp. 1165–1171.
- [162] M. Sclocchi, “Input filter design for switching power supplies,” pp. 1–9, 2011.



# APPENDIX A

## A.1. Matlab/Simulink

The DC microgrid simulation performed using MATLAB/SIMULINK. Matlab is a software package used to perform analysis and solve mathematical and engineering problems whereas, Simulink is a graphical extension to MATLAB for modeling and simulation of systems. In Simulink, orders drawn on the screen as block diagrams using blocks and lines. Blocks used to generate, modify, combine, output, and display signals. Wires used to transfer messages from one neighborhood to another. The DC microgrid components like sources, interfacing converter, BESS, and loads built using Simulink block and lines in MATLAB.

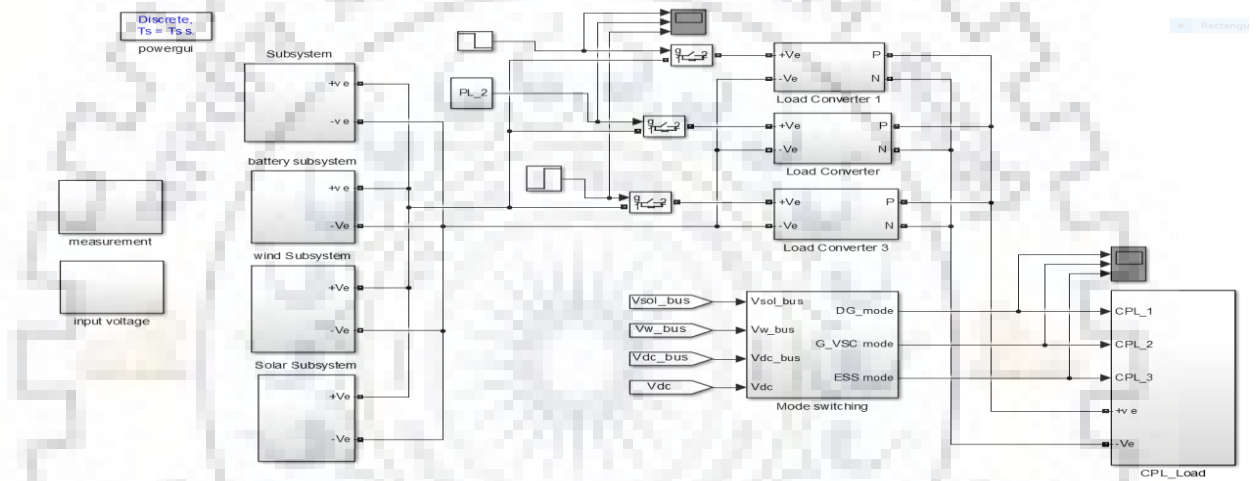


Fig. A. 1: Proposed DC Microgrid Matlab/Simulink

## A.2. Real-Time Simulation of DC Microgrid Matlab/Simulink Models Using OPAL-RT

Controller-in-the-loop simulation (CIL) is a technique used to develop and test control and protection systems. The aim is to check and certify the functionality, performance, quality, and safety of the control software.

In simulating DC microgrid Matlab/Simulink models with OPAL-RT, the following two main step processes are involved. The DC Microgrid models need to be designed accurately in Matlab/Simulink software, and the modeled DC microgrid categorized into the following three subsystems.

- 1) SM\_Master subsystem
- 2) SS\_Slave subsystem

### 3) SC\_Console subsystem

SM\_Master subsystem and SS\_Slave subsystem have the computational elements of the Microgrid model, whereas the SC\_Console subsystem has the user interface blocks like scopes and output displays etc. Users can analyze the real-time behavior of the system using the SC\_Console subsystem. Each subsystem runs in each different core of the simulator.

All inputs signals to the subsystem first must go through the Opcomm block that saves the communication information set-up. The designed DC microgrid model has run with 20 $\mu$ sec fixed step time to run the model in real-time by choosing a fixed step size according to model requirement and hardware capability.

Then RT-Lab software is used to convert the Simulink model into C-code and to load each subsystem into each core of the simulator. Finally, the microgrid model should be executed in RT-lab to analyze the real-time behavior of the system. While the model is running in real-time, the transients can be analyzed using the user interface window. All the outputs can be visualized in real-time to estimate the behavior of the system under different conditions.

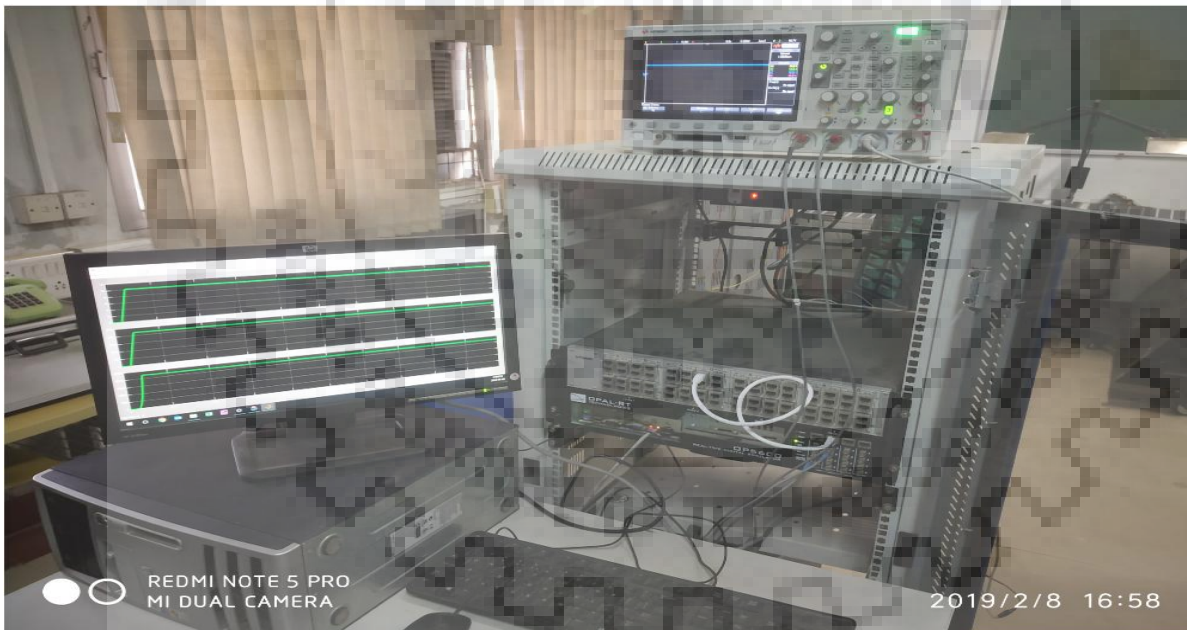


Fig. A. 2: Real-Time Simulation Set up Using OPAL-RT Simulator



## APPENDIX B

### B.1. List of Publication

#### i. Journal Article

1. **G. Ensermu**, Avik Bhattacharya, and Nigamananda Panigrahy, "Real-Time Simulation of Smart DC Microgrid with Decentralized Control System Under Source Disturbances." *Arabian Journal for Science and Engineering* (2019): 1-13.
2. **G. Ensermu**, Avik Bhattacharya, "Review of Recent Trend in DC Microgrid Topologies, Control and Stability," *Renewable and Sustainable Energy Reviews* (Under Review)

#### ii. International Conferences

1. **G. Ensermu** and A. Bhattacharya, "Control and Stability Analysis of DC Microgrids with Constant Power Loads and Source Disturbances," 2018 IEEE International Conference on Power Electronics, Drives and Energy Systems (PEDES), Chennai, India, 2018, pp. 1-6.
2. **G. Ensermu** and A. Bhattacharya, "Design of Decentralized Droop Control Structure of DC Microgrid with Constant Power Loads and Source Disturbances," 2018 IEEE Innovative Smart Grid Technologies - Asia (ISGT Asia), Singapore, 2018, pp. 91-96.
3. D . Debela, **G. Ensermu**, and A. Bhattacharya, "Design, control and simulation of grid-connected DC/AC microgrid for residential applications," 2017 Second International Conference on Electrical, Computer and Communication Technologies (ICECCT), Coimbatore, 2017, pp. 1-6.